The instability of shear layers produced by curved shocks

Thesis by

Patrick Lemieux

In Partial Fulfillment of the Requirements

for the Degree of

Doctor of Philosophy

California Institute of Technology

Pasadena, California

1999

(Submitted May 13, 1999)

A ma chère Su-ying,

ainsi qu'à mes parents, Johanne et André.

Acknowledgements

Pursuing doctoral studies at Caltech and especially in a facility such as the T5 Hypervelocity Shock Tunnel is not a task that can be accomplished successfully without the influence of many outside factors, including the help of many exceptional people.

I am grateful to Professor Hans Hornung who provided me with advice and inspiration during my years at Caltech. Many thanks to Professor Joseph Shepherd who on more than one occasion also provided deep insight into this project.

I am truly indebted to Michael Kaneshige for his expertise and help with the Light Gas Gun facility. I also wish to thank Jean-Paul Davis, Simon Sanderson and Eric Cummings for technical help in the lab. Bahram Valiferdowsi has provided important support in running and maintaining the facility. Joe Haggerty and Ali Kiani were patient and skilled in manufacturing the test model. Professors Bob Rogers and Jim Venart of the University of New Brunswick in Fredericton, Canada, provided me with the academic tools to succeed at Caltech. Professor Ed Zukoski provided needed assistance during my first two years of graduate studies. John Blandino and Donald Kendrick's help with my candidacy preparation is hereby gratefully acknowledged. Many thanks to Marionne Epallé and Karen Cheetham for proofreading the thesis.

I feel privileged to have had the friendship of the following people while at Caltech: Victor Burnley, Jim Smith, Philippe Adam, Branislav Kecman, Kenneth Clarke, Boris Dewitte, Uli Pfahl, Julian Lee, Muriel & Flavio Noca, Paul Sivilotti, Susan Paulsen, Sergio Turteltaub and Matthias Noelker. True learning, even in science, does not only come from books, lectures and experiments. I have learned greatly from you.

Most of all, I would like to thank my parents, Johanne and André Lemieux, and my wife, Su-ying, for their constant love and support. This work would not have been possible without them.

Financial support for this project was provided in part by the Natural Sciences and Engineering Research Council of Canada.

Abstract

A curved shock of general shape in hypersonic flow generates vorticity, so that a shear layer is formed in the flow downstream of the shock. The parameters affecting the distribution of vorticity in the shear layer are identified. Experiments aimed at determining the preferred wavelength of structures that develop in these flows are carried out in the T5 Hypervelocity Shock Tunnel. To visualize these structures, a new technique using streaklines is developed. The results are compared with numerical simulations of perfect-gas flows.

The numerical study also points to a flow regime, as the Newtonian limit is approached, where the instability of the shear layer is such that the shock becomes distorted. A series of experiments aimed at investigating flows approaching this limit is performed, using the T5 Light Gas Gun facility, and confirms the existence of this new regime.

Contents

List of Figures

Chapter 1 Introduction

1.1 Background

One of the problems associated with a vehicle reentering the atmosphere at orbital speeds is the extremely high heat transfer rate in the vicinity of the stagnation region. To be able to dissipate some of that heat, it is necessary for the vehicle to be blunted at the nose, though this increases the drag. The nose bluntness causes the bow shock on the vehicle to be detached and curved. As has been shown by Lighthill [1957], a curved shock of general shape in uniform, steady flow generates vorticity so that a shear layer is formed in the region between the body surface and the shock wave.

An alternative way to view this situation is to look at the entropy field. A region of high entropy increase is formed behind the 'strong' part of the shock wave (*i.e.*, $M_\infty \sin(\beta) \gg 1$, where β is the local wave angle). This 'entropy wake' has a lateral dimension which may be large, but limited. Since for inviscid, non-reacting flow the entropy is constant along streamlines downstream of the shock, a strong gradient of entropy exists across the entropy wake, with high entropy near the body and low entropy near the shock wave. This zone of comparatively high entropy is why the region near the body is often referred to as the 'entropy layer'[1].

The importance of this entropy layer, flowing over the body of a reentry vehicle, on the flow field surrounding the vehicle, both in terms of heat transfer and drag, has been appreciated by several research groups over the last thirty years. A group at NASA Ames was responsible for a large body of work on the effect of cone nose bluntness at high Mach numbers (*e.g.*, Cleary [1965], Cleary [1966], and Cleary [1968]). Their work concentrated on taking static and pitot pressure measurements on cones of

[1] Although some authors take special care in making the distinction between 'entropy wake' and 'entropy layer', the distinction is unimportant for the discussion that follows, and the terms are used interchangeably.

varying geometries at different flow conditions commensurate with Earth reentry. Softley [1968] also performed experiments over blunt cones; he observed a correlation between the nose bluntness and the boundary layer transition. More recently, work done by Stetson *et al.* [1984] and Ericsson [1988] on blunt cones provided empirical rules correlating the distance at which the entropy layer is 'swallowed'[2] as a function of nose bluntness, and the boundary layer transition. Figure 1.1 illustrates the various parameters used in this analysis. The distance at which the entropy layer is swallowed is X_{sw}; the distance to transition is X_{tr}; and the length of the cone is L. Although this recent work alludes to the possibility that an instability in the entropy layer itself is responsible for the correlation between the distance to entropy layer swallowing and boundary layer transition, the origin of such an instability was not identified, and the experiments lacked the required flow visualization techniques to observe it, should it occur.

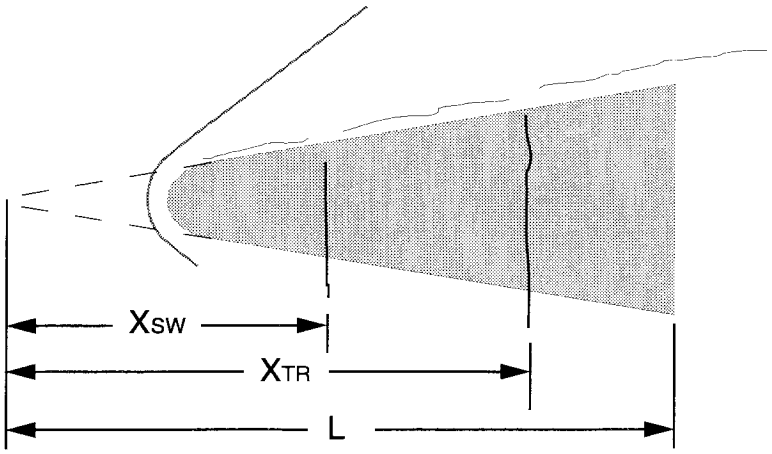

Figure 1.1. Entropy layer swallowing and boundary layer transition.

Few groups appear to have focused their studies on the physics of the flow within the entropy layer itself, as it flows downstream of the shock, and as an entity decoupled from the boundary layer.

A few notable examples of the occurrence of an instability developing in the shear

[2]'Entropy layer swallowing' is the expression used to describe the phenomenon by which the entropy layer, which becomes thinner as it flows over an axisymmetric body, becomes fully entrained within the growing boundary layer.

layer produced by a curved shock do exist in the literature, but the source of the instability in the flow, or even the mention that an instability exists, has been either omitted or misinterpreted. One example is the published schlieren photograph of Mach *et al.* [1962], which shows a spherical projectile traveling at 3000 m/s in carbon tetrachloride for the purpose of an experiment aimed at measuring the temperature within the stagnation region of the shock layer. The instability of the entropy layer which develops under these conditions and is clearly evident in the photograph is not mentioned. Series of experiments were also performed in a hypersonic ballistic facility in Leningrad (Mishin and Mende [1967]) from the late 1970s through the 1980s. The purpose of these experiments was to use a novel technique (projectiles) to study a type of shock instability associated with dissociating gases and first observed by Griffiths *et al.* [1975] in shock tube experiments. This instability, found to occur at shock front velocity nearing that where the value of $(\partial P/\partial v)_h$ is positive on the Rankine-Hugoniot curve[3] (due either to ionization or dissociation of the gas), appears to have been reproduced with some success in ballistic experiments in Leningrad (Baryshnikov *et al.* [1979]). The phenomenon, referred to as "Relaxational Instability of Shock Wave" (RISW), was identified by Baryshnikov and his colleagues as the source of the instability found in the inviscid wake of projectiles traveling within a certain speed window and certain initial conditions (including pressure and gas composition). Since RISW only occurs within a small region of the shock layer, it is unlikely that it is responsible for instabilities present far downstream, such as claimed by Bedin [1989]. Instabilities which affect the shock layer far downstream of the stagnation point are more likely to be due to an instability in the entropy layer.

An important observation discussed in Stetson [1979] during experiments done on blunt cones in hypersonic flow, is that increasing cone bluntness delays boundary layer transition until the laminar flow section reaches a maximum length. It was found that further increases in nose bluntness beyond that point then reduce the laminar flow region of the boundary layer. One of the possible reasons for this reversal to occur is an instability in the entropy layer itself, where oscillations developing within the

[3] P, v, and h are the pressure, specific volume, and specific enthalpy behind the shock.

entropy layer penetrate the boundary layer and initiate early transition to turbulence. An analytical study of this phenomenon was undertaken by Fedorov [1990]. Linear theory was used to analyze self-oscillations in the entropy layer on a blunt flat plate. Fedorov set up the eigenvalue problem for the region of the entropy layer around the expected point of inflection in the velocity profile. The analysis revealed the existence of one unstable mode. Furthermore, it was also found that the greatest instability, that which grows downstream at the fastest rate, occurs at a finite Mach number. Some of these conclusions, however, may pertain specifically to the flow over flat plates, which does not remain rotational very far downstream of the shock. It is unclear how these results translate to different geometries, especially those for which the flow remains rotational over large distances over the body.

A common difficulty in all the experiments done on the stability of entropy layers is visualizing adequately that region of the flow field. It is difficult using conventional flow visualization techniques to detect the changes in the flow field associated with this instability. Instead, diagnostic tools such as hot-wire anemometry have been used to try to detect the fluctuations associated with this instability.

Recall that according to the Rayleigh stability criterion, an inflection point in the velocity profile is a necessary condition for an instability to develop in inviscid flow (Rayleigh [1880]). Stetson *et al.* [1984], in a notable effort using hot wires, attempted to detect this inflection point, but were unsuccessful.

It is clear that the conditions under which the shear layer becomes unstable are not well understood, and that the role played by the source of the shear layer, namely the vorticity produced at the curved shock, may not have been sufficiently well appreciated. Although a sufficient condition for instabilities to develop in such a shear layer has yet to be established, the more rotational the flow, the more likely instabilities are to develop. Thus, it is important to understand how vorticity is generated at the shock, and how to maximize it. Similarly, it is important to understand how high levels of vorticity may be maintained far downstream of the shock. The answer to these questions will help define a strategy which will be used to study the instability of the shear layer produced at curved shocks.

1.2 Vorticity generation by curved shocks

Although the vorticity generated by a curved shock is a subject treated in a number of textbooks and journal articles (*e.g.*, Truesdell [1952], Lighthill [1957], or Hayes and Probstein [1966]), the derivation sheds light on the distribution of vorticity in the shear layer. To make the concept clear, and for the sake of completeness, the derivation is included here.

The starting point for such a derivation is the Crocco-Vazsonyi momentum equation (Vazsonyi [1945]), written here for an inviscid fluid with no body force:

$$\frac{\partial \tilde{u}}{\partial t} + \tilde{\omega} \times \tilde{u} = T\nabla s - \nabla(h + |\tilde{u}|^2) \,, \tag{1.1}$$

where $\tilde{u}$ is the velocity vector; $\tilde{\omega}$ is the vorticity vector; T is the temperature; s is the specific entropy; and h is the specific enthalpy.

For the case of steady, frictionless, homenthalpic flows, this reduces to the Crocco equation:

$$\tilde{\omega} \times \tilde{u} = T\nabla s \,. \tag{1.2}$$

In order to draw useful results from this equation, however, the gradient of entropy must be expressed in terms of the flow properties along the downstream part of the shock. To do this, first consider the shock conditions for conservation of mass, momentum, and energy:

$$\rho_1 u_1 = \rho_2 u_2 \,, \tag{1.3}$$

$$P_1 + \rho_1 u_1^2 = P_2 + \rho_2 u_2^2 \,, \tag{1.4}$$

and

$$h_1 + u_1^2/2 = h_2 + u_2^2/2 \,, \tag{1.5}$$

where the subscripts 1 and 2 denote the location before and after the shock, respectively, and the shock geometry is illustrated in Figure 1.2(a). The momentum

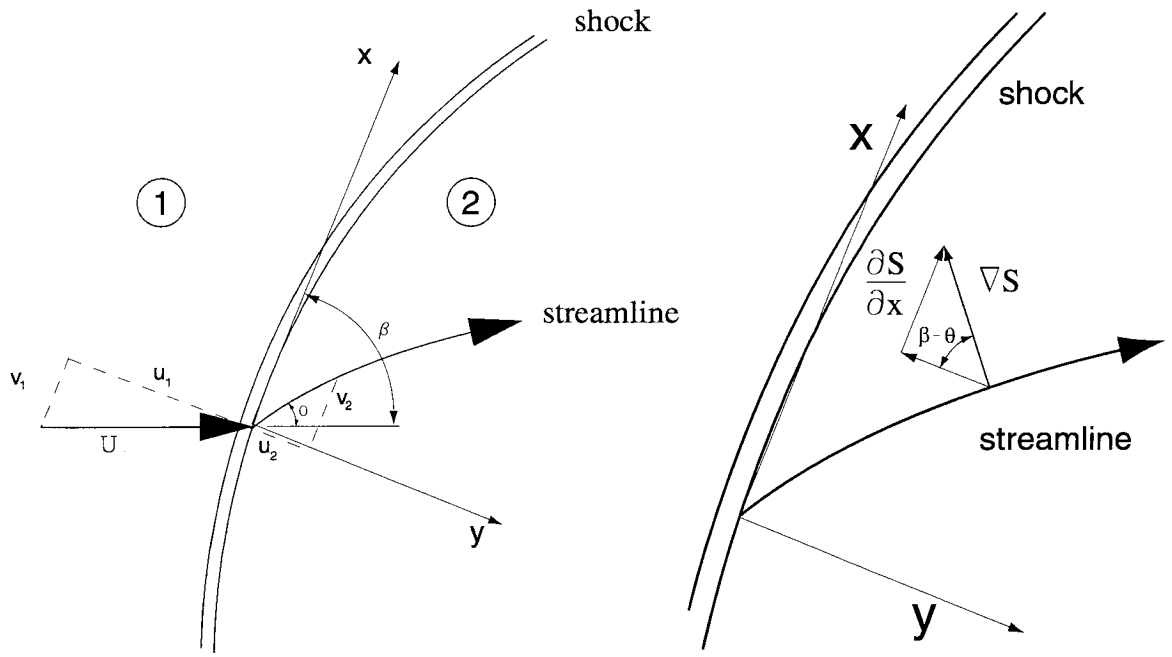

(a) Curved shock coordinates (b) Entropy gradient

Figure 1.2. Coordinate system used for a curved shock.

equation (1.4) may be rearranged to give:

$$P_2 = P_1 + \rho_1 U_\infty^2 \sin^2(\beta)\left(1 - \frac{\rho_1}{\rho_2}\right) , \tag{1.6}$$

and the energy equation (1.5) may be rearranged to give:

$$h_2 = h_1 + \frac{1}{2} U_\infty^2 \sin^2(\beta)\left(1 - \frac{\rho_1^2}{\rho_2^2}\right) . \tag{1.7}$$

These equations provide a convenient form to be used in the Gibbs relation, which relates the entropy to the pressure and enthalpy:

$$T\frac{\partial s}{\partial \beta} = \frac{\partial h}{\partial \beta} - \frac{1}{\rho}\frac{\partial P}{\partial \beta} . \tag{1.8}$$

Differentiating and substituting equations (1.6) and (1.7) into equation (1.8), the result for the entropy change is

$$T_2 \frac{\partial s_2}{\partial \beta} = U_\infty^2 \sin(\beta)\cos(\beta)\left(1 - \frac{\rho_1}{\rho_2}\right)^2 . \tag{1.9}$$

It is more convenient, however, to express the derivative of entropy with respect to the distance along the shock instead of with respect to the shock angle. The two are related by

$$\frac{\partial s}{\partial \beta} = \frac{\partial s}{\partial x}\frac{\partial x}{\partial \beta} + \frac{\partial s}{\partial y}\frac{\partial y}{\partial \beta} = \frac{\partial s}{\partial x}\frac{\partial x}{\partial \beta} = r\frac{\partial s}{\partial x} , \tag{1.10}$$

where r is the local radius of curvature of the shock.

Equations (1.6) to (1.9) are now in a form that may easily be used in Crocco's equation. From the geometry of the shock (see Figure 1.2 (b)), the right-hand side of equation (1.2) may be expressed as

$$T_2 \left|\nabla s_2\right| = \frac{T_2\, \partial s_2/\partial x}{\sin(\beta - \theta)} . \tag{1.11}$$

Similarly, the left-hand side of equation (1.2) reduces to

$$\left|\tilde{\omega} \times \tilde{u}\right| = -\omega\, U_\infty \frac{\cos(\beta)}{\cos(\beta - \theta)} , \tag{1.12}$$

so that Crocco's equation gives

$$-\omega\, U_\infty \frac{\cos(\beta)}{\cos(\beta - \theta)} = \frac{T_2\, \partial s_2/\partial x}{\sin(\beta - \theta)} . \tag{1.13}$$

Rearranging the terms, and noting that for an oblique shock,

$$\tan(\beta - \theta) = \frac{\rho_1}{\rho_2}\tan(\beta) , \tag{1.14}$$

Hayes and Probstein [1966] have in this manner shown that the vorticity downstream of a two-dimensional, planar curved shock is given by

$$\omega = -U_\infty\, \kappa\, \cos(\beta)\left(\frac{\rho_2}{\rho_1} + \frac{\rho_1}{\rho_2} - 2\right) , \tag{1.15}$$

where ω is the vorticity normal to the plane of the flow; κ is the local shock curvature

($\kappa = 1/r$); the wave angle is β; and the density ratio across the shock is ρ_2/ρ_1. Finally, from dimensional analysis, the vorticity given by this equation is often non-dimensionalized with the free-stream speed and a characteristic length, *e.g.*, the radius of curvature d of the shock at the normal-shock point, to give

$$\frac{\omega\, d}{U_\infty} = -d\,\kappa\,\cos(\beta)\left(\frac{\rho_2}{\rho_1} + \frac{\rho_1}{\rho_2} - 2\right) . \tag{1.16}$$

1.2.1 Parameters affecting vorticity generation

Consideration of equation (1.16) shows that two factors play a role in determining the non-dimensional vorticity at the shock:

1. The density ratio across the shock, ρ_2/ρ_1.

2. The shock shape, which fixes $\kappa\,\cos(\beta)$.

From this equation, moreover, the relative importance of each of these factors on the overall vorticity distribution may now be determined. In particular, it is important to find out what role each plays on the peak vorticity.

To illustrate the features of the vorticity distribution and to discuss the relative importance of these two factors, consider the example of flow of a perfect gas over a two-dimensional blunt body. Significant differences relating to the flow of real gases will be pointed out in later sections.

First, the effect of the density ratio on the vorticity distribution is investigated. Recall that for oblique shocks of angle β in a perfect gas, the jump in density across the shock is given by

$$\frac{\rho_2}{\rho_1} = \frac{\gamma + 1}{\gamma - 1 + 2/(M_\infty^2 \sin^2\beta)} , \tag{1.17}$$

i.e., the Mach number and the ratio of specific heats determine the density ratio. β is fixed by the shock shape. Since we wish to exclude the effect of shock shape, a model independent of M_∞ and γ is used. A good model under these circumstances is that of a parabola

$$\frac{y_s}{d} = \left(\frac{x_s}{d}\right)^{1/2} .$$

The parameter d is selected so that the parabola's nose curvature matches that of the shock; the remaining parts of the parabola, far from the origin, best approximate very strong shocks in axisymmetric flow.

The effect of the density ratio on peak vorticity can now be investigated. Since two parameters affect the density ratio, we proceed by first keeping the ratio of specific heats constant and varying the Mach number, and then by keeping the Mach number constant and varying the ratio of specific heats. Vorticity distributions for both of these cases are plotted in Figures 1.3 and 1.4.

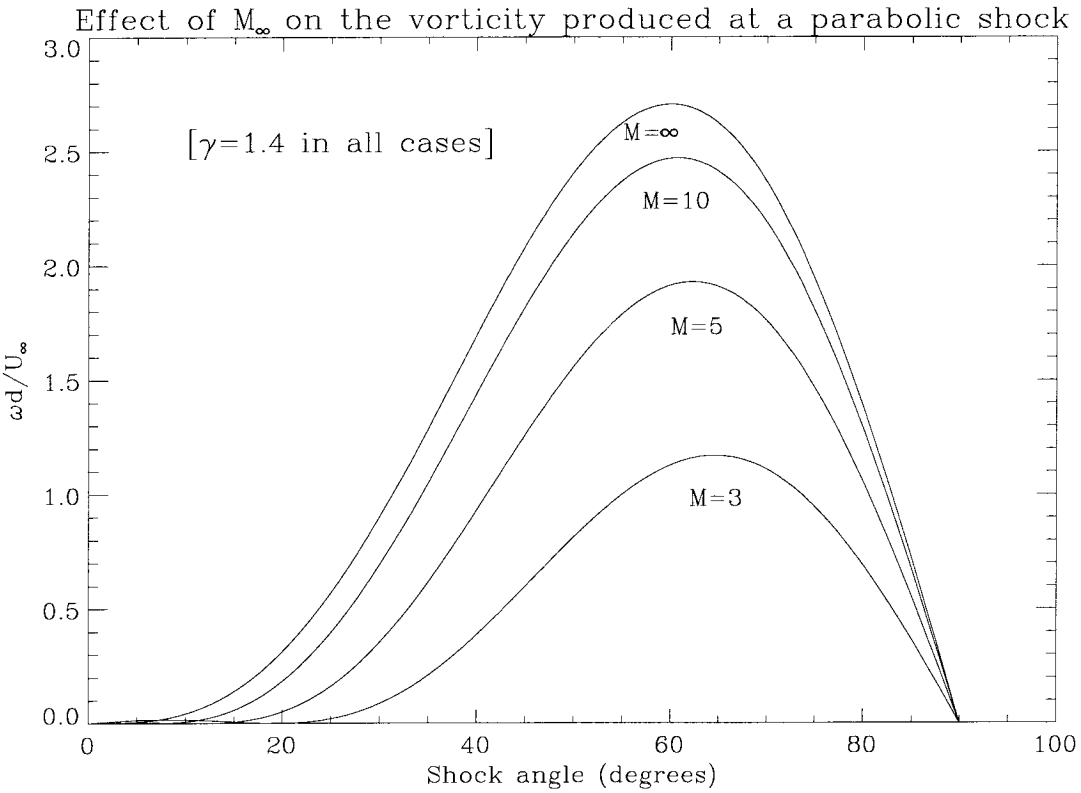

Figure 1.3. Vorticity distributions: density ratio effect with changing Mach number.

Figure 1.3 illustrates well how the peak vorticity increases significantly with increasing Mach number, up to around 5, but that beyond this point, changes in peak vorticity are relatively insensitive to Mach number. The density ratio approaches $(\gamma+1)/(\gamma-1)$ at high Mach numbers, which is not very large unless gamma is close to one. The limiting trend is different when the Mach number is fixed and γ ap-

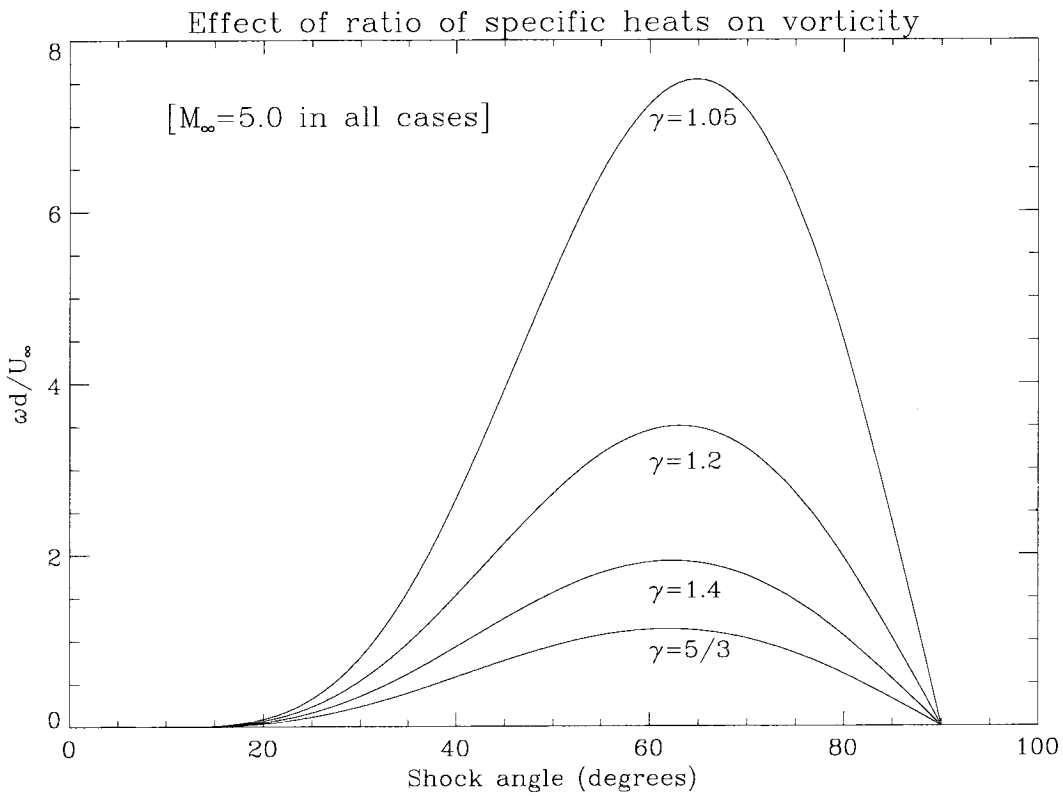

Figure 1.4. Vorticity distributions: density ratio effect with gamma approaching 1.

proaches unity, as shown in Figure 1.4. Even small changes in gamma towards unity cause large increases in peak vorticity. The density ratio approaches M_∞^2 for very small values of $\gamma - 1$.

Next, the effect of the shock shape on the distribution is assessed. To do this, an additional model for the shock shape is introduced. The hyperbola is a convenient model for the shock shape, since it has a finite radius at the nose and asymptotically approaches a straight line far downstream. The parameters of the hyperbola may be chosen so that the slope of the straight line is that of a Mach wave, thus giving a close approximation to curved shocks over a wide range of Mach numbers. Its equation is given by

$$\frac{y_s}{d} = \frac{1}{\sqrt{M_\infty^2 - 1}} \left(\frac{x_s^2}{d^2} + (M_\infty^2 - 1)\frac{x_s}{d} \right)^{1/2} .$$

Both the hyperbola and parabola models are sketched in Figure 1.5, using several Mach numbers to generate different hyperbolic profiles. While both models are often

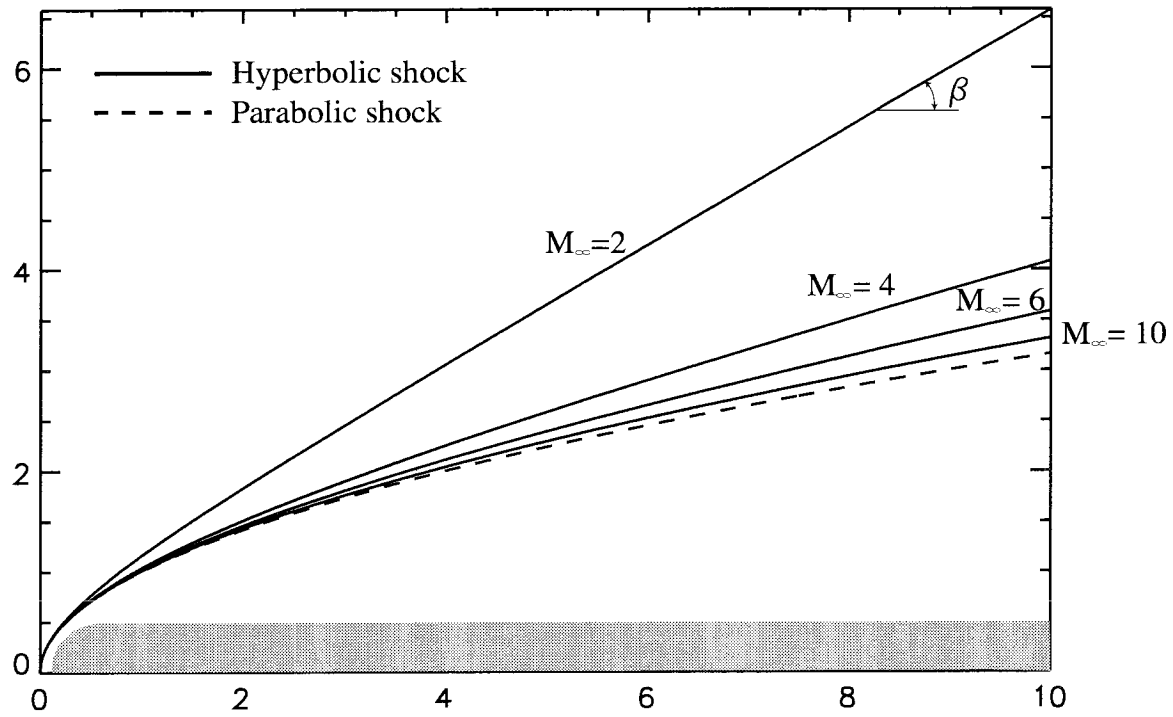

Figure 1.5. Shock shapes for hyperbolic and parabolic shock models.

used to represent shock waves over blunt bodies, there are important differences between the two. Since the parabola is the $M_\infty \to \infty$ limit of the hyperbola, both models converge in the hypersonic limit. For finite Mach numbers, however, the shock shapes of the two models differ, diverging greatly as x increases, as shown in Figure 1.5. Both of these models may be used to investigate the effect of $\kappa \cos(\beta)$ on vorticity generation.

The distribution of vorticity with respect to shock angle for these two models is shown in Figure 1.6, for the case of a perfect diatomic gas ($\gamma = 1.4$) at various free-stream Mach numbers. Four cases are shown, comparing the distributions obtained at Mach number 2, 5, 10, and ∞. The difference in peak vorticity at the different Mach numbers is mainly due to the dependence of the density ratio on that parameter.

The two shock models give the same distribution of vorticity at infinite Mach number, as expected, and their distributions are very similar at high Mach numbers.

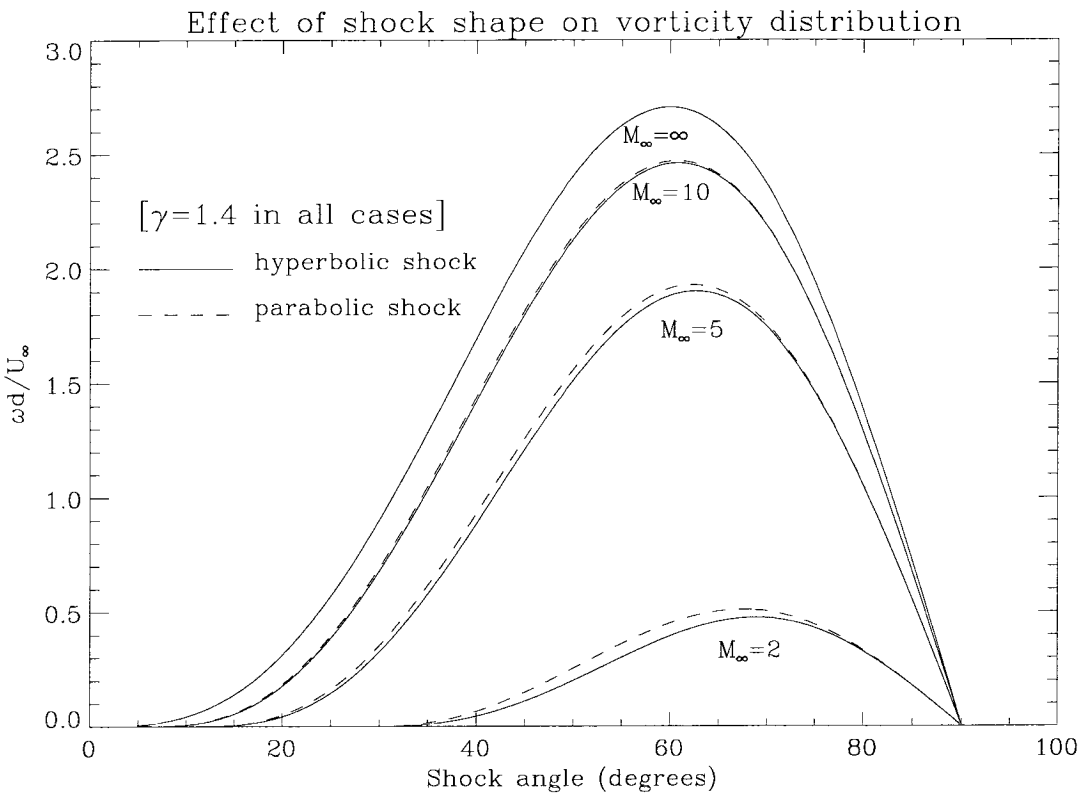

Figure 1.6. Vorticity distributions: effect of shock shape.

An important observation, however, is that the distributions never differ significantly, even at Mach numbers as low as 2, where Figure 1.5 clearly shows that the two shock shapes are very different. It may therefore be concluded that the relative role of $\kappa \cos(\beta)$ on peak vorticity and on the shape of the distribution of vorticity in general is not significant when compared to the effect of changes in density ratio across the shock.

This analysis suggests that an optimum strategy for a study of the stability of the entropy layer should focus as much as possible on hypersonic flow using a gas with a high density ratio. It also shows that for flows beyond $M_\infty \approx 5$, this is better accomplished by selecting gases with low γ than by increasing the Mach number.

1.2.2 Transport of vorticity in the flow

The above description of the vorticity produced addresses only the region of the flow immediately downstream of the shock. Now consider the way in which the vorticity produced at the shock changes as it is subsequently convected downstream of the shock. For the case of steady, inviscid flow, the Crocco-Vazsonyi equation (equation (1.1)) becomes

$$\tilde{\omega} \times \tilde{u} = T\nabla s - \nabla(h + |\tilde{u}|^2). \tag{1.18}$$

Taking the curl of the momentum equation gives

$$\rho \frac{D(\tilde{\omega}/\rho)}{Dt} = (\tilde{\omega} \cdot \nabla)\tilde{u} + \nabla T \times \nabla s \tag{1.19}$$

which for planar two-dimensional flow reduces to

$$\rho \frac{D(\tilde{\omega}/\rho)}{Dt} = \nabla T \times \nabla s. \tag{1.20}$$

These two equations, (1.18) and (1.20), provide the starting point for analyzing the variation of vorticity along streamlines downstream of the shock. Two specific cases are considered here.

For the special case of homentropic, steady, planar flow, equation (1.20) reduces to

$$\frac{\partial}{\partial \xi}\left(\frac{\omega}{\rho}\right) = 0, \tag{1.21}$$

where ξ is the streamline coordinate. That is, in the special case where the entropy remains constant throughout the flow, the vorticity is expected to vary in the same manner as the density, along streamlines. As has been shown earlier, hypersonic blunt body flows are not homentropic, however, but are normally homenthalpic, so that equation (1.2) applies. From equations (1.2) and (1.19), we find that

$$\frac{\partial}{\partial \xi}\left(\frac{\omega}{\rho T}\right) = 0\,. \tag{1.22}$$

Thus, for inviscid, homenthalpic, planar flow over a blunt body, the vorticity produced at a curved shock remains constant downstream of the shock, provided that the product of the density and the temperature also remains constant. For the case of a perfect gas, this is equivalent to having the pressure remain constant[4]. This fundamental observation is crucial in the design of an experiment for the study of the stability of the shear layer produced by a curved shock.

Differences between such an experiment and the above analysis based on a perfect gas must now be stressed. Although the general mechanism of vorticity production is the same in the case of a real gas, some important distinctions exist. A molecular gas in hypervelocity flow experiences rapid heating as it passes through a shock. This rapid heating excites new vibrational energy levels in the gas, and may cause significant dissociation to occur. Both of these phenomena play an important role on the overall density jump across the shock, which has been shown in the previous section to be the principal factor affecting vorticity production. In fact, the overall effect of hypervelocity real gas flow on the density jump is to cause a significant *increase* in the density ratio, compared to the flow of a perfect gas, as shown by Hayes and Probstein [1966]. Hence, facilities capable of producing hypervelocity flows are ideally suited for an experimental investigation of the stability of shear layers.

1.3 Experimental facilities for hypervelocity flow simulations

Many of the problems relating to flight to and from space are associated with the high speeds of such flights through the atmosphere, and the subsequent high stagnation temperatures. Simulating the effects that result from high temperatures in ground facilities requires the test time to be short, since materials currently available cannot sustain these temperatures for very long. The shock tunnel with heated driver gas has therefore been the most usual type of flow facility in this regime. In the free-

[4]Note that even in the case of a reacting gas, ρT is approximately proportional to the pressure.

piston shock tunnel (pioneered by Stalker [1961]), the driver gas is heated by adiabatic piston compression. The transient heating achieved by this method permits operation at higher driver temperatures.

The T5 hypervelocity shock tunnel is such a facility. A sketch of the shock tunnel, including the specification of some of its main components, is included in Figure 1.7. Detailed descriptions of the specific facility may be found in Bélanger [1993], Germain [1994], and Wen [1994]. Descriptions of the operation of piston-driven shock tunnels in general are also available in the literature (Lukasiewicz [1973]).

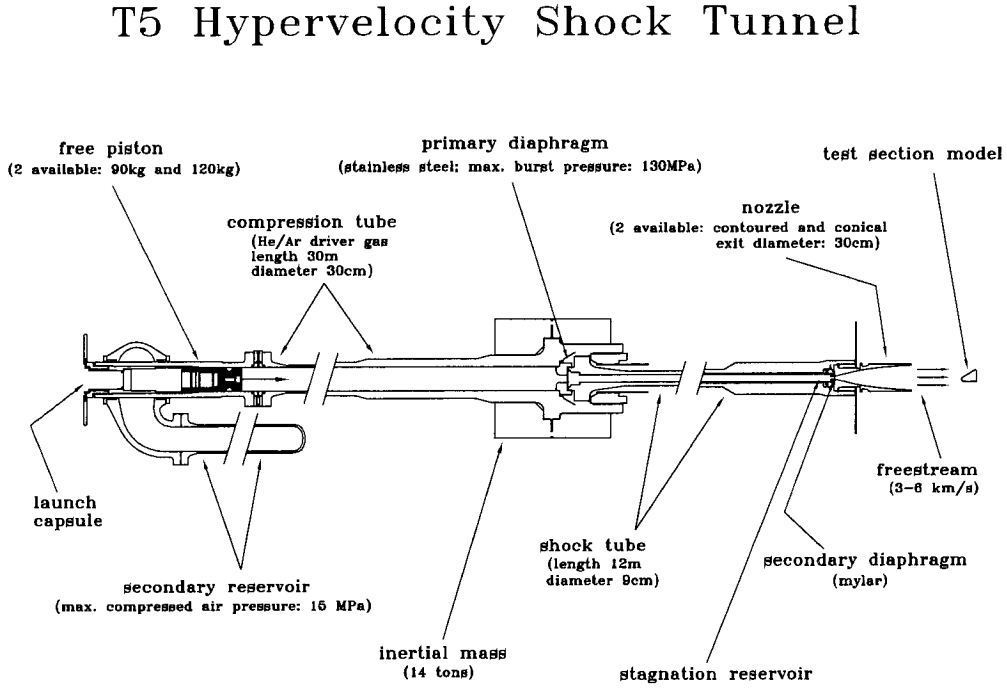

Figure 1.7. Sketch of the T5 Hypervelocity Facility.

1.3.1 Range of conditions available in T5

In the shock tunnel, the test gas is heated and compressed by the passage of a shock. The shock is then reflected from the end wall of the shock tube, bringing the test gas to rest by compressing it and heating once more. The test gas is then expanded from

this reservoir state through the nozzle. For a given test gas and nozzle shape, the conditions at the nozzle exit depend only on the reservoir state, provided that the test gas is in equilibrium in the reservoir. The reservoir state may be characterized by its pressure, P_0, and specific enthalpy, h_0.

The free-piston shock tunnel permits the reservoir state to be varied over very large ranges by varying the driver parameters such as driver gas composition, driver gas compression ratio, diaphragm burst pressure, secondary reservoir pressure, and piston mass. An essential requirement constraining the range of these parameters is a safe piston trajectory, so that damaging impact between the piston and the end of the compression tube is avoided.

Ground testing facilities are in general designed for the realistic simulation of flow conditions encountered during atmospheric flight. In the case of hypervelocity facilities such as T5, the flow being reproduced is that encountered by a reentry vehicle (or any object traveling at high speed through the atmosphere, such as a meteor or a satellite). To understand how this flow regime differs from others (particularly from the flow of a perfect gas), it is useful to consider specific examples. Consider the case of a vehicle reentering the Earth's atmosphere. A typical speed for such a vehicle during reentry is $U_\infty \approx 6\,\mathrm{km/s}$. The specific kinetic energy of the gas relative to the vehicle is $U_\infty^2/2 = 18$ MJ/kg. As the gas comes to rest on the surface of the vehicle in the stagnation region, this kinetic energy is converted to thermal energy. Now, if it is assumed that the gas is diatomic and behaves according to the perfect gas law, then its specific heat is given by

$$C_p = \frac{7}{2}\frac{R}{M} \approx 1000\,\frac{\mathrm{J}}{\mathrm{kg}\cdot\mathrm{K}}\,, \tag{1.23}$$

so that its temperature increase at the surface of the body is

$$\Delta T = \frac{h}{C_p} \approx 18000\ \mathrm{K}\,. \tag{1.24}$$

Flight test data, however, have shown that vehicles traveling in the atmosphere at even

higher flow regimes (*e.g.*, Apollo reentry) do not experience temperatures higher than approximately 11000 K (Anderson [1989]), so that the perfect gas model is clearly inappropriate in this case. In reality, when the thermal energy is sufficiently large, a significant fraction of the gas molecules become vibrationally excited or dissociate or even possibly ionize, so that the gas behaves very differently from a perfect gas. If the rate at which this occurs is very rapid, then the gas may be considered to be in thermodynamic and chemical equilibrium everywhere. If the rate is slower, however, then thermodynamic and chemical nonequilibrium effects need to be taken into account. Hence, these 'real gas effects' occur as a result of a combination of two phenomena.

1. The specific enthalpy is of the same order as the dissociation energy D of the gas molecules.

2. The rate of dissociation is finite and introduces a time scale t_D that must be taken into account when characterizing the gas.

This time scale also introduces a length scale $l_D = U_\infty t_D$. Hence, in order for a ground facility to properly model the flow around a reentry vehicle, it is necessary that the dimensionless groups $U_\infty^2/(2D)$ and l_D/L, where L is a characteristic length of the vehicle, be kept the same for both the test model and the reentry vehicle. The gas used in the simulation is chosen as the one being simulated since many properties of this gas must be duplicated. Now, since D is a property of the gas, U_∞ must also be duplicated in the facility. Also, the need to duplicate the flight value of l_D/L means that as the characteristic length is scaled down from the original vehicle to the model, l_D must also be scaled down by the same amount. Since dissociation occurs as a result of collisions between gas molecules, it is intimately related to the density of the gas. In fact, l_D is inversely proportional to the density ρ for the dissociation reaction. It therefore follows that in order for the ratio l_D/L to be duplicated in the experiment, the product ρL must also be duplicated. The range over which this parameter, referred to as the 'binary scaling parameter', may be varied is thus an important index of the ability of a facility to model the real gas flows of reentry.

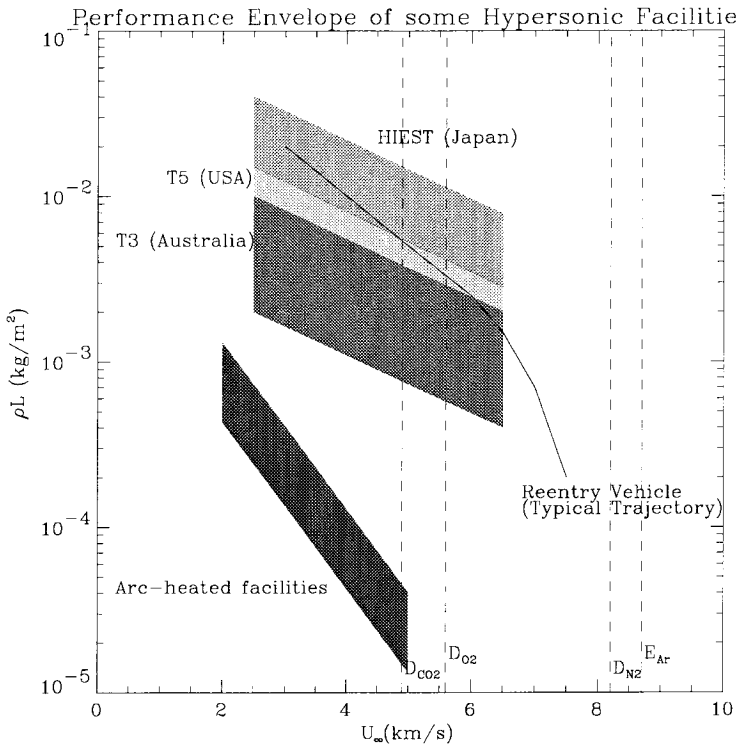

Figure 1.8. Comparison of various hypervelocity ground testing facilities.

Two parameters must therefore be reproduced in the facility: the flow speed of the vehicle, which limits the enthalpy of the flow; and the binary scaling parameter ρL, which is proportional to the non-dimensional chemical reaction length of the gas, both in the flow around the vehicle and in the ground testing facility. The available range of these parameters forms an envelope of test conditions which characterizes the ground testing facility. Figure 1.8 illustrates how the T5 envelope compares with those of selected other existing facilities, and to a typical reentry vehicle. In this figure, it is assumed that the span of the model is half of the nozzle diameter d, so that the characteristic length L is $d/2$. The envelope for T5 is based on actual shot conditions; the envelopes for the arc-heated facility and T3 are adapted from Hornung [1988]; the envelope for HIEST is adapted from Itoh *et al.* [1997]. The lower bound on each of the envelopes shown is for illustrative purposes only; the facilities are only strictly limited at the low end of ρL by their vacuum capability.

Table 1.1 lists several dissociation reactions relevant to Earth and Mars reen-

try. The enthalpy of formation for each of these reactions is listed, along with the corresponding reentry flight speed based on an energy balance along the stagnation streamline

$$D = h_\infty + U_\infty^2/2 \approx U_\infty^2/2 \,, \tag{1.25}$$

i.e.,

$$U_\infty \approx \sqrt{2\,D}\,, \tag{1.26}$$

so that the dissociation energy of the various gases may also be plotted (as dashed vertical lines) in Figure 1.8.

Table 1.1. Selected reactions relevant to reentry flows.

Reaction	Enthalpy of formation	Free-stream speed
$CO_2 \rightarrow CO + O$	12.1 MJ/Kg	4900 m/s
$O_2 \rightarrow O + O$	15.6 MJ/Kg	5600 m/s
$N_2 \rightarrow N + N$	33.7 MJ/Kg	8200 m/s
$Ar \rightarrow Ar^+ + e^-$	38.0 MJ/Kg	8700 m/s

For the purposes of studying the vorticity generated at a shock, the parameters of interest in the test section are the free-stream Mach number, total enthalpy, and gas properties. These have a direct effect on the levels of vorticity produced at the shock, as they affect the density jump across the shock.

1.4 Scope

The scope of the current project is to explore experimentally the stability of the shear layer generated by a blunt body in hypersonic flow. It is the goal of the present thesis to address the following questions:

1. What are the flow conditions under which the shear layer becomes unstable?

2. How far downstream from the shock is their effect visible?

3. What diagnostic tools are currently available to detect these instabilities?

4. What diagnostic tools would be best suited to investigate these flows?

5. Assuming that these instabilities exist (outside of the boundary layer), what physical parameters affect their wavelength?

6. Assuming that these instabilities exist, what is their overall effect on the flow and on the shock profile?

Chapter 2 Numerical Investigation of Shock Generators

2.1 Goal of the numerical investigation

Although a description of the physical mechanisms responsible for the generation and transport of vorticity at a shock has been presented in the previous chapter, a shock generator optimized to study the shear layer instability that may develop from such vorticity has not been identified. Even though any blunt object producing a detached, curved shock is adequate for the purpose of making the flow rotational at the shock, certain criteria were deemed essential for an experimental study of the stability of the shear layer. The shock generator needs:

1. To produce high levels of vorticity that remain constant over a large distance downstream of the shock.

2. To produce maximum vorticity as far from the body as possible, so as to eliminate possible interactions with the boundary layer.

The first constraint follows directly from the goals of the experiment, while the second one is necessary in order to keep the boundary layer decoupled from the shear layer.

Experimentation in the shock tunnel to optimize a shock generator over these criteria is not a viable option due to both cost and time constraints. Existing computational fluid dynamic (CFD) programs provide a much more efficient tool to perform this type of investigative work. One such program is the code developed by Candler for hypersonic flows in thermochemical nonequilibrium (Candler [1988]). This code was selected based on a history of successful simulation of T5 flows, see *e.g.*, Wen [1994] and Wen and Hornung [1995]. The goal of the present numerical investigation is therefore to use the code developed by Candler to study the vorticity field produced

by different shock generator geometries and to determine, based on the computed vorticity field, which of these basic configurations best satisfies the two experimental requirements listed above. Since several descriptions of this code are already available in the literature, only a brief description is presented here. In all of the simulations discussed here, nitrogen is used as the 'test' gas.

2.1.1 Description of the numerical method

Candler's code computes the flow field by solving the partial differential equations for the conservation of species, mass, mass-averaged momentum, vibrational energy of each diatomic species, and total energy. These coupled equations are solved using a modified Steger-Warming flux-vector splitting finite-volume method (MacCormack and Candler [1989]) to obtain a steady-state solution. The scheme is implicit, using Gauss-Seidel line relaxation. It has been implemented to simulate both viscous and inviscid flows, the latter being a special case for which the transport coefficients (viscosity, thermal conductivity, and diffusion) are all set to zero. The implicit scheme is not time accurate; a time-averaged steady-state solution is provided as output. Since no turbulence modeling is attempted in this code, the solution is always laminar.

Thus, this tool is of limited practical use in studying the stability of the shear layer produced by the shock and cannot be expected to answer the questions listed at the end of Chapter 1. Nevertheless, Candler's code is a valuable tool for characterizing many real gas flows in T5 and has often helped in obtaining quantitative flow-field information. In contrast, the only field information obtained experimentally is in the form of interferograms, which provide constant density contours in the flow.

2.2 Computing the vorticity field

The vorticity field plays a particularly important role in this study, as discussed in Chapter 1. Thus, the velocity field found by the code may be used to compute the vorticity distribution in the flow over prospective models and to determine the maximum vorticity levels produced by each one. The vorticity, defined as the curl of

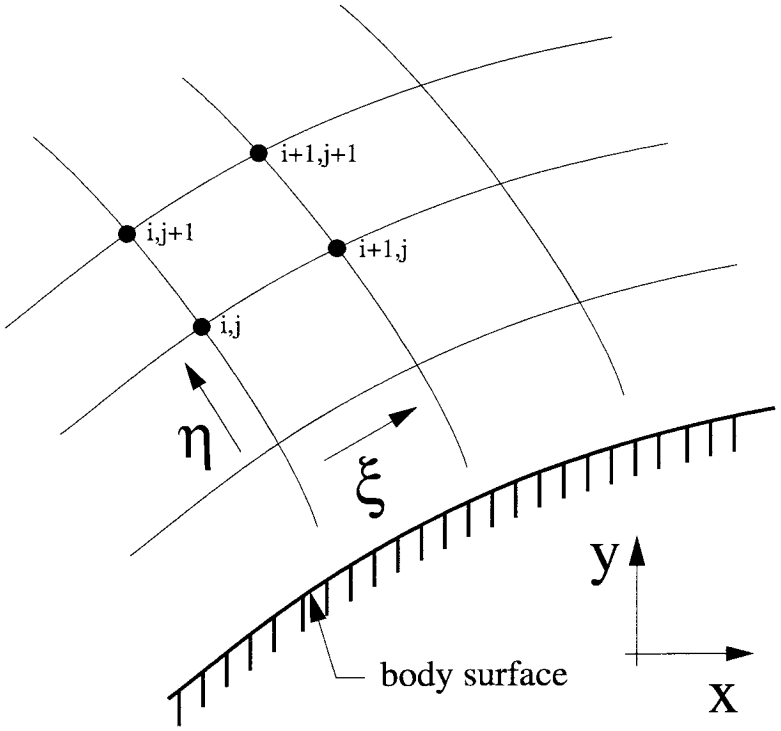

Figure 2.1. Grid coordinate system for vorticity calculations.

the velocity vector, $\nabla \times \tilde{u}$, may be computed directly from the output of the code. In two-dimensional planar flow, the vorticity is given as

$$\omega = \frac{\partial v}{\partial x} - \frac{\partial u}{\partial y}, \tag{2.1}$$

where $u = u(x, y)$ and $v = v(x, y)$. Since the grid is generally not Cartesian, the gradients in the general coordinate system are computed using the mesh metrics, to give

$$\omega = \frac{\partial v}{\partial \xi}\frac{\partial \xi}{\partial x} + \frac{\partial v}{\partial \eta}\frac{\partial \eta}{\partial x} - \frac{\partial u}{\partial \xi}\frac{\partial \xi}{\partial y} - \frac{\partial u}{\partial \eta}\frac{\partial \eta}{\partial y}, \tag{2.2}$$

where $u = u(\xi, \eta)$, $v = v(\xi, \eta)$, $\xi = \xi(x, y)$, and $\eta = \eta(x, y)$. ξ and η are the curvilinear grid coordinates shown in Figure 2.1, and x and y are the Cartesian counterparts. The resulting vorticity field forms the basis of the numerical study used to select a model to be used in the experimental investigation.

2.2.1 Geometries investigated

Several candidate geometries which appeared to be promising shock generators were studied in this numerical investigation:

1. a hemicylindrically blunted flat plate,
2. a square-faced flat plate,
3. a plate with a wedge-shaped leading edge (referred to as 'double-wedge'),
4. a hemispherically blunted cone, and
5. a hemicylindrically blunted wedge.

The following sections discuss the process used to investigate these geometries and some of the results obtained.

2.2.2 Grid layout and noise in vorticity computations

The flat plate with hemicylindrical leading edge generates a shock closely approximated by a hyperbola, which means that the point of maximum vorticity generation, occurring at a shock angle of approximately 60 degrees (*e.g.*, see Figure 1.3), is far off the surface of the body.

The free-stream conditions and physical dimensions used in this simulation are listed in Table 2.1 and are generally representative of the types of experiments performed in T5. Initially, a mesh of uniformly spaced grid points at the body in the

Table 2.1. Free-stream conditions used in the simulations.

Isothermal wall temperature:	297 K
Free-stream speed:	5000 m/s
Free-stream density:	0.04 kg/m^3
Free-stream temperature:	2260 K
Nose radius:	0.1 m
Length of plate:	0.5 m

i-direction (streamwise), and j-direction (normal to the body surface) was used to

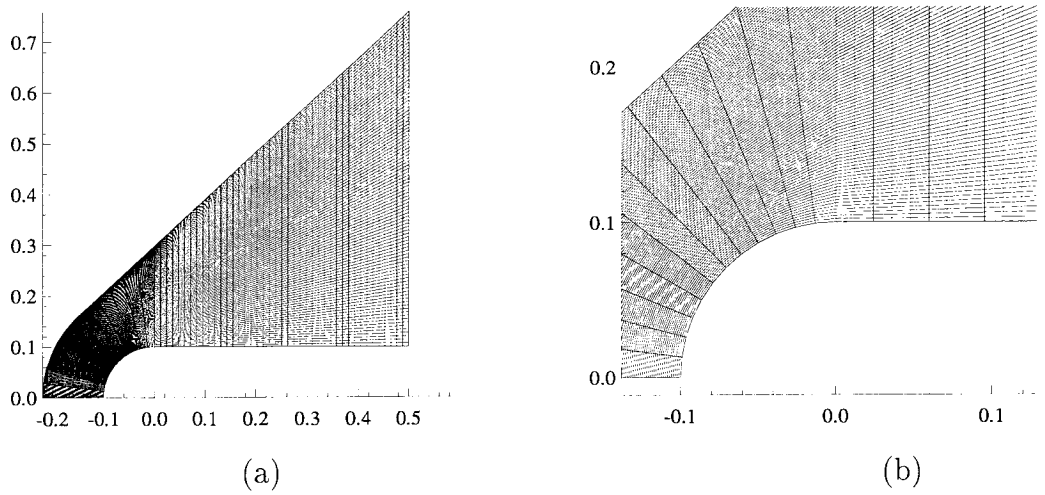

Figure 2.2. Initial grid system used, 56×100 cells. Flow is from left to right. Figure (b) is an enlarged view of the leading edge in (a).

compute the flow over the shock generator (see Figure 2.2). The resulting temperature field is plotted in Figure 2.3, where temperature contours are non-dimensionalized by the characteristic temperature of dissociation of N_2. The temperature contours clearly indicate the shock position and illustrate the poor resolution of the mesh near the shock front. Since the vorticity field is obtained by taking derivatives of the velocity field, discontinuities such as these are amplified and preclude any meaningful interpretation of the data, at least in that region of the flow.

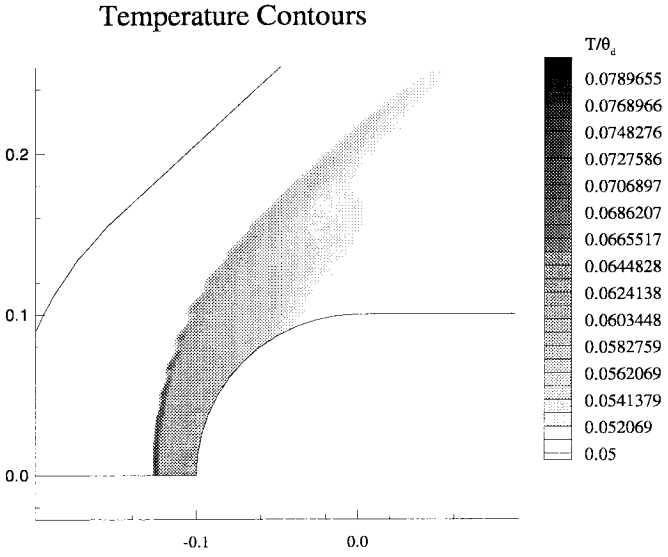

Figure 2.3. Contours of temperature, showing the shock position. The solution was found using the grid shown in Figure 2.2. The waviness at the shock surface is due to the poor resolution of the mesh in that region.

To improve grid resolution near the shock and to reduce the type of oscillations illustrated in Figure 2.3, the number of cells must be increased

significantly, especially in the i-direction. Also, in order to make the shock less diffuse, the number of cells in the j-direction must also be increased. We first seek to determine the extent to which the shock front is smeared by the uniform grid. To this end, the temperature profile across the shock is plotted as a function of cell number, using the solution shown in Figure 2.3, and is then compared to the temperature computed using a new grid having half the number of grid points in the j-direction. The result is shown in Figure 2.4. The figure shows that to capture the shock, from the beginning

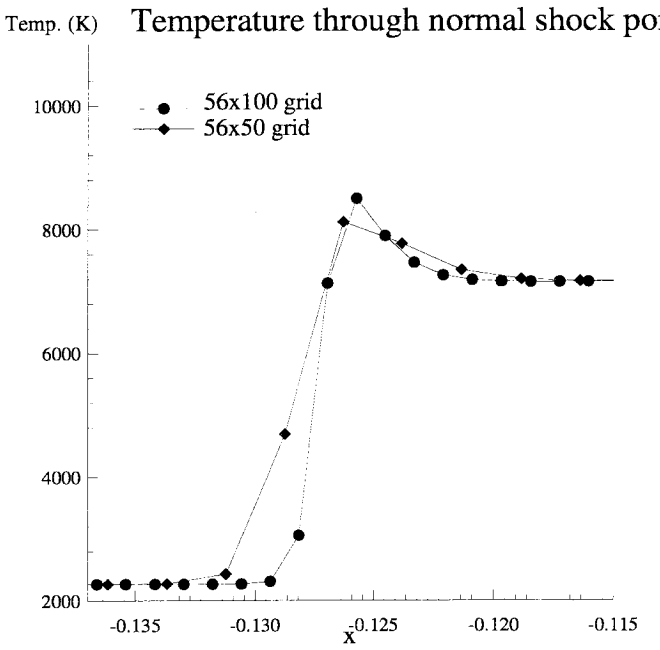

Figure 2.4. Temperature at center of cells, along stagnation streamline. The stagnation point is at $x = -1.0$.

of the rise in temperature to the peak after the shock, requires approximately four cells. Therefore, reducing the number of cells in the j-direction by a factor of two doubles the computed physical thickness of the shock from approximately 0.004 m to 0.008 m. The computed shock thickness is not physically representative and should be minimized as much as possible. Uniform mesh refinement would solve this problem, but the computational burden of this approach, beyond a certain limit, is prohibitive. Since the region of concern is confined to a small part of the domain, upstream and downstream of the shock, a computationally less intensive approach is to 'fit' the mesh to the shock, *i.e.*, refining it in the immediate vicinity of the shock. In order to

do this, however, *a priori* knowledge of the shock shape and position is necessary[1]. Using an analytical approximation to the shock shape, such as a hyperbola, to define the region of refinement is ruled out, as any deviation from the true shock position quickly reverts to the same problem of poor resolution *at* the shock and no universal analytical shock shape representation exists that may be applied to a wide range of shock generators.

2.2.3 Fitting the mesh to the shock

The best estimate of the shock position is obtained by using the solution from the coarse uniform grid computations already performed, so these results may be used to generate a fitted mesh. This new mesh can then be used to perform a flow computa-

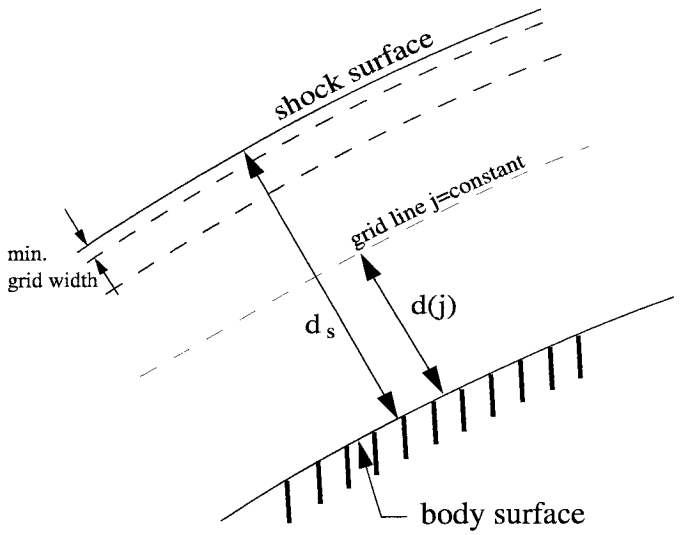

Figure 2.5. Nomenclature for shock-fitted grid.

tion that is better resolved near the shock, providing a better estimate of the whole vorticity field. Hence, the approach taken is twofold:

1. An initial run is performed, using a 'uniform' grid (as described in the discussion regarding Figure 2.2), for the purpose of finding the shock position at the given

[1]'Adaptive Mesh Refinement' techniques, which refine the mesh in regions of high gradients, would be ideal in providing the type of shock fitting discussed here, but such a tool has not been implemented in Candler's code at this time.

condition, and for the given model geometry, and

2. Based on this computed shock profile, the mesh is stretched in such a way that the spacing between grid points along rays normal to the shock decreases exponentially as the shock position is approached from both sides, down to a minimum specified width at the shock, as shown in Figure 2.5.

First, to find the shock position, the computed temperature field found with the uniform grid is used along with the following algorithm:

1. Along each ray where i is constant, the temperature at each j node is compared with the free-stream temperature starting at the free-stream end of the ray.

2. The node at which the temperature of the cell has jumped by 5% or more is recorded.

3. The xy-location within that cell where the temperature is exactly 5% higher than the free-stream value is found by interpolating the temperature linearly across that cell. This is the coordinate of the shock on that i-ray.

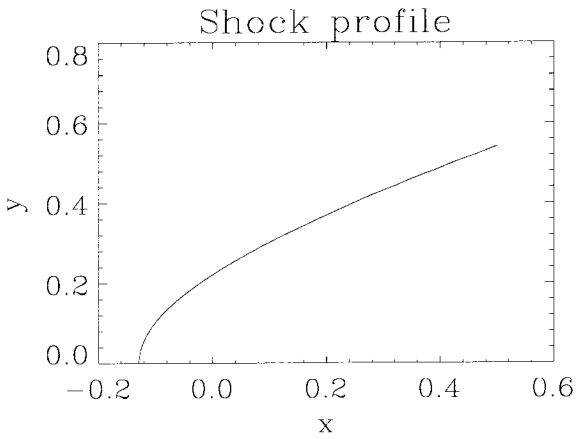

Figure 2.6. Shock profile for 800 × 100 grid.

The relation describing the way in which the new mesh is then stretched between this computed shock and the body is

$$d(j) = \left(\frac{e^{c\frac{j-2}{j_s-2}} - 1}{e^c - 1} \right) d_s, \quad (2.3)$$

where d_s is the distance between the shock and the body surface, j_s is the j-node at the shock, and c is a parameter that determines the minimum grid width at the shock. The nomenclature is specified in Figure 2.5. This procedure was used on the flow computed on a 800 × 100 uniform grid and generated the shock profile shown in Figure 2.6.

Although the large number of i-nodes used in this uniform flow computation accounted for a large reduction in the shock shape waviness (compared to Figure 2.3), small oscillations, still present, play a role in distorting the overall mesh fitted to this curve. A standard low-pass filter may then be used to smooth out the shock shape and reduce these oscillations. The Savitzky-Golay moving window data averaging scheme (Press *et al.* [1992]) was implemented here for this purpose.

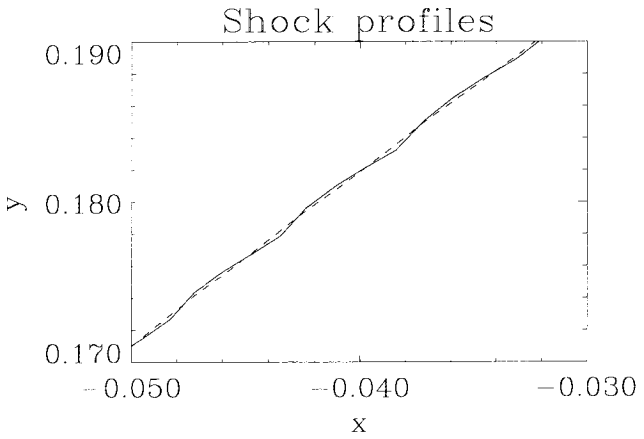

Figure 2.7. Enlarged view of shock profile of Figure 2.6, showing the effect of the filter. The initial shock is shown by a solid line; the filtered shock is shown by a dashed line.

The Savitzky-Golay algorithm recalculates the shock position by altering each (x, y) coordinate according to

$$x(i,j) = \frac{1}{2n+1}\Sigma_{k=j-n}^{j+n} x(i,k)$$
$$y(i,j) = \frac{1}{2n+1}\Sigma_{k=j-n}^{j+n} y(i,k),$$

where n sets the number of cells over which the moving window averaging is done. The effect of this smoothing on the shock shape is illustrated in Figure 2.7, which shows a magnified section of the shock shape of Figure 2.6. Note that the filtering operation does not create a shift in the shock position. The resulting mesh, nearly oscillation-free, is shown in Figure 2.8.

The procedure outlined in this section tacitly assumes that the converged shock position is unaffected by the mesh refinement. If this assumption is wrong, however, our choice that the grid spacing increases exponentially away from the point of minimum cell width will cause a rapid return to the shock thickness problem illustrated in Figure 2.4. The effect of the grid on the shock position must therefore be investigated.

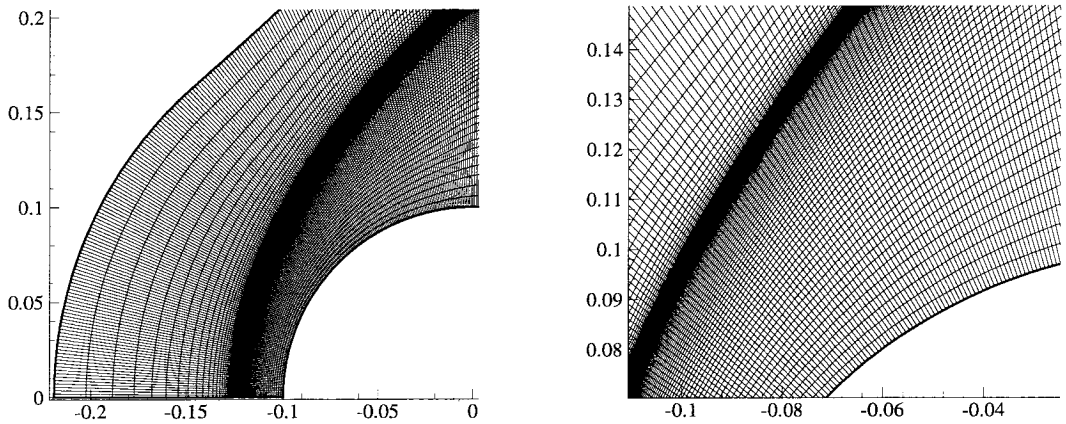

(a) (b)

Figure 2.8. Fitted grid generated using the smooth shock profile of Figure 2.7. Figure (b) is an enlarged view of the grid in (a).

2.2.4 Grid effect on shock shape and stand-off distance

Computations made on a mesh using the stretching technique discussed in Section 2.2.3 give significantly better resolution of all the flow properties in the immediate vicinity of the shock, as long as the region of maximum refinement is aligned with the converged shock location. One of the effects of varying the grid in this manner, however, is a perceptible shift in the converged position of the shock. That shift, which appears to reduce the stand-off distance by approximately 10%, has the undesired effect of offsetting the region of greatest grid density with the new shock position. The shocks found by both the uniform and fitted grids are shown in Figure 2.9, represented by a solid line and a dash line, respectively. A third computation, performed using a mesh fitted to the dash line shock, provides the shock shown by a dotted line.

Thus, the first solution found with the fitted mesh needs to be used to generate another mesh in order to take advantage of the maximum benefits of having a grid aligned with the shock, *i.e.*, to have the shock lie within a few cells of the region of minimum cell width. Of course, this third step increases the computational requirement further. Also, as shown in Figure 2.9, the change in the converged shock

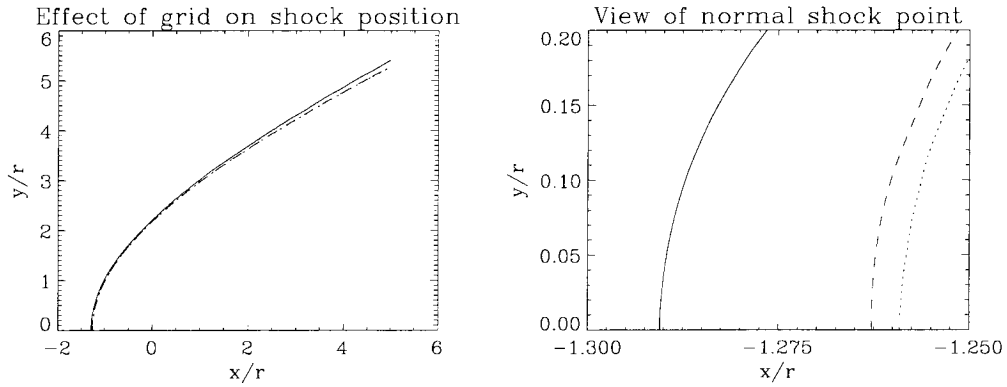

Figure 2.9. Computed shock position with fitted mesh vs. uniform mesh (note: the stagnation point is located at $x = -1.0$). The uniform grid solution is shown by a solid line; the first fitted mesh solution is shown by a dash line; the second fitted grid is shown by a dotted line.

stand-off distance that this additional step provides is only approximately 1.5% for the case of the hemicylindrically blunted flat plate. The vorticity contours obtained from the two-pass approach were in fact deemed sufficiently smooth to guide the investigation of the various models considered.

2.3 Results: vorticity distribution over selected models

The two-pass approach described above was performed to compute the vorticity field over the five candidate models listed at the beginning of the chapter. For the blunt wedge model, multiple passes were performed to refine the mesh around the converged shock profile. The results are discussed in the following sections.

2.3.1 Vorticity distribution over a hemicylindrically blunted flat plate in hypervelocity flows

The resulting vorticity distribution for the hemicylindrically blunted flat plate under the conditions listed in Table 2.1 is shown in Figure 2.10. These results show that a blunt flat plate creates non-dimensional vorticity peaks of order unity immediately

downstream of the shock. Note that in this case, the vorticity is non-dimensionalized by the plate radius, as opposed to the radius of curvature of the shock at the stagnation point, as was done in Section 1.2. Lines of constant pressure over the plate are shown in Figure 2.16.

Although the peak vorticity is indeed generated far from the surface of the plate, the vorticity level diminishes rapidly along streamlines, as expected from the results of Section 1.2.2 for a homenthalpic flowfield with pressure diminishing along streamlines. This shock generator is therefore not optimal in a study of the shear layer stability. The model, nonetheless, provided a good starting point for this investigation and

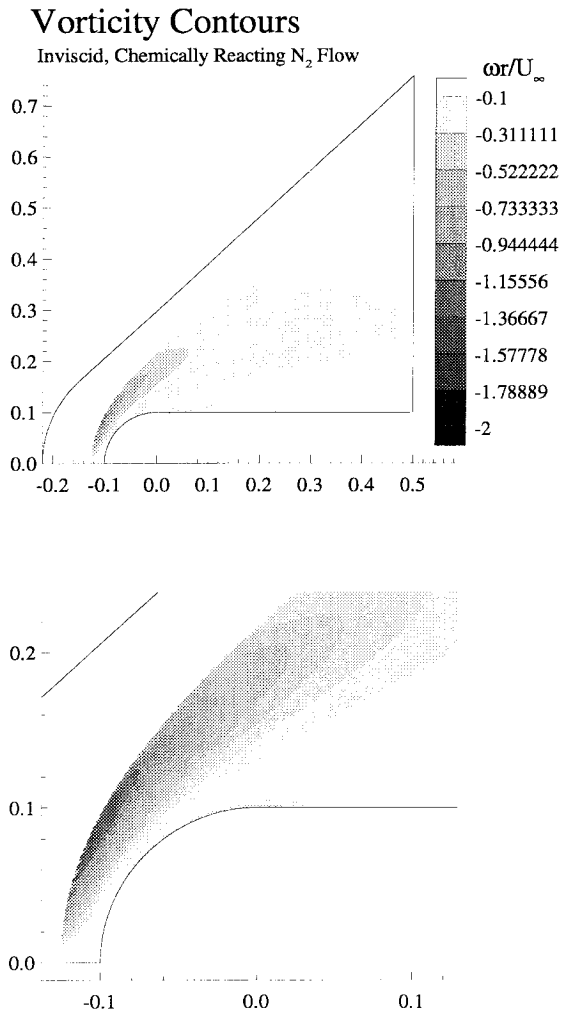

Figure 2.10. Vorticity contours around a hemicylindrically blunted flat plate, computed using a shock-fitted grid.

was helpful in developing the shock-fitted mesh procedure with which other shock generators were investigated.

2.3.2 Vorticity distribution over a rectangular flat plate and a double-wedge shock generator

The hemicylindrically blunted flat plate is inadequate because the part of the flow that is rotational is confined to a small region downstream of the shock. In order to raise the peak vorticity at the shock, the next two shock generators listed at the beginning of the section were considered: the rectangular flat plate and the double-wedge (see Figure 2.11) . The purpose of investigating these two models was to

Figure 2.11. Two of the five shock generator geometries considered: a rectangular plate and a double-wedge.

determine whether a sharp corner could create a rapid expansion which would bend the shock locally, thus creating a region of high vorticity far from the body surface. The rectangular plate's sharp 90° corner, for example, generates an expansion fan which bends the detached shock. Since this occurs relatively close to the body surface, a 'double-wedge' geometry was also considered in an attempt to move the point of maximum vorticity generation further away from the body. The double-wedge shifts the point of maximum vorticity generation outward by using the angle separating the oblique shock from the body surface.

The vorticity contours for the double-wedge model are shown in Figure 2.12. Since the leading edge of the wedge and of the attached shock both have radii of curvature of zero, for the sake of comparison the vorticity is non-dimensionalized by the radius of the plate of Figure 2.10. The vorticity peak is not substantially different from that of the hemicylindrically blunted flat plate, and suffers from the same shortcomings: the flow does not remain rotational very far downstream of the shock. The rectangular

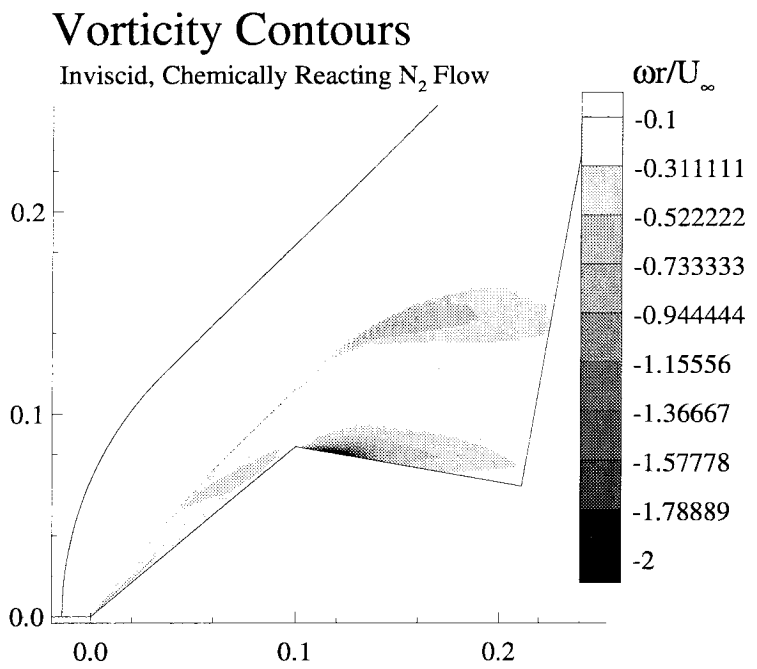

Figure 2.12. Vorticity contours around the double wedge.

plate produces similar vorticity contours. For these reasons, both of these two models were not selected for the experimental investigation.

The three models discussed so far, the hemicylindrically blunted flat plate, the rectangular flat plate and the double-wedge, thus support the results of Chapter 1:

1. It is difficult to generate high levels of vorticity at a shock by controlling its shape and curvature, and

2. In flows where the pressure along streamline drops away from the shock, so does the vorticity.

Thus, the next two models investigated were selected specifically because they keep the density ratio high across a large section of the shock profile and have relatively constant pressure fields downstream of the shock.

2.3.3 Vorticity generation over a blunt cone and a blunt wedge

Blunt cones and wedges produce pressure fields which remain roughly constant along streamlines, so that by the results of Section 1.2.2, whatever vorticity generated at the shock is convected downstream with the flow. There exist important differences

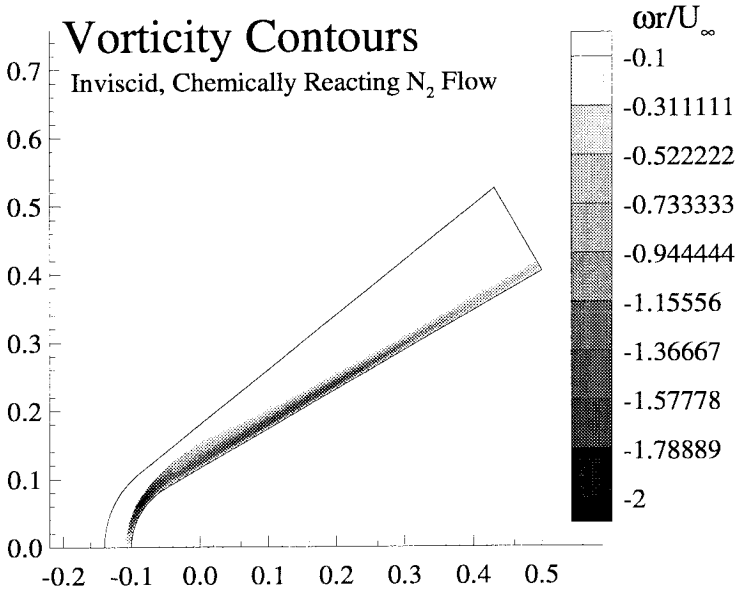

Figure 2.13. Vorticity contours around a blunt cone.

between the flow over axisymmetric bodies and over two-dimensional planar bodies, however, that need to be discussed at this point. The derivation of the results of Section 1.2.2 assumed early on that the flow was planar, so that the vortex stretching terms, $(\tilde{\omega} \cdot \nabla)\tilde{u}$ of equation (1.19), played no role in the final result.

A similar simplification was performed in the derivation of equation (1.16), which described the mechanism of vorticity generation at a curved shock in two-dimensional, planar flows. Following this result, Hayes and Probstein [1966] derived a further result for the vorticity field behind a curved shock over a concentric sphere (axisymmetric

flow) and found that it is given by

$$\omega = \frac{-U_\infty \left(1 - \frac{\rho_2}{\rho_1}\right)^2}{\frac{\rho_2}{\rho_1} R_s^2} R \sin\theta \,, \tag{2.4}$$

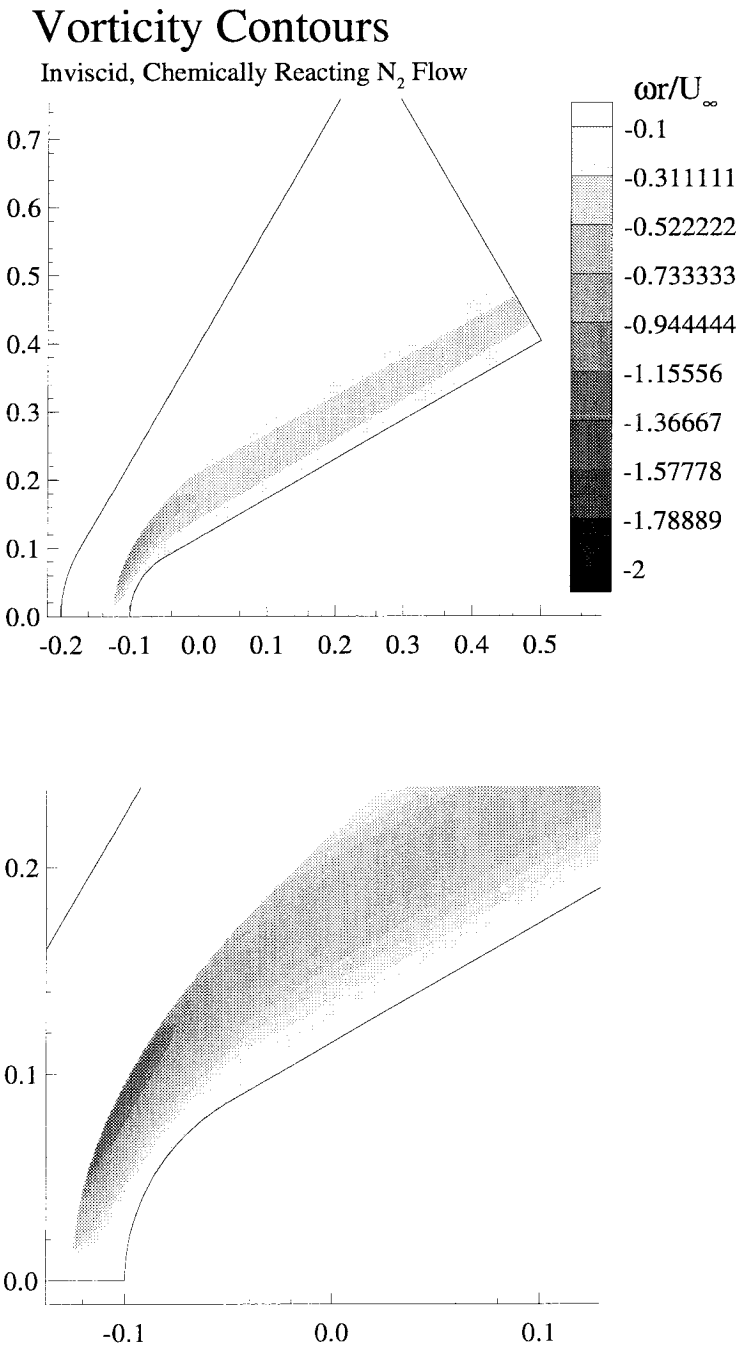

Figure 2.14. Vorticity contours around blunt wedge.

where R_s is the radius of the spherical shock; R is a spherical radius between the body and the shock; and θ is the polar angle from the upstream axis. Even though many simplifications were made in this derivation (*e.g.*, concentric, spherical shock and body; constant density field downstream of the shock), it shows that the vorticity field in axisymmetric flows differs significantly from that in planar flows. For instance, whereas an inviscid planar flow next to the body is irrotational, the vorticity field in axisymmetric flow is never zero except on the axis where $\theta = 0$.

The stretching of vortex lines in axisymmetric flow has an intensifying effect on the vorticity level along streamlines, as can be seen by comparing the computed flows over a cone with those over a wedge (Figures 2.13

and 2.14, respectively). This may or may not have an effect on the overall stability of the shear layer. The flow over these two shock generators, a blunt wedge and blunt cone both with nose radii of 0.1 m and half-angles of 30°, was computed. The free-stream flow conditions are those listed in Table 2.1. The vorticity contours found for each model are shown in Figures 2.13 and 2.14. Again, vorticity has been non-dimensionalized by the nose radius. It is clear from these figures that these shock generators represent a significant improvement over the previous three models discussed so far. The vorticity levels in both cases are appreciably higher than the other models, but more importantly, they remain high over a large region of the flow. For the cone, the vorticity layer has peak vorticity very close to the body, and would clearly eventually become 'swallowed' by the boundary layer (in viscous flows) at some point downstream, as found by Stetson *et al.* [1984] and others. So, although the shock generated by a blunt cone produces an intense shear layer that may well become unstable, its coupling with the boundary layer makes this model inappropriate for the present experimental study.

The wedge model, however, satisfies one requirement important in the experimental study of the shear layer instability, namely that the vorticity layer remain separated from the surface of the body throughout the flow.

To see how the vorticity and the product of density and temperature correlate along streamlines, both are plotted along streamlines in Figure 2.15. The same is done in Figure 2.16 for the flow over the hemicylindrically blunted flat plate whose vorticity levels, shown in the contours of Figure 2.10, dropped rapidly downstream of the shock. In these calculations, the flow is inviscid and chemically non-reacting to satisfy the assumptions made in Section 1.2.2. The streamlines are plotted using a commercial data visualization software (Tecplot) which uses a predictor-corrector algorithm for the calculation of the streamtraces. Four steps are taken within each cell (in the direction of the local velocity vector) to find the best line of tangency with the vector field. The flow properties, in this case the non-dimensional vorticity and the product of density and temperature, may then be plotted along those streamlines. Fluctuations may be observed near the shock because of the large gradients

(especially in vorticity) in that region. Kinks in the curves are due to poor local grid resolution, which is not perfectly aligned with the shock in these computations. The curves showing the ratio $(-\omega r/U_\infty)/(\rho T)$ are indeed roughly constant after the shock, as expected for homenthalpic flows. To appreciate the effect of thermo-chemistry on this correlation, the computation was repeated (using the same free-stream conditions as Figure 2.15), this time allowing for the gas to dissociate and vibrate. The result is presented in Figure 2.17. Note the stand-off distance which is reduced by a factor of nearly 2 due to the increased density ratio across the shock, compared to Figure 2.15. Correspondingly, the vorticity level produced at the shock is higher than in the frozen case. The vorticity drops down slightly along streamlines, however, further downstream. Although the flow in this case is still homenthalpic, the endothermic balance is not accounted for in the derivation presented in Section 1.2.2, so that the correlation with ρT is no longer expected to be strictly valid. The initial rise of $(-\omega r/U_\infty)/(\rho T)$ along streamline A, and subsequent slow decrease correspond to initial rapid dissociation and subsequent slow recombination.

2.4 Selection of an experimental model

Based on this survey of different model geometries, the best model for an experimental study of the instability of the shear layer produced by a curved shock is a blunt wedge. Such a shock generator produces high levels of vorticity, depending on the density ratio at the shock, and the flow remains rotational far downstream of the shock, along streamlines. Furthermore, the region of high vorticity is far off of the surface of the body, so that the shear layer is separated from the boundary layer. Such a model is therefore ideally suited for tests in T5, where the flow conditions may be varied to provide a large range of vorticity throughout the shear layer.

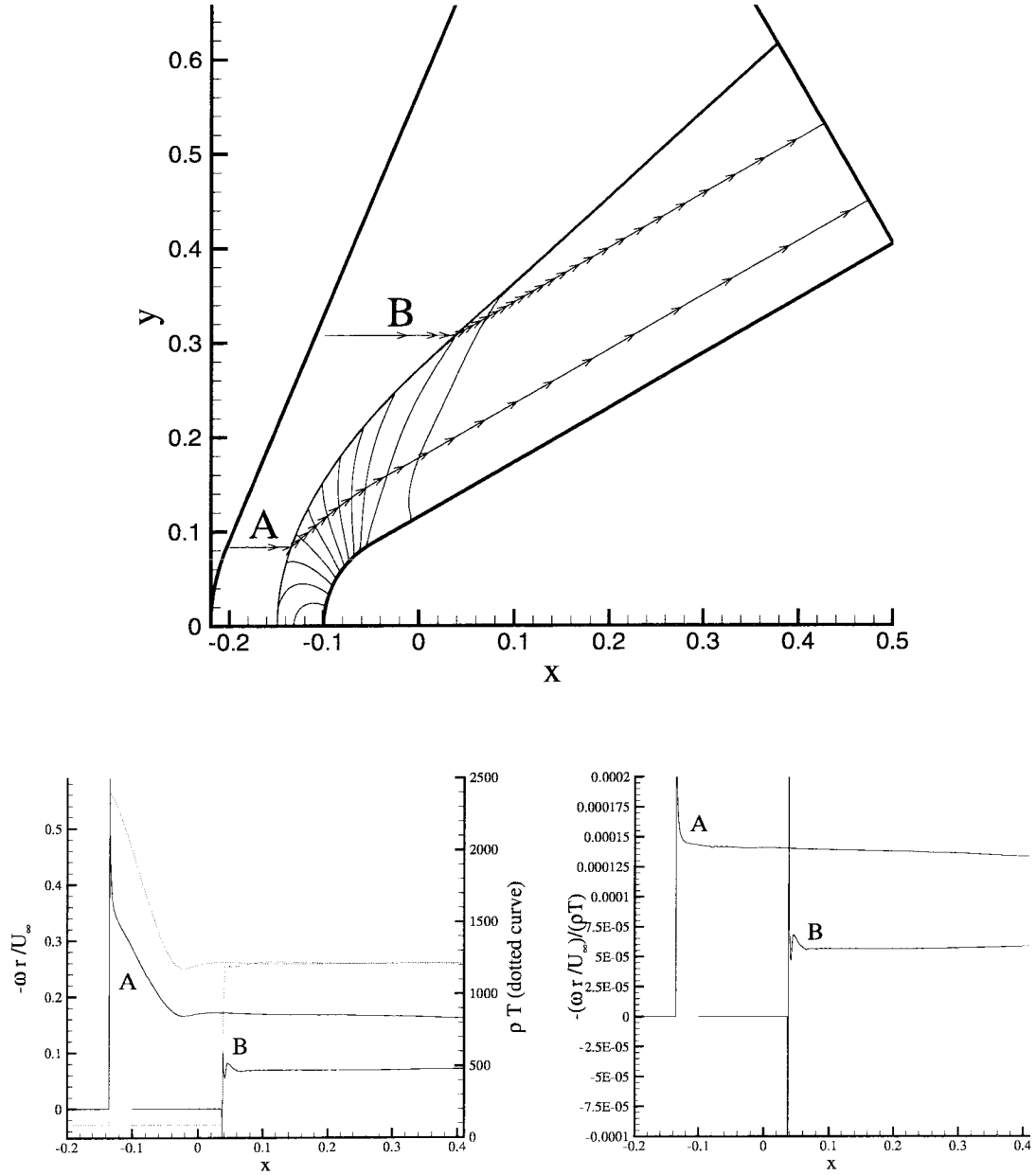

(a) (b)

Figure 2.15. Contours of constant pressure in frozen flow over a blunt wedge, with two streamlines. The free-stream conditions are: $U_\infty = 5000\text{m/s}$; $\rho_\infty = 0.04\text{kg/m}^3$; $T_\infty = 2260\text{K}$. The lower left figure (a) plots the non-dimensional vorticity and the product ρT as a function of streamline abscissa, for both streamlines. The lower right figure (b) shows the ratio of those two quantities, which should be constant for homenthalpic flows according to the results of Section 1.2.2.

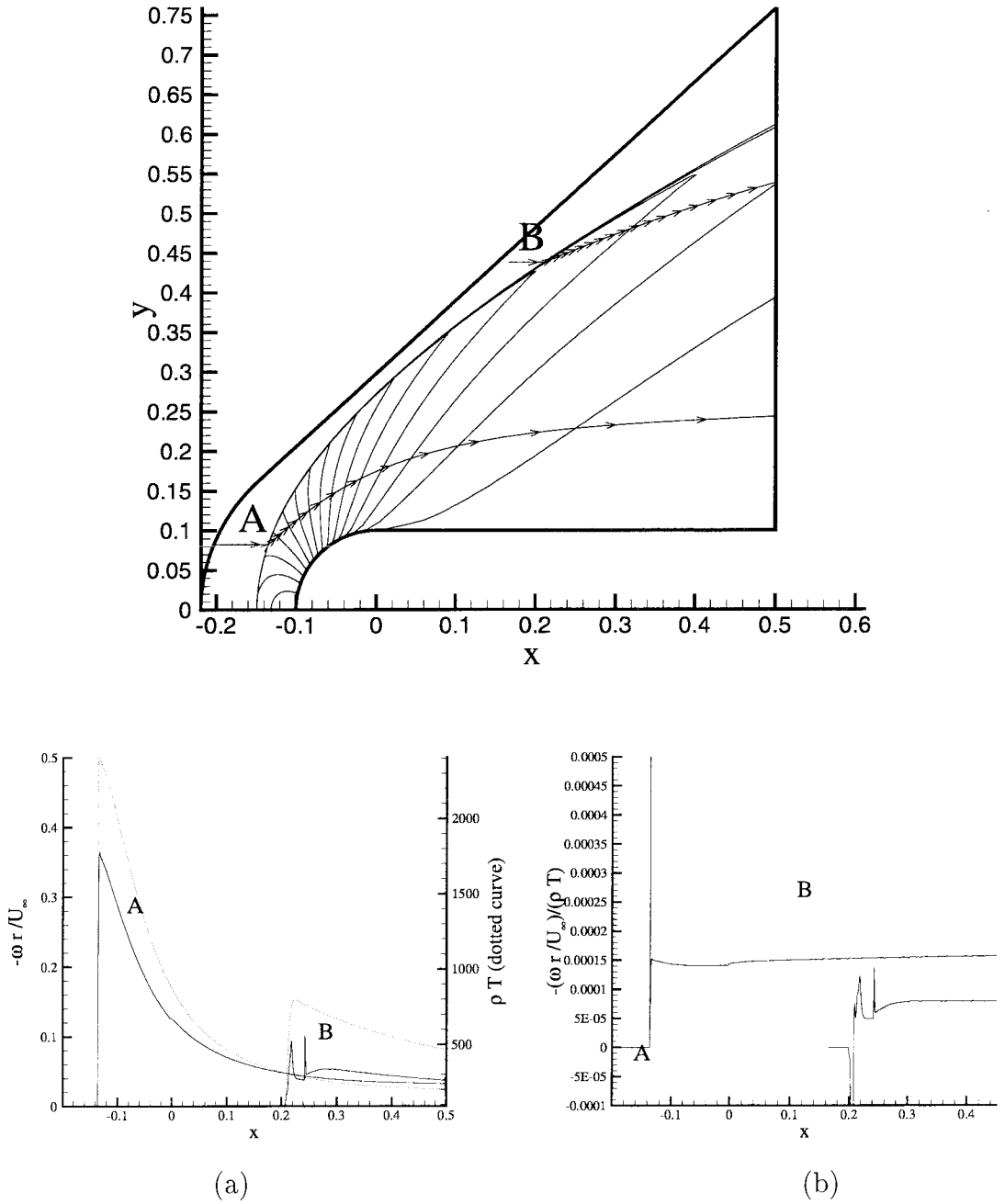

Figure 2.16. Contours of constant pressure in frozen flow over a hemicylindrically blunted plate, with two streamlines. The free-stream conditions are: $U_\infty = 5000\text{m/s}$; $\rho_\infty = 0.04\text{kg/m}^3$; $T_\infty = 2260\text{K}$. The lower left figure (a) plots the non-dimensional vorticity and the product ρT as a function of streamline abscissa, for both streamlines. The lower right figure (b) shows the ratio of those two quantities, which should be constant for homenthalpic flows, according to the results of Section 1.2.2.

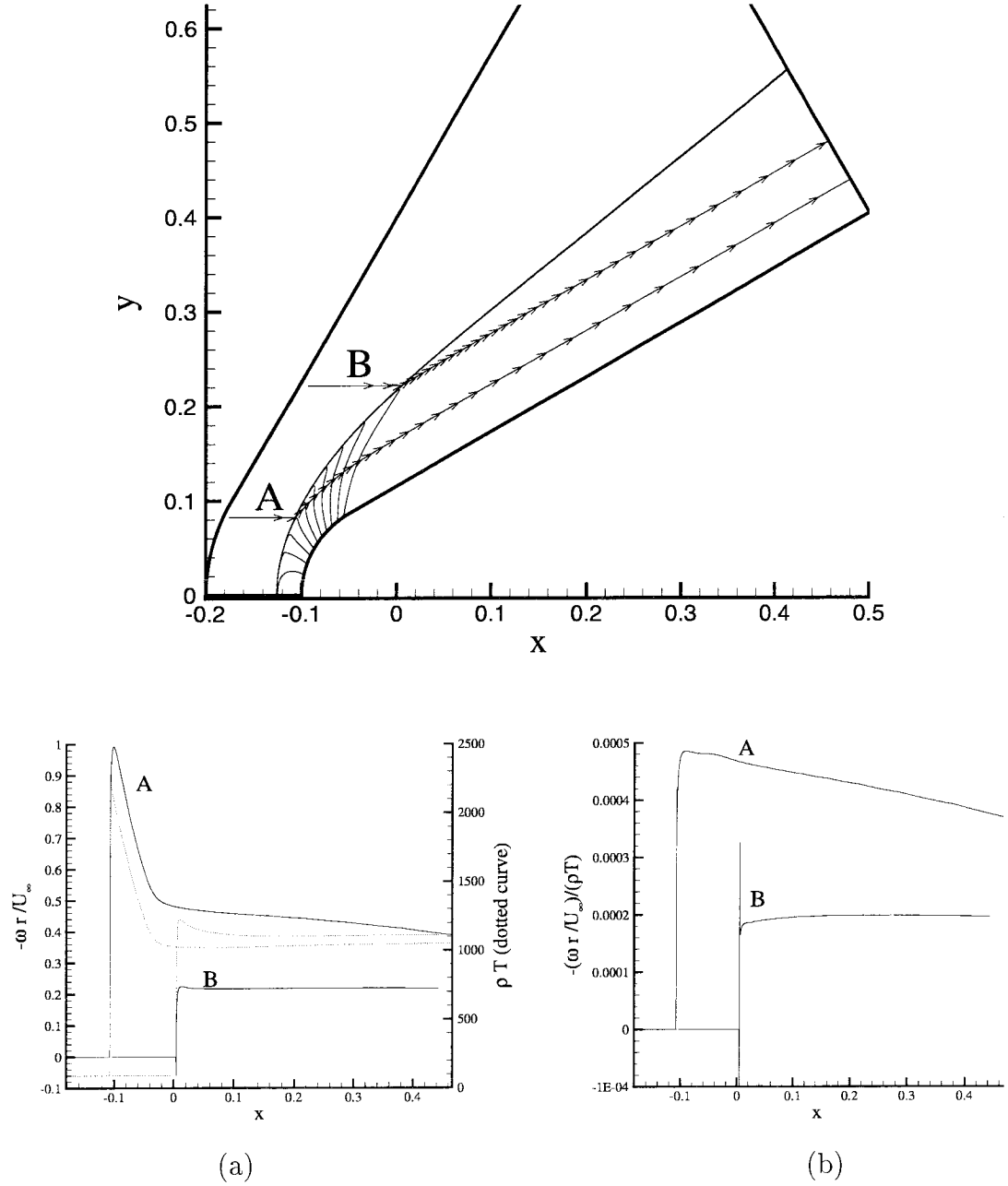

Figure 2.17. Contours of constant pressure in reacting flow over a blunt wedge, with two streamlines. The free-stream conditions are: $U_\infty = 5000\text{m/s}$; $\rho_\infty = 0.04\text{kg/m}^3$; $T_\infty = 2260\text{K}$. The lower left figure (a) plots the non-dimensional vorticity and the product ρT as a function of streamline abscissa, for both streamlines. The lower right figure (b) shows the ratio of those two quantities.

This page is intentionally blank.

Chapter 3 Experimental Techniques

3.1 Introduction

Now that a suitable shock generator has been identified, the experimental program developed and carried out is presented.

The experimental techniques used in this study may be subdivided in the following way:

1. **Flow visualization.** This is the principal diagnostic tool used in the study. A new streakline visualization technique was developed; holographic interferometry was also used.

2. **Surface heat transfer and pressure measurements.** These were recorded for most experiments, but their role within the scope of the study is secondary.

3. **The T5 Light Gas Gun modification.** An available modification to the layout of the shock tunnel, transforming T5 into a light gas gun, was used for an important series of experiments during this study. Shadowgraphy was used to record the flow, and electronic triggers were used to measure speed.

Discussion of these experiments is divided into two main parts: (1) the results of experiments performed on a blunt wedge (two-dimensional study), and (2) the results of experiments performed using projectiles in the T5 Light Gas Gun facility (high density ratio study).

3.2 Model and experimental setup for the two-dimensional, planar flow study

Based on the numerical results of Chapter 2, a hemicylindrically blunted wedge was selected for the experimental study. The following design features were required of the test model:

1. Removable cylindrical leading edge. This requirement allows the relatively inexpensive machining of a series of leading edges of varying radii (the only characteristic length of the model applicable to this study).

2. Aspect ratio as large as possible. This is needed to satisfy the 2D approximation.

3. Flexible instrumentation setup. The model should be able to accommodate various instrumentation arrangements, both in terms of thermocouples and pressure transducers.

4. Adjustable wedge half-angle. Since the flow around a wedge is symmetric (provided that the cylindrical leading edge extends to both sonic lines), only a half wedge needs to be used. This wedge may then be rotated about the flow axis to simulate different half angles.

5. Vertically adjustable. The position of the wedge needs to be adjustable to minimize interference with the nozzle expansion fan.

6. Sealed openings. In order to safeguard the electronic connectors inside the model, all openings should be sealed with o-rings.

3.2.1 Description of the experimental model

Based on recommendations made by Bélanger [1993], who reported difficulties with pressure measurements in T5 on aluminum models due to ringing, the model was made of low carbon steel. A leading edge with radius of 3.5 cm (1 3/8 in) was arbitrarily selected for the initial run of experiments. This leading edge was instrumented with

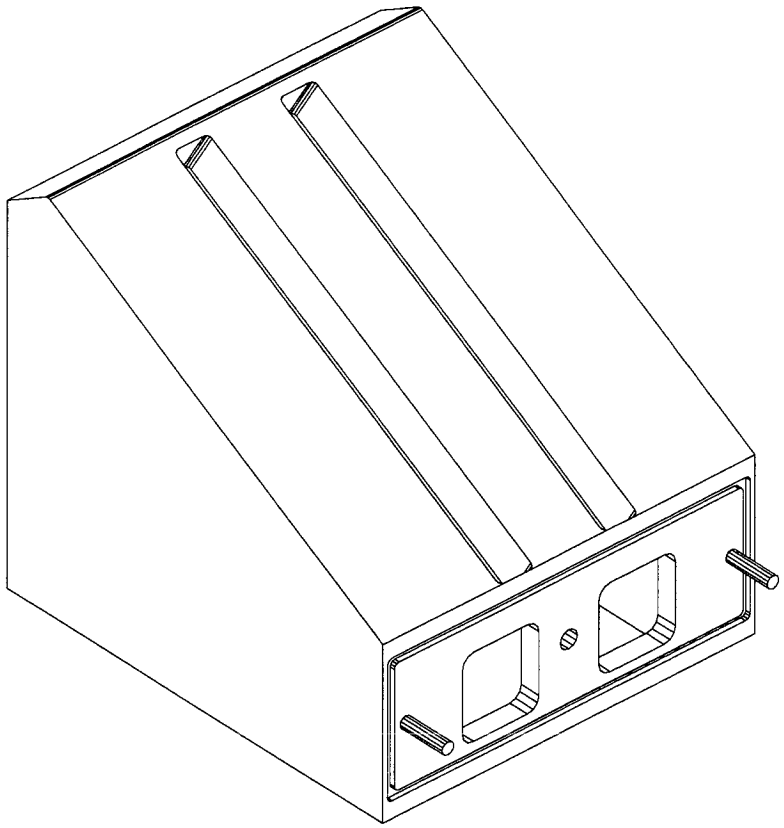

Figure 3.1. Main body of model, showing the openings for the instrument blocks and the removable leading edge setup, with o-ring grove and wire cavities.

heat transfer gauges and pressure transducers. Two additional (non-instrumented) leading edges were subsequently manufactured and had radii of 1.9 cm (3/4 in) and 6.4 cm (2.5 in), respectively.

Two instrumentation blocks were designed to fit into slots machined on the top surface of the model. These blocks can be changed between experiments with minimum impact on the rest of the setup to provide maximum flexibility concerning the type of surface measurements taken during a test. They are located symmetrically off of the model's centerline in order not to be affected by the streakline flow visualization technique, described later. A sketch of the model's main body is shown in Figure 3.1 and illustrates the instrumentation slots and the attachment surface for the leading edge. Since the pressure transducers used in this experiment were the most bulky instruments to be accommodated (DSP model 113A26, over 3 cm long and 1 cm in diameter), the blocks were designed around them. The nominal dimensions of

the blocks are 22.86 cm (9 in) by 1.9 cm (3/4 in), and they are 2.54 cm (1 in) thick (a sketch of the block manufactured for the pressure transducers is shown in Figure 3.2). Smaller instruments, such as thermocouples, are then easily supported by blocks of the same dimensions. In order to feed the instrument wires through a slot below the block, a small footprint micro-D connector was used. Each block is therefore connected to the main body wiring by its own connector and can be removed or altered between runs.

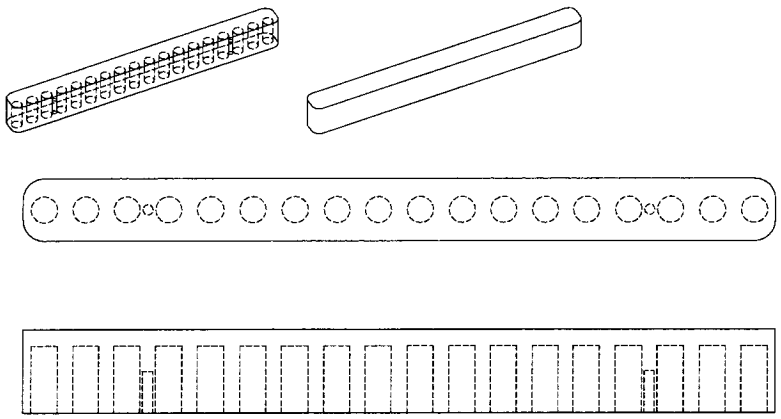

Figure 3.2. Instrumentation block used to house the pressure transducers. The surface of the block has a pressure tap hole 1.6 mm in diameter (not shown) for each transducer. The size of the transducers (shown by dash lines) explains why the instrumentation blocks are so large.

3.2.2 Difficulty with planar flow studies

The two-dimensional flow assumption usually made in experimental planar studies is never strictly valid. This is of particular concern in a facility such as T5, where a nozzle (with circular exit plane) supplies the flow in which the experiments are run. In the current experiment, the assumption is violated for two reasons:

1. End effects due to the model's limited span,

2. Divergence of the conical nozzle flow.

End effects

End effects refer to the three-dimensionality that arises because of the finite spanwise extent of the model. By investigating the flow near the centerline of a model and by maximizing aspect ratio, however, these effects may be minimized. In the present

case, the model's span was limited to eight inches by the nozzle expansion fan (see Section 3.2.3 for a discussion of this effect). The chord then varies depending on the leading edge radius. For the three leading edges used in this experiment, the chord varied from 28.7 cm (11.3 in) (for the 1.9 cm radius leading edge) to 26 cm (10.24 in) (for the 6.4 cm radius leading edge), giving aspect ratios varying between 0.71 and 0.78. This suggests that results obtained far from the leading edge (and especially away from the centerline), are suspect and should be interpreted with care. For this reason, the streakline flow visualization method is used only along the model centerline.

Divergence of the conical nozzle flow

The conical nozzle used in T5 has an included angle of 14°. This nozzle is preferred for many experiments because of its ability to accommodate a large range of operating conditions. It avoids the problem of off-design operation associated with contoured nozzles (Rousset [1995]), trading it instead for flow divergence at all conditions. An important effect of this flow divergence is to increase spanwise flow over the model. This is difficult to quantify accurately, but it is possible to estimate the deviation from uniform flow at any point on the model. For instance, on the plane defined by the nozzle centerline and the model span, the flow deviation along the span of the model is given by

$$\begin{aligned} v &= \frac{x}{l}u \,, \\ \theta &= \arctan(x/l) \,, \end{aligned}$$

where v is the spanwise component of velocity; u is the flow speed along the centerline; l is the distance between the leading edge and the source point of the nozzle (*e.g.*, that distance is 122 cm when the leading edge is aligned with the exit plane of the nozzle); x is the distance along the model span; and θ is the angle between the flow vector and the nozzle centerline. Hence, on the outer edge of the model span, even with the model located at the closest point to the flow source (about 2 cm inside the

nozzle during a shot), the flow deflection is only 4.8°.

The effect of conical flow divergence is considered to be a significant issue in many flow studies. In the case of the current study, which is aimed at exploring the instability of the shear layer produced by the shock curvature, flow divergence is a minor inconvenience that does not affect the results obtained.

3.2.3 Interference with the nozzle expansion fan

As the flow reaches the end of the nozzle, the exit edge of the nozzle generates an expansion fan which propagates inward and may interact with the flow around the model. The expansion fan comes off the end of the nozzle at the Mach angle

$$\mu = \arcsin(1/\mathrm{M}_\infty) \tag{3.1}$$

with respect to the nozzle wall. Thus, for a typical T5 run generating Mach 5 flow, the expansion fan forms a cone inside the test section with a half angle of 4.5°. This effect is made worse with the use of the contoured nozzle, since the flow is axial at

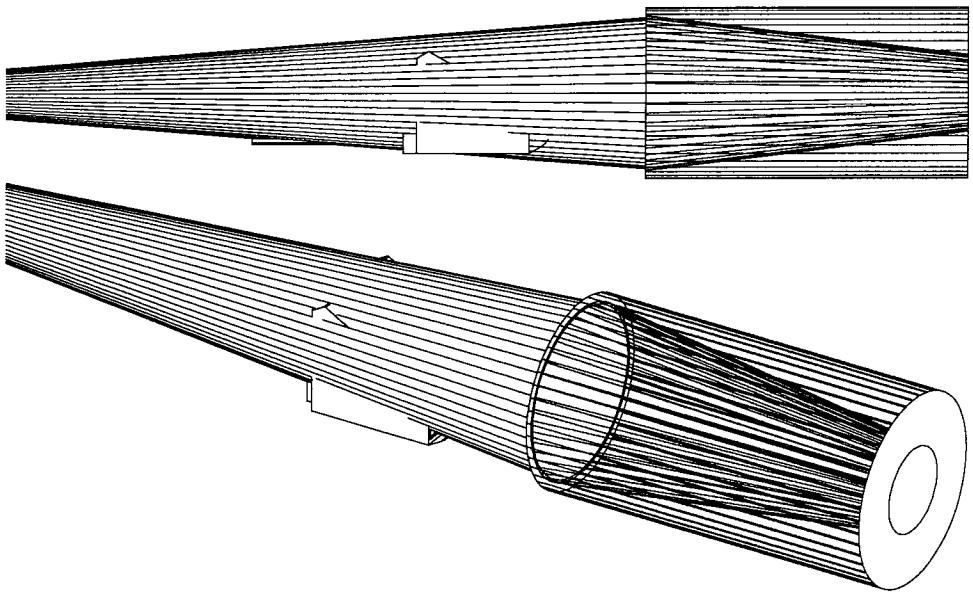

Figure 3.3. Worst-case effect of the interaction between the conical nozzle expansion fan and the wedge model. Note that the full span of the leading edge is contained within the expansion cone.

its exit plane.

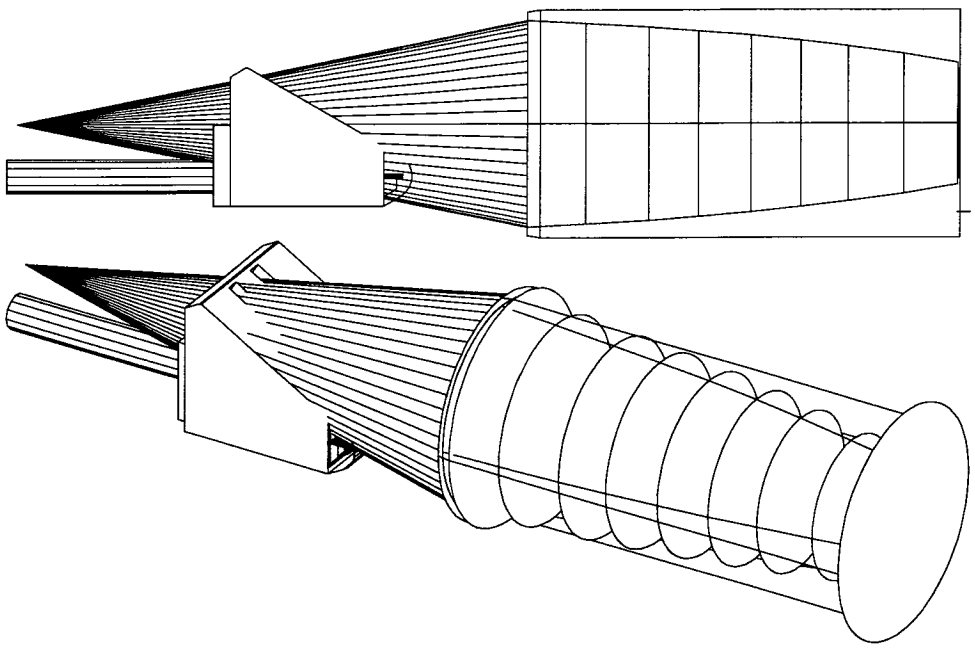

Figure 3.4. Worst-case effect of the interaction between contoured nozzle expansion fan and the wedge model. Note that in this case, a large section of the model lies outside the leading wave of the expansion fan.

To estimate where the interaction of this fan with the model occurs, the distance between the nozzle and the leading edge at the time of the shot is required. This distance depends on the maximum recoil of the shock tunnel to which the nozzle is attached. The recoil of the shock tunnel, of course, is due to the free piston mode of operation of the facility. Adding the nozzle recoil to the initial distance between the nozzle exit plane and the model's leading edge gives the distance during the shot. Table A.2 (in Appendix A) lists this distance, along with other shock tunnel data, for all test runs performed. For each nozzle, the largest distance separating the leading edge from the nozzle exit plane is listed in that table, and can be used to get a bound on this effect.

For the case of the conical nozzle, the maximum distance between the leading edge of the model and the nozzle exit plane is 19.3 cm (7.6 in) and for the contoured nozzle, this distance is 17.4 cm (6.8 in), obtained in shots 1857 and 1327, respectively[1]. The

[1]There are various reasons why this distance varies from shot to shot. As mentioned earlier,

expansion fan leading wave for both of these shots is illustrated in Figures 3.3 and 3.4, respectively.

Thus, even for the worst-case scenario, the model falls almost entirely within the expansion cone when the conical nozzle is used. The region of no interaction is slightly reduced by the shock over the model, which intersects the expansion fan. Note that the average nozzle-to-model distance for all the shots performed with the conical nozzle is only 10.2 cm, about half of what is illustrated in Figure 3.3, so that the actual effect of the expansion in any given shot is significantly less than what is shown there.

Another important factor affecting the region of interaction between the nozzle expansion and the model is, of course, the model span. A balance must be struck between reducing end effects by maximizing span, and reducing nozzle fan interaction by minimizing span. It was felt that 20.3 cm, or 2/3 of the nozzle exit diameter, would provide the best compromise, because it is the largest length that can reasonably fit within the expansion cone for most operating conditions.

3.3 Planar flow study: test conditions and diagnostics

As has been pointed out in Section 1.2.2, we wish to exploit the high density ratios associated with dissociation after a shock in hypervelocity flow to generate high vorticity. The density ratio achieved in T5 flows depends mainly on the reservoir enthalpy. Accordingly, we choose three conditions: low, intermediate, and high enthalpy. These conditions are listed in Table 3.1.

nozzle recoil is one factor affecting this. Other factors are the desired optical diagnostics, which may require that the model be translated forward or backward to provide a specific field of view. The leading edge radius on a large model is also important, as the model will not always fit inside the nozzle before the shot to compensate for the recoil. Ideally, for studies that are not concerned with visualizing the stagnation region of the flow, the nozzle leading edge should be aligned with the exit plane of the nozzle, after recoil. The values used here are *maximum* distances obtained for all the shots, and thus illustrate the worst-case scenarios. Average values for this distance are significantly lower.

Table 3.1. Nominal T5 conditions and approximate density ratios for planar flow study.

	h_{res}	P_{res}	M_∞	U_∞	ρ_∞	T_∞	ρ_2/ρ_1
Condition 1	11 MJ/kg	20 MPa	5.7	4300 m/s	0.018 kg/m^3	1450 K	8.5
Condition 2	20 MJ/kg	27 MPa	5.0	5500 m/s	0.018 kg/m^3	3020 K	10.8
Condition 3	4 MJ/kg	14 MPa	6.2	2700 m/s	0.036 kg/m^3	580 K	6.2

3.3.1 Flow visualization — overview of the methods used for planar flow

The T5 flows were studied with two flow visualization techniques. A new method for streakline visualization was developed and is described in detail in Chapter 4. An existing holographic interferometer (Sanderson [1995]) was also used. The small field of view of this interferometer made it necessary to cover the flow field of the present setup by taking several pictures in successive shots. Figure 3.5 shows an example of an interferogram taken near the leading edge of the 3.5cm-radius model. The fringes approximately represent lines of constant density and may be used to identify regions of high mixing where the shear layer has become unstable.

3.4 Experimental setup for flows with large density ratios

During the course of the experiments with the hemicylindrically blunted wedge, Hornung [1998] found, in a numerical study of the problem, that density ratios of about 15 are required for the shear layer on such a model to become unstable[2]. Such high density ratios cannot be achieved in hypervelocity flows generated by a nozzle expansion because the amount of energy that goes into dissociation after a shock wave is

[2]Note that the disturbances in the T5 nozzle flow are significantly larger than those used in the numerical investigation. Instability in the shear layer may therefore develop at lower density ratios in the experimental flows. This important numerical investigation is discussed in more details in Chapter 5.

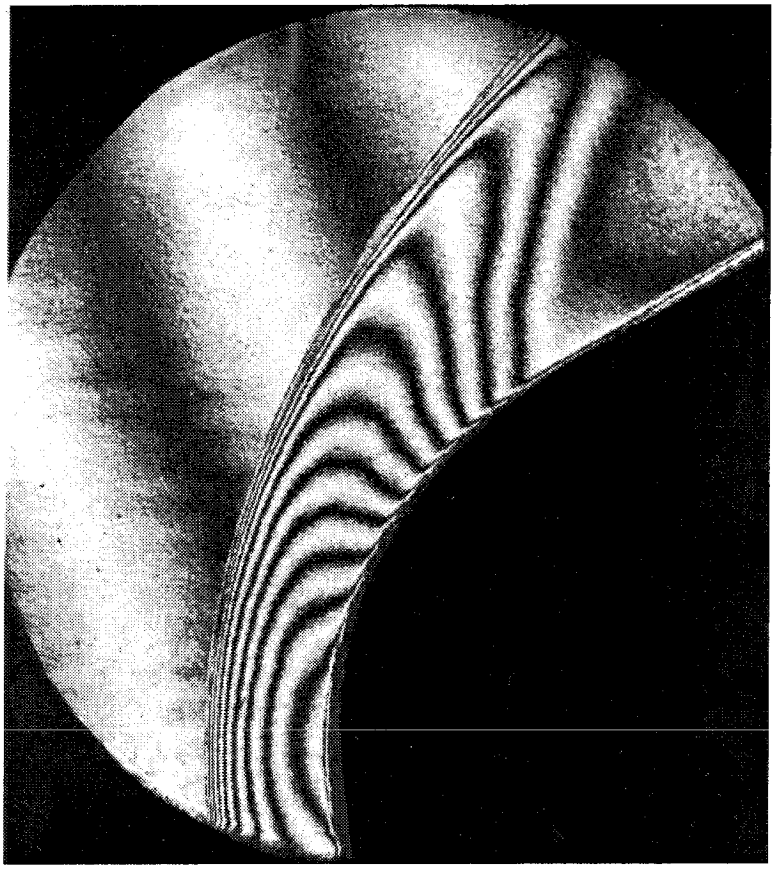

Figure 3.5. Interferogram of the stagnation region of the flow over the wedge. Flow is left to right. The flow conditions correspond to Condition 1 in Table 3.1, with a stagnation enthalpy of 10.4 MJ/kg.

limited by the free-stream dissociation level. The amount of dissociation present in the free-stream flow is a function of nozzle-flow freezing: the recombination reaction is frozen in the nozzle flow as the density falls in the expansion. This causes the density ratio across an equilibrium normal shock to be limited to approximately 12. One way to obtain a density ratio higher than that is to fire a projectile through a suitable gas at rest. For example, at a speed of 2500 m/s in a gas of small $\gamma - 1$ such as propane (where a perfect gas approximation of that condition gives $\gamma - 1 \approx 0.06$), the density ratio would be well over 20.

It was therefore decided to use a modification to T5 that had been made initially by Bélanger *et al.* [1995], and later improved by Kaneshige [1999], to shoot a projectile into a polyatomic gas. It is far simpler to make the projectile axisymmetric than

plane, for obvious reasons, and the simplest possible shape, a sphere, was chosen.

In the following, a description of the Bélanger/Kaneshige modification of T5 is presented. The modification is referred to as the T5 Light Gas Gun.

3.4.1 Description of the T5 Light Gas Gun

Fundamentally, the modification consists of using the T5 shock tube reservoir as a source of gas to propel a projectile through the conventional T5 test section, dump tank, and into a new test section mounted on the back end of the dump tank and into which the test gas is pumped. A projectile following this path travels a distance of approximately 4 m, after being accelerated by a launch tube 3.09 m long. The launch tube itself is mounted on a threaded nozzle insert which fits on the upstream part of the T5 contoured nozzle. A standard T5 contoured throat fits on the upstream part of this insert, with a thin mylar diaphragm sandwiched between the two sections to maintain vacuum in the launch tube (and the T5 dump tank) after the shock tube has been filled. The projectile is loaded by placing it between the throat and the mylar diaphragm. The launch tube itself is supported on a table mounted on the rails of the T5 test section. This table allows the precise alignment of the tube within the test section via an xy-translator, as well as an adjustment for the tube elevation.

The propellant for the projectile is the T5 shock tube test gas, compressed by the reflected shock in the nozzle reservoir. By using a gas with a low atomic weight (*e.g.*, helium), a high speed of sound is obtained in the propellant, which maintains high pressure behind the projectile for the length of its trajectory through the launch tube. This is the fundamental principle of operation of multiple-stage light-gas guns, first developed by Crozier and Hume [1957] and described in detail in Canning *et al.* [1970].

The free end of the launch tube protrudes approximately 1 m from the table support, inside the test section. A pressure transducer is mounted on the end of the launch tube, providing timing data for the projectile trajectory. Further modifications were required at the back end of the dump tank to accommodate the new test

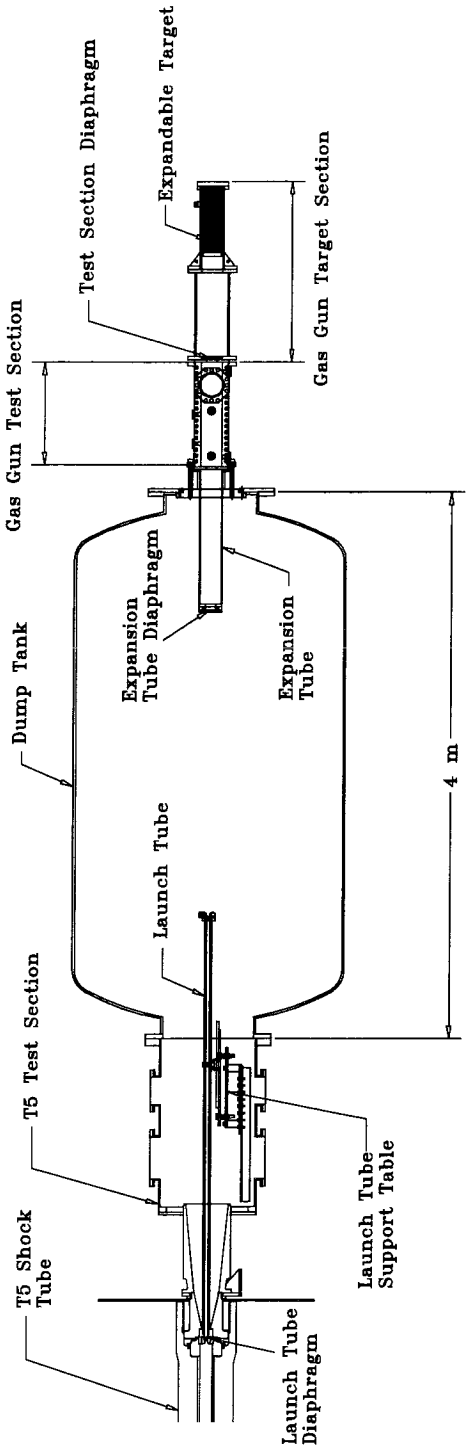

Figure 3.6. Side view of T5 Light Gas Gun assembly, and nomenclature. The launch tube is evacuated along with the dump tank prior to a shot. The test section and the extension tube are both filled with test gas. The target section is under vacuum during tests.

section.

The layout and nomenclature of the T5 Light Gas Gun, as used in this series of experiments, is shown in Figure 3.6. This configuration is nearly identical to that of shots 1839 and 1840 performed by Kaneshige [1999] for experiments on gas detonations using projectiles. Some minor modifications were made at the upstream end of the extension tube to improve the reliability of the timing signals used to determine the projectile speed. These are mentioned in Section 3.4.2.

T5 Light Gas Gun test section assembly

The test section used in the T5 Light Gas Gun experiment consists of three different zones:

1. A circular extension tube 15.24 cm (6 in) in diameter, used for the settling of the flow around the projectile.

2. A rectangular 15.24 cm $\times$ 15.24 cm (6 in x 6 in) instrumented test section with window ports for optical diagnostics.

3. A target section whose purpose is to capture the projectile without damaging any part of the facility.

The photographs in Figure 3.7 illustrate this assembly. While the extension tube, at 1.016 m long, is arguably redundant in the present experiment (settling time is not an issue in non-detonating gases), it nonetheless played an important role by supporting a timing wire used to record the time of entry of the projectile into the tube (discussed in the following section) and was therefore kept for this experiment.

The main test section housed three pressure transducers, three photodetectors and laser diodes, and a 16.61 cm (6.5 in) diameter window port used to photographically record the flow over the projectile.

Attached to the main test section is a separate target section. This circular target section houses a disposable plug, approximately 45 cm long and 10 cm in diameter,

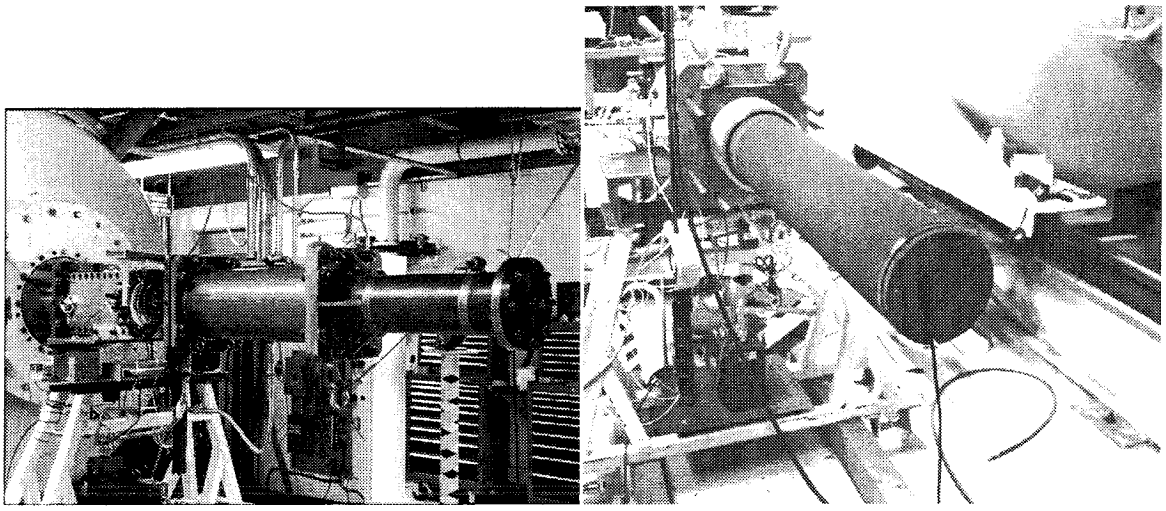

(a) (b)

Figure 3.7. Photograph of T5 Gas Gun assembly. In (a), the setup is in normal firing position. The extension tube is inside the dump tank and not visible; (b) shows the extension tube (with break wire assembly) after it has been removed from the dump tank.

which is made up of a series of honeycombed metal blocks, interspaced with heavy-gage sheet metal. This insert is not meant to be reusable and is in fact destroyed during each shot. Its purpose is to absorb and dissipate the energy of the projectile while stopping it. The target section is removed, cleaned, and repacked after each shot. It is initially under vacuum and isolated from the main test section by a mylar diaphragm[3].

3.4.2 T5 Light Gas Gun diagnostics

Flow visualization

The flow over the projectile is recorded, using standard shadowgraphy, as it passes in the field of view of the test section windows. In order to do this, a light source is synchronized to fire a short-duration beam through the Light Gas Gun test section

[3]The evacuation of the target section was found by Kaneshige [1999] to greatly reduce the amount of target debris that makes its way back into the test section after shots performed in detonating gases, and thus to minimize the required cleanup and the possibility of damage to the instruments and the windows. This evacuation is not strictly required for the present experiment. However, this procedure was also found to work well in the current experiments (with non-detonating gases), so it was not modified.

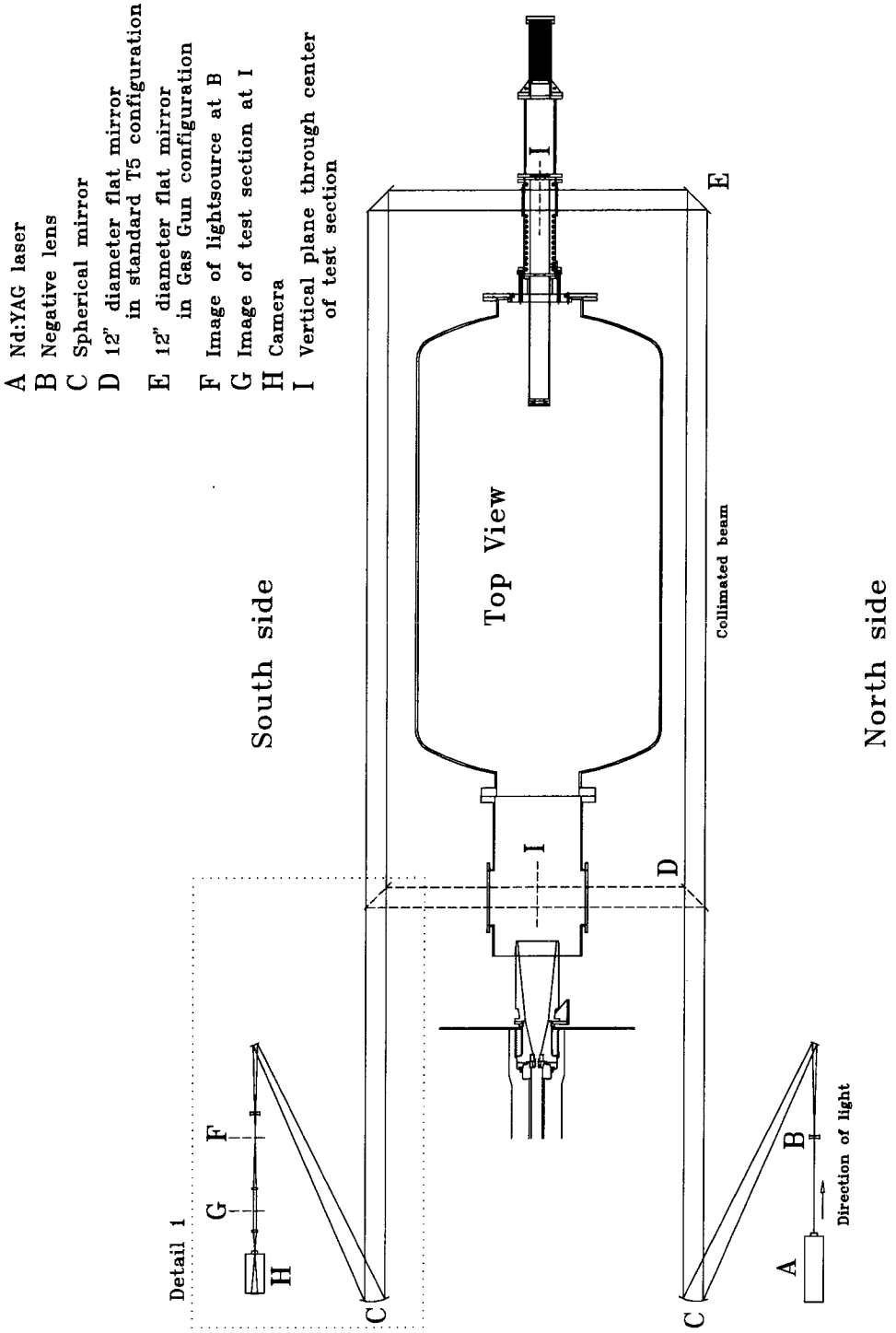

Figure 3.8. The T5 shadowgraph setup, both for standard T5 operation and for the T5 Light Gas Gun test section. The translation of the flat mirrors ('D') more than doubles the path that the light must take before reaching the film plate. The optical components themselves are not to scale, and their layout, from the laser to mirror 'C' and in Detail 1, is for schematic purposes only.

and onto an exposed film plate, in a manner similar to the standard T5 configuration. The light source consists of a Spectra Physics GCR-150-10 Nd:YAG which produces 532 nm laser pulses. The shadowgraph system used for the standard T5 setup needed to be slightly modified for the gun experiment, however, because of the fact that the new test section is located approximately 5.5 m further back from the collimating spherical mirror, behind the dump tank. Basically, the change consists of translating the two flat 30.5 cm (12 in) mirrors, used to redirect the expanded, collimated laser light through the test section, and back onto the camera. Unfortunately, this creates a significantly longer optical arm for the light to travel after the test section, before reaching the camera, and caused some problems in the shadowgraph system which will be discussed in Chapter 5. Figure 3.8 illustrates the optical setup used for both the standard T5 test section and for the T5 Light Gas Gun test section. Figure 3.9 is Detail 1 of that figure.

Projectile timing

In order to be able to draw quantitative conclusions from the shadowgraph, reasonable estimates of the projectile speed are required. For this purpose, a series of diode photodetectors and pressure transducers are used along the length of the test section. Additionally, a pressure transducer is available at the launch tube exit to record the time at which the projectile passed. Finally, in the configuration used in this experiment, a thin (38 AWG) 'trip' or 'break' wire was stretched across the opening of the tube. As the projectile entered the extension tube, the wire broke, resulting in a voltage change on the recorded trace (see voltage divider circuit in Figure 3.10).

This and other timing devices used at this station in previous experiments were reported to produce spurious timing signals and were found to be unreliable. The sooty environment of the dump tank, in particular, was found to make photodetectors unreliable at this station. The original break wire idea was re-engineered several times during all the experiments done in the T5 Light Gas Gun. The last changes, consisting mostly of improving the electrical insulation of the wire circuitry and better protecting it from possible damage from fragments and other debris, were

implemented by Kaneshige and the present author and performed well during this series of experiments.

The layout of the timing instruments is shown in Figure 3.11, and shows the distance between the stations. The pressure transducers, labeled P1 to P3 (in the direction of projectile travel), consisted of piezoelectric crystal devices manufactured by PCB Piezotronics, model 113A24 and 113A26. They have a natural frequency of 500 kHz and a rise time of 1 μs. The photodetectors (labeled L1 to L3) were either manufactured in house (L1 and L2) or purchased (L3), and were aligned along the line-of-sight of diode lasers with wavelengths varying between 650 nm and 680 nm. Interference filters were used in front of the photodetectors L1 and L2 to limit the bandwidth of the light transmitted to the photodetectors, because the luminosity in the bow region of the shock may produce errors in the detected signal. In the case of L3, a commercial unit (Thorlab Det2-SI) with a reported rise time of 1 ns was used to detect the passage of the projectile through the test section window ports. This timing station is the most crucial, as it is used to send the signal to Q-switch the laser and record the shadowgraph (see next section). Since the shadowgraph system

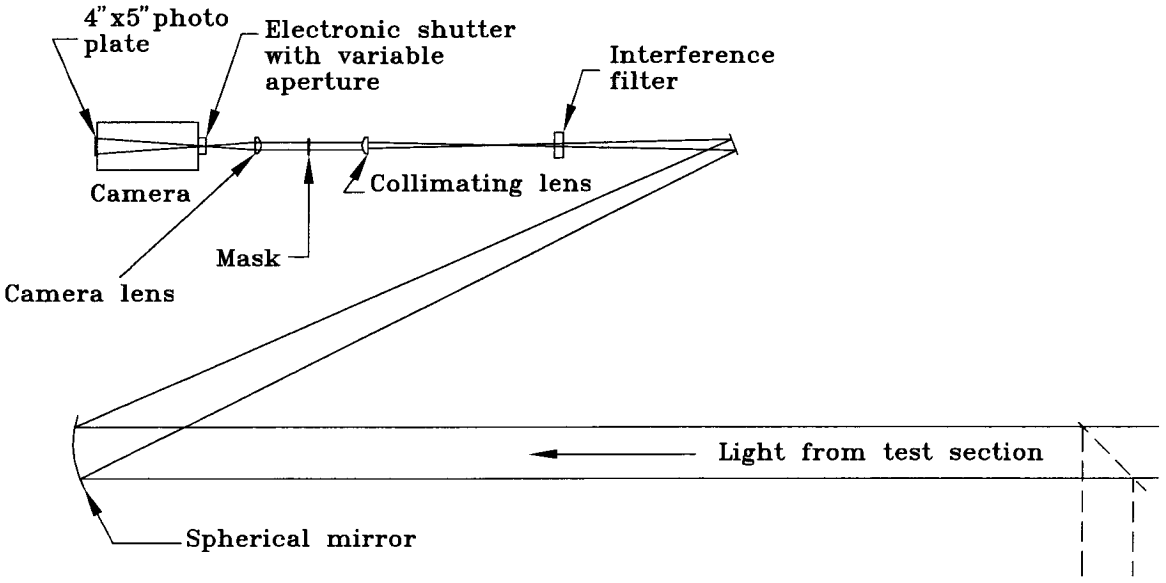

Figure 3.9. Schematic details of shadowgraph setup, camera side. The optical components are not to scale. Since the optics table is not in the same horizontal plane as the center of the test section windows, the light is actually folded vertically between the spherical mirror and the interference filter in the actual setup.

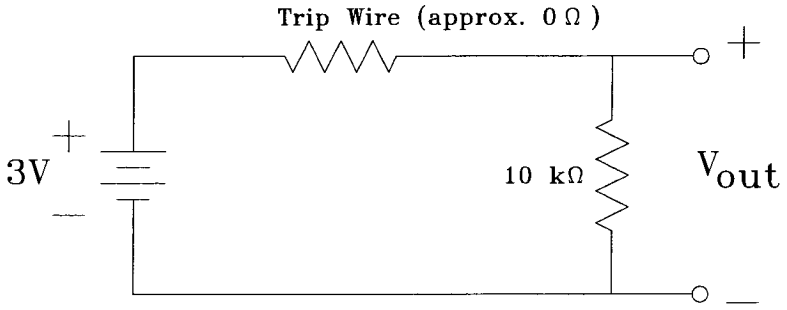

Figure 3.10. Break wire circuit. V_{out} goes to the T5 DAS and a storage oscilloscope.

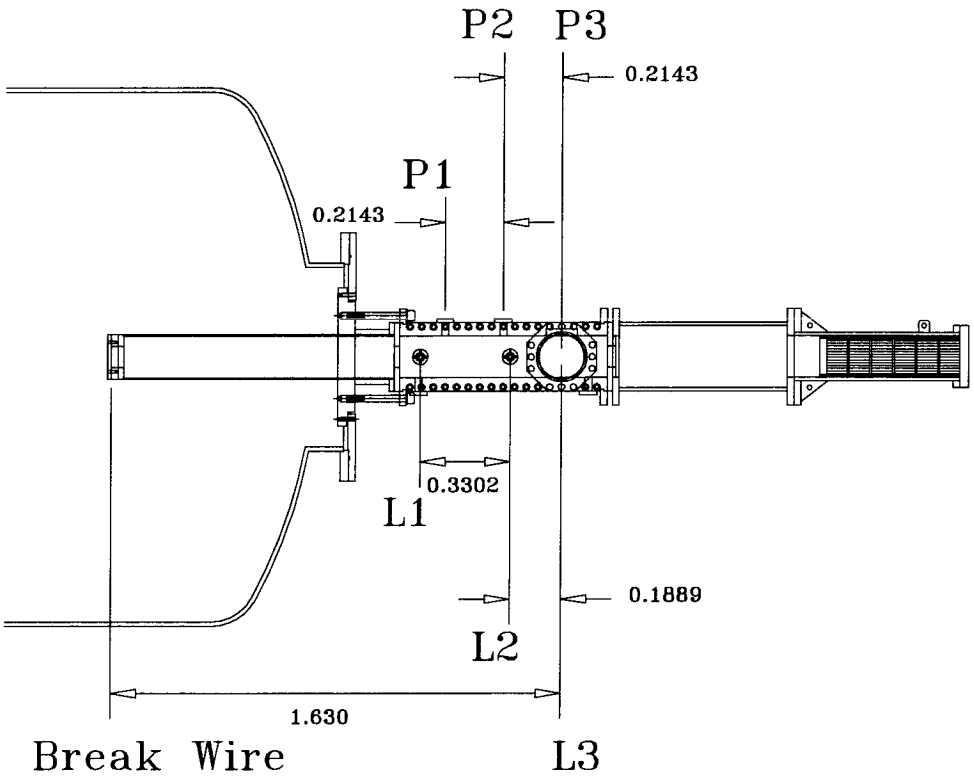

Figure 3.11. T5 Light Gas Gun timing instruments layout. Distances shown are in meters. L1, L2 and L3 are photodetectors; P1, P2 and P3 are pressure transducers.

already uses the whole field of view of the window ports, this means that the diode laser and L3 may not be aligned normal to the projectile trajectory, and so must cross the test section obliquely. This setup makes determining the exact position at which L3 is triggered difficult to measure. The position of the projectile in the test section windows, however, can be accurately measured in the shadowgraph; this datum, along with the Q-switch timing signal, is used for timing measurements, instead of L3.

Timing issues related to high-speed photographic system

It has been mentioned that the light source used for the shadowgraph system consists of a single pulse from a Nd:YAG laser. The length of this pulse and the intensity of the light determine the film exposure. To keep these parameters relatively constant, the laser flashes at a constant rate of about 10 Hz, so that the laser cavity and associated optics reach a quasi-thermal steady-state which is maintained until the experiment is over. An important parameter determining the intensity of the beam is the delay between flashlamp discharge and laser Q-switching. For the Spectra Physics laser used, this delay needs to be between 190 μs to 200 μs to obtain maximum laser power, with the half-power points occurring at approximately $\pm$ 30μs. During standard T5 operations, this delay is inconsequential: the laser may be set to automatically Q-switch 200 μs after flashlamp trigger without adversely affecting anything.

In the case of an experiment using projectiles traveling at many different speeds, however, the timing between flashlamp trigger and laser Q-switch becomes important and may need to be actively controlled. To illustrate this, consider the case of a projectile *expected* to travel at a speed of 3000 m/s through the test section. This projectile should cross a distance of 0.6 m in the 200 μs between flashlamp trigger and Q-switch. In order to capture the projectile in the center of the test section windows, therefore, the signal to fire the laser must be sent 0.6 m before the projectile arrives there. If, however, the *actual* speed of the projectile during the shot is 2700 m/s (10% less than expected), it will then travel a distance 6 cm less than anticipated. Since the window ports are only 16.5 cm wide, a system hardwired to capture the projectile in the center of the field of view by assuming a speed and keeping the flashlamp/Q-switch delay fixed would barely see the tip of the projectile in this example. Because of the large number of experimental parameters involved in this setup, projectile speed variations of 10% or more are possible from shot to shot. It is therefore clearly better to control the Q-switch signal directly, at a specific point within the test section windows (*i.e.*, by using L3), and to use earlier timing signals (*i.e.*, P_{exit} and the break wire) to calculate when to fire the flashlamp 200 μs before the projectile gets there.

A number of means exist to electronically compute the speed of the projectile from early triggers; in the T5 Light Gas Gun, this is performed using a modified form of a system devised by Chernyavskii *et al.* [1973]. The system is described in detail in Kaneshige [1999]. One problem with having the laser flashlamp and Q-switch signals controlled independently is that if, for any reason, a delay significantly different from 200 μs between the two signals occurs, then the film will be improperly exposed and the shadowgraph may not be usable[4].

Measuring speed from the timing signals

In order to measure the speed of the projectile, an average was taken from selected timing stations. The pressure transducers, for instance, were used strictly as backups since their frequency response is low and the distance between them is short, in comparison to the photodiodes. Sample signals from the pressure transducers and the photodiodes are shown in Figure 3.12 and Figure 3.13, respectively, and show that the resulting speeds deduced from these signals differ significantly.

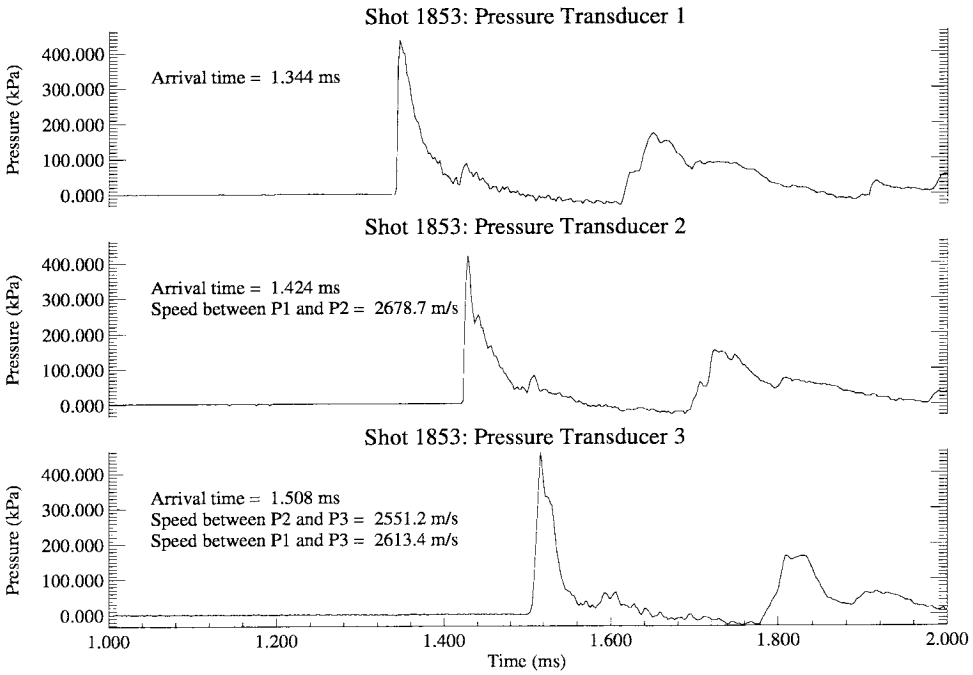

Figure 3.12. Sample timing trace from pressure transducers.

[4]In this series of experiments, such a problem accounted for the loss of one shot.

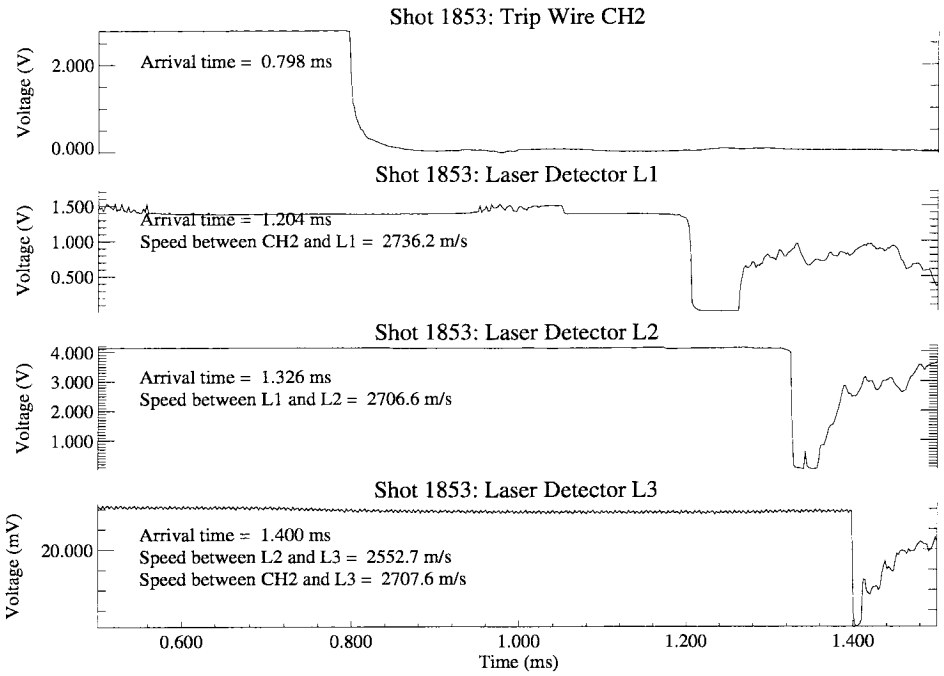

Figure 3.13. Sample timing trace from trip wire and diodes.

Two systems were used to record the timing signals: the T5 data acquisition system digitizers sampling at 500 kHz for all timing channels, and a Tektronix 640A storage oscilloscope with four channels sampling at 1 MHz each. The data acquisition system (DAS), although rated to operate at frequencies of up to 1 MHz, was found in many instances to operate unreliably at high frequency, and the confidence in the results obtained from it is consequently lower than in the results obtained with the oscilloscope.

The oscilloscope recorded timing signals from P_{exit}, the trip wire, and the laser Q-switch, as well as the laser flashlamp trigger for reasons discussed in the previous section. These timing signals were also recorded on the T5 DAS as backup; all other pressure and photodetector signals were only recorded on the T5 DAS.

Since P1, P2, P3, L1, L2, L3 and the break wire are all mounted directly onto the T5 Light Gas Gun test section assembly, their positions relative to one another may be measured accurately, up to the nearest millimeter. The launch tube pressure transducer P_{exit}, on the other hand, is subjected to the recoil of the shock tube during a shot, meaning that its position relative to the Light Gas Gun test section varies

by up to 10 cm during a shot. The uncertainty of its position with respect to the test section at the precise time of projectile launch is estimated to be of the order of 1 cm. This station was not used in the average speed calculation, although it may be argued that the uncertainty in the relative position of its timing signal and the comparatively slow response of the pressure transducer is more than offset by the long averaging length between P_{exit} and L3.

The estimated projectile speeds presented here were obtained by taking the following arithmetic mean, when the signals were available:

$$U_{proj} = \frac{[U_{L1-L2} + U_{L2-L3} + U_{L1-L3} + U_{BW-L3}]_{\text{DAS}} + 4 \times [U_{BW-Q}]_{\text{scope}}}{8}, \qquad (3.2)$$

where L refers to a diode station, BW refers to the break wire station, and Q refers to the projectile position at time of laser Q-switch. The speed found by the scope between the break wire and the Q-switch is multiplied by four to give it a weight equal to all the speeds found using DAS signals. The (systematic) standard deviation, σ, is computed on the same set of data, in the usual way

$$\sigma = \sqrt{\frac{n\Sigma x^2 - (\Sigma x)^2}{n(n-1)}}, \qquad (3.3)$$

where x refers to the speeds on the right hand side of Equation (3.2), and n is the number of signals used, up to eight in this case. The data are included in Appendix B.

3.4.3 Test conditions for the experiment

The aim of the T5 Light Gas Gun experiments was to observe flows at the highest possible density ratios and to determine if a shear layer instability developed to an extent where it affected the shape of the shock. In order to do this, two parameters could be varied

1. the speed of the projectile, and

2. the ratio of specific heats of the gas around it.

Two gases were chosen to provide varying ratios of specific heats: carbon dioxide and propane.

The reported projectile speeds for which the T5 Light Gas Gun had been used prior to this experiment ranged from approximately 2100 m/s to 2500 m/s, based on a single T5 running condition. It was important, for the purposes of this experiment, to significantly increase the range of speeds from (approximately) 1000 m/s to 3000 m/s. For this reason, additional conditions were designed and made use of two different T5 test gases: helium and nitrogen. Given T5 reservoir conditions, the speed of the projectile can be estimated using a method of characteristics program written and documented by Kaneshige [1999] for this purpose. The program was found to overestimate the muzzle speed of the projectile by approximately 15% because it does not account for various losses in the projectile trajectory through the launch tube, but it provided the best estimates of the speed for untested conditions and was used very successfully here.

Limitations of the experiment

In theory, progressively higher projectile speeds are possible, up to the limits of the T5 reservoir pressure (assuming constant projectile weight). But a practical limitation to the speeds achievable is the material strength of the projectiles. The original projectiles selected for the Light Gas Gun (polished nylon spheres 2.54 cm in diameter) were routinely damaged by the high acceleration and the friction with the launch tube wall.

It became apparent that the main running condition used by Bélanger and Kaneshige created a load very close to the impact strength of this material; in many shots, the projectile was found to break into several pieces, which can be clearly seen in shadowgraphs. This damage did not have an important effect on their results, but it presented a potentially serious problem here. A fragmented projectile produces a shock, which may differ greatly from that produced by a spherical one, and thus

Table 3.2. Impact strength of selected thermoplastics.

Material	Density	Impact strength (tensile)	Impact strength (Izod, notched)	Tensile strength
Nylon 101	1150 kg/m^3	4800-9600 J/m	30-50 J/m	60-80 MPa
Nylon (Nylatron NS)	1180 kg/m^3	6500 J/m	—	75 MPa
Acetal (Acetron GF)	1410 kg/m^3	2100-4800 J/m	65–120 J/m	60 MPa
Teflon-acetal (Delrin AF)	1540 kg/m^3	2700 J/m	—	50 MPa
Polyamide-imide (extruded Torlon)	1380 kg/m^3	—	150 J/m	20 MPa
Polycarbonate (extruded Lexan)	1200 kg/m^3	12000–16000 J/m	650–850 J/m	60–75 MPa

makes it difficult to separate the (hypothesized) effects of shear layer instability on the shock shape from those due to the projectile shape. Also, if the projectile starts to fragment at 2300 m/s, it is not possible to increase the speed significantly without completely disintegrating the projectile. Since the load applied to the projectile is impulsive in nature, the appropriate material property to consider is the impact strength. Of course, since the weight of the projectile needs to remain roughly constant in order to keep the pressure in the T5 reservoir the same, only materials with comparable densities were considered. These materials are listed in Table 3.2[5].

Polycarbonate materials were found to have an impact strength one order of magnitude higher than most other plastics, and so seemed better suited for high velocity tests. Unfortunately, whereas nylon spheres could be procured directly from vendors as highly polished spheres, polycarbonate spheres did not appear to be readily available in this form. Individual projectiles therefore had to be machined on a

[5]The values listed are taken from Port Plastics Inc.'s 'Properties of Polymers Engineering Thermoplastics', using ASTM test method D1822 for tensile impact strength, ASTM D256 for Izod strength (1/8 in specimen, notched), and ASTM D638 for tensile strength.

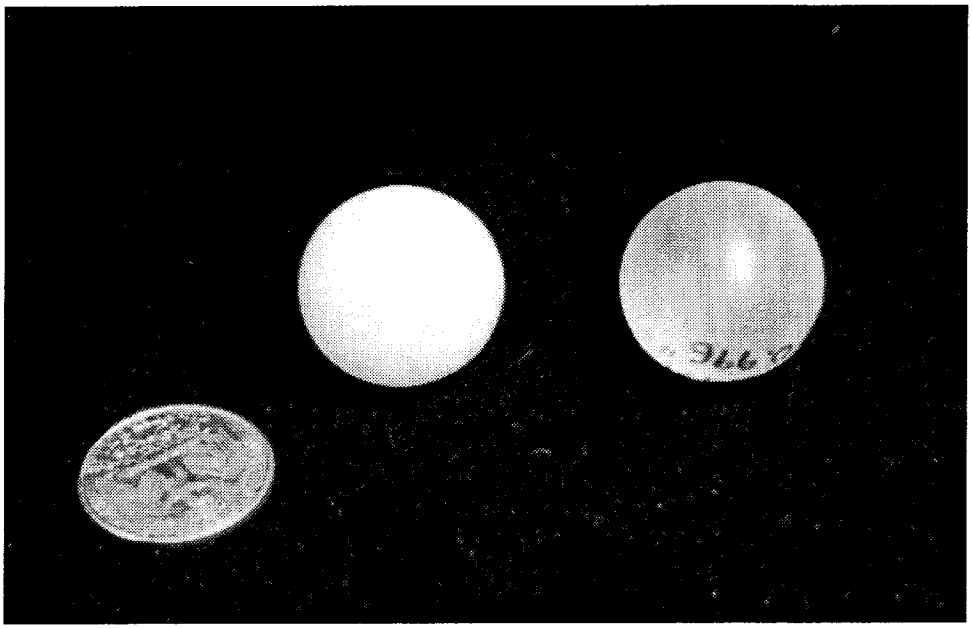

Figure 3.14. Nylon (left) and polycarbonate projectiles, similar to those used in the T5 Light Gas Gun experiment.

numerically-controlled lathe, from cylindrical polycarbonate rods. The spheres could only be machined down to a thin (5 mm) cylindrical support. This was required to hold the spheres in the lathe. This support was then cut flush with the surface of the projectile, leaving a flat on the sphere. During experiments, this flat area was oriented back to the flow when the projectile was inserted in the launch tube. It had no apparent effect on the results obtained. The manufacturing process necessarily affected the finish of the projectiles, which then exhibited small marks from the cutting tool. These differences in the surface roughness did not affect the flow around the projectile, but will be discussed further in Chapter 5. A photograph of spheres similar to those used in the experiment is shown in Figure 3.14. Thus, using polycarbonate projectiles provided a simple way to increase the range of operation of the T5 Light Gas Gun, and eliminated the problem of fragmentation. With these projectiles, speeds in excess of Mach 10 in propane were possible, which was adequate for our purposes.

This page is intentionally blank.

Chapter 4 Sodium Wire Streakline Visualization

4.1 Streakline visualization in scientific studies

Experimental studies of flow stability have benefited greatly from the ability to visualize the path taken by particles emanating from a common point (streaklines). The smoke-wire in low speed flows is a classical tool for obtaining profound information about the flow structure. Within the current project a development effort was undertaken to produce such a tool for short duration hypervelocity flows.

The idea of injecting smoke into a fluid for the purpose of flow visualization appears in the scientific literature as early as the nineteenth century (see, *e.g.*, Mach [1896]). In the traditional setup, the smoke lines are generated by a small pipe which injects smoke in front of a test model in a wind tunnel. Provided that the wind tunnel flow has sufficiently low turbulence, this method can be used even at supersonic speeds (Goddard *et al.* [1959]). In stability studies in particular, the smoke-wire has proved to be a valuable research tool and is still being used in qualitative and quantitative studies (*e.g.*, Fric and Roshko [1994]). A review of the literature, however, does not reveal any successful implementation of this technique, or a similar one, in the highly transient environment of shock tunnel-produced hypervelocity flows that would allow the visualization of streaklines and that could be used for the specific purpose of studying the shock-generated vorticity layer.

4.2 Implementing streakline visualization in hypervelocity flows

Visualization using smoke is not realizable at the flow conditions used in T5. On the other hand, Germain [1994] has been successful in applying the atomic sodium seeding method of Blendstrup *et al.* [1979] to visualize boundary layer flows in T5. This technique was the starting point for the development of streakline visualization for T5.

The new technique combines this visualization method with the smoke-wire idea. We chose to call it 'Sodium Wire Streakline Visualization' (SWSV). It uses the hot gas flow of the shock tunnel to produce the traces by ablation from a wire. By tuning a narrow bandwidth light source to the absorption frequency of the metal, streaks of this metal, even at concentrations in the parts-per-million range in the test gas, may be visualized. Furthermore, by adjusting the frequency of the laser around the absorption peak, both the absorptive and high refractive properties of that part of the spectrum can be used to produce different flow visualization effects. Since the available tunable light source in T5 is a dye laser operating near the 590 nm frequency, sodium was chosen as the seeding metal to generate the streaks, because its spectrum has a strong absorption doublet near this frequency. Although the remaining discussion will assume that sodium is used as the seeding material, the technique itself and the results obtained are equally applicable using other seeding materials and light sources.

The seeding is made relatively safe and simple by the high temperatures of hypervelocity flows, as it enables sodium to be introduced in the form of sodium chloride, deposited at discrete source points on a steel wire stretched across the flow. The hot gas causes significant dissociation of the NaCl and seeds the test gas continuously with atomic sodium emanating from the wire (at 7000 K and 1 atmosphere, 99% of NaCl is dissociated, at equilibrium).

The technique presented here is based on two well-known features of spectral lines, specifically applied to sodium:

- The atomic spectrum of sodium includes a high absorption/emission doublet at the D-line (D_1 at 589.593 nm and D_2 at 588.996 nm).

- The refractivity ($\kappa - 1$, where κ is the index of refraction) of sodium gas near this line can be several orders of magnitude higher than that of air.

Each of these features was used to try and produce a flow visualization method on its own. These studies are explained in the following sections.

4.2.1 Absorption

The level of light absorption that takes place within a streak depends essentially on the value of the absorption coefficient at the wavelength of the light source, provided that a minimum amount of sodium is present. The effect of the sodium seeding on the flow itself is negligible because of the low concentration required; highly diluted proportions, on the order of $1{:}10^3$ to $1{:}10^4$ were found by Blendstrup *et al.* [1979] to be sufficient for spectroscopy experiments using sodium. The absorption spectrum itself, however, is subject to significant variations based on the flow conditions. Spectral line broadening mechanisms, which are responsible for these changes in absorption fall broadly into four categories:

- Natural broadening, which occurs as a consequence of the limited lifetime of the excited energy states,

- Doppler broadening, which is a consequence of the motion of the atoms of the emitting or absorbing gas,

- Lorentz or pressure broadening, which results from a shortening of the lifetime of the excited state of the atoms due to collisions between atoms (not necessarily of the same element), and

- Electric or magnetic field broadening.

Electric broadening occurs in media in which high levels of ionization take place, and is therefore not applicable here. Natural broadening effects are typically of second

order when compared to Doppler and Lorentz broadening and are also neglected. Thus, under the conditions normally prevalent in atomic spectroscopy, Doppler and Lorentz effects combine to give a line profile, known as the Voigt profile.

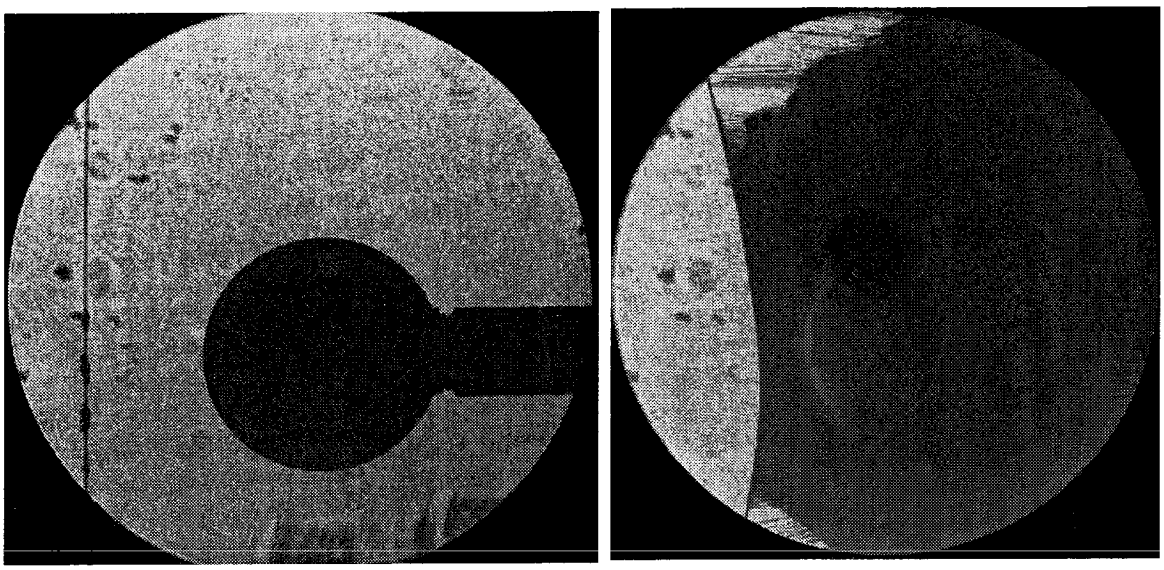

(a) (b)

Figure 4.1. Test of the Sodium Wire Streakline Visualization concept. Figure (a) shows the model, a 3 inch diameter sphere, with a wire seeded with sodium chloride at various locations. Figure (b) shows the effect of the hot gases on the NaCl, creating a sheet of sodium atoms which absorbs all the light downstream of the wire. The luminosity of the flow in the bow region of the sphere is visible. The drag on the wire is evident, and bends it in the direction of the flow. The marks in the field of view upstream of the wire and below the sphere in (a) are due to spots on the optical windows and are not part of the flow.

Since the typical free-stream pressure in the test section is small (of the order of 10 kPa and less) for all the conditions used in this experiment, while the free stream temperatures are high (ranging from 500 K to 3000 K), changes in spectral line width due to Doppler effects are much more significant than those due to Lorentz, or pressure, effects. Thus, for an order-of-magnitude absorption analysis, it is sufficient in this case to assume that the spectral distribution of sodium in the test flow is Gaussian, as if produced by Doppler effects alone.

At this point, however, the hypothesis of Sodium Wire Streakline Visualization, namely that sodium may be introduced in the flow produced by T5 and detected in the manner discussed, needs to be substantiated. In a preliminary experiment, a wire, seeded with sodium chloride, was stretched in front of a sphere. This setup was

placed in the T5 test section and subjected to a flow having a reservoir enthalpy of 11 MJ/kg. Some of the results of this validation study are shown in Figure 4.1 and illustrate some important features of the method. The fundamental premise of the method is clearly proved to be valid: NaCl dissociates continuously from the wire and seeds the flow downstream of it. Equally important are some of the potential difficulties to which results such as these pointed. For example, the flow is easily contaminated by excess sodium on the wire, thus contributing to the sheet-like effect blocking the light in this figure. Also, the results suggest that tuning the light source to a frequency slightly removed from that of peak absorption might minimize the susceptibility to contamination and improve the contrast between the regions where streaks are intended from those where they are not.

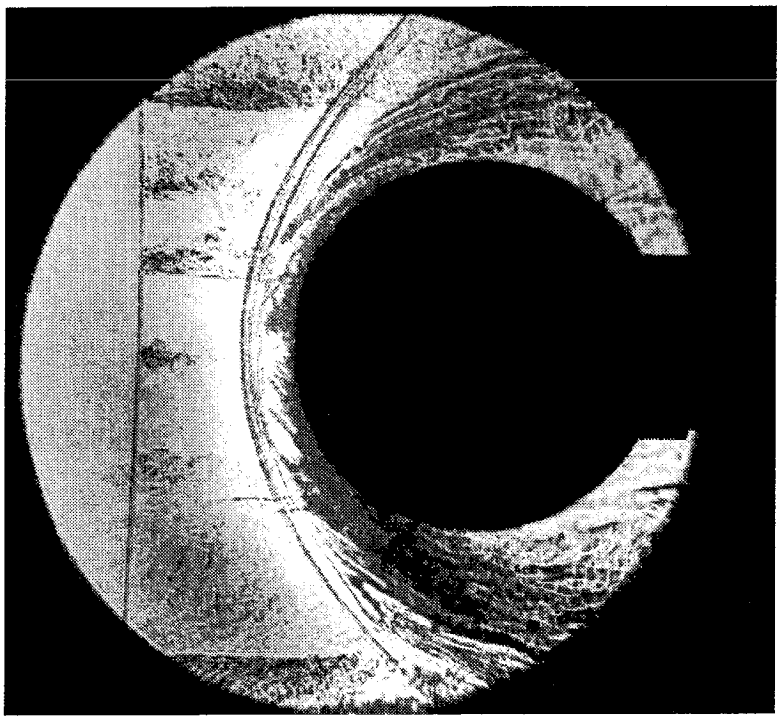

Figure 4.2. Streaklines through the shock produced by a cylinder. The laser is tuned sufficiently far from the center of the D-line that there is not excessive light absorption by the sodium in the test section. Note that the higher temperature of the flow downstream of the shock causes the sodium to absorb more light in that region than upstream of the shock.

Further tests were performed using a four-inch diameter cylinder at the same flow conditions as Figure 4.1. The wire was seeded at intervals of approximately 25 mm;

each site consisted of a salt crystal of roughly 3 mm in length and a fraction of a millimeter in thickness around the wire. The resulting flow is shown in Figure 4.2. While results such as this provided proof that streaklines can be traced using this technique and would provide a valuable tool in the study of the stability of the shear layer produced by the shock, further experiments showed that placing the wire downstream of the shock significantly improved the repeatability and reliability of the technique. In addition, placing the wire downstream of the shock made the seeding of specific areas of the flow easier.

4.2.2 Enhanced refractivity

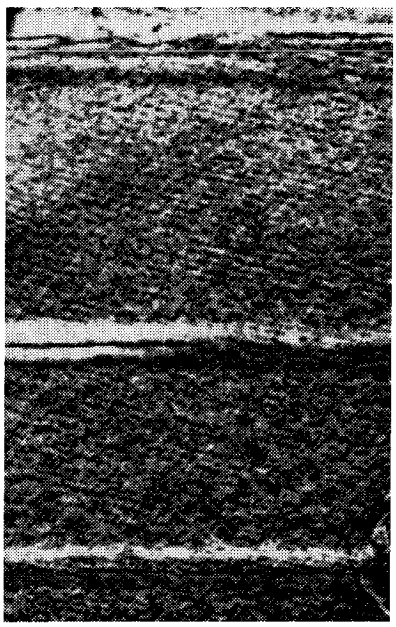

Figure 4.3. Three streaks, visualized by enhanced refractivity of sodium.

The absorption of light by sodium atoms is the predominant mode of flow visualization used to observe streakline, but the high refractivity of sodium near these resonant frequencies can also be used to produce different visualization effects. Techniques that rely on the gradients of the index of refraction (*e.g.*, differential interferometry, schlieren) may thus operate effectively with the light source tuned to a wavelength further away from the line center than what would be used in the absorption method, described previously. An example is shown in the visualization of three free-stream streaklines in a flow at $h_0 = 11\,\mathrm{MJ/kg}$ (Figure 4.3). The streaks are made visible by Wollaston prism differential interferometry, without noticeable absorption. The streaks in Figure 4.3 would not have appeared in absorption shadowgraphy at the wavelength of the light source used. The enhanced refractivity method is much less sensitive to the light source wavelength than absorption shadowgraphy, so that results may, in theory, be obtained over a larger range of laser frequency.

4.3 Apparatus, optical setup and the development of the flow tagging technique

The light source for this experiment consists of a 300 mJ/pulse, frequency-doubled Nd:YAG laser, which is used to pump a dye laser made by Cummings [1995], with wavelength adjustable in the 587–594 nm range. These lasers were used as light sources for both shadowgraphy and differential interferometry. The basic layout of the optical setup is similar to that shown in Figure 3.8; the dye laser is placed in line with the Nd:YAG laser, between points A and B. Mirror D is positioned so that the light passes through the T5 test section, with the light shown by dashed lines. The details of the setup used for differential interferometry are shown in Figure 4.4 and represent the new Detail 1 for this arrangement (on the camera side). A full explanation of the optical layout for Wollaston differential interferometry is presented in Merzkirch [1974].

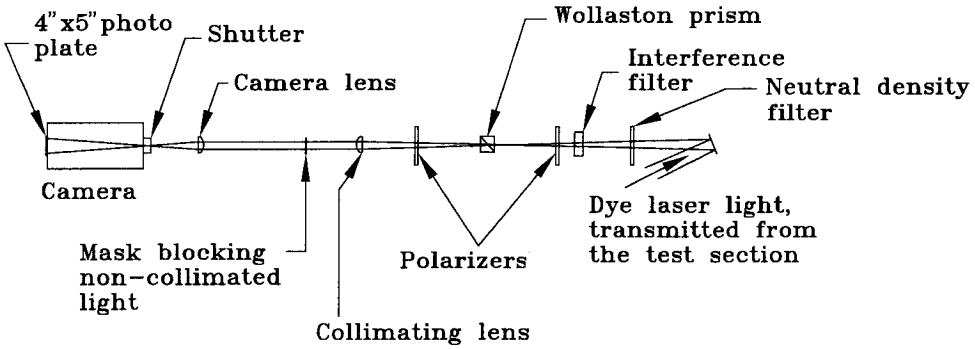

Figure 4.4. Detail 1 of Figure 3.8 for Smoke Wire Streakline Visualization optical setup with differential interferometry.

The light source frequency was tuned to the edge of one of the sodium absorption lines, as it appeared in a propane flame rich in sodium, at a temperature of approximately 1600 K and atmospheric pressure. At this condition, the D_2-line has a Doppler half-width of approximately 35 mÅ, whereas at an assumed flow temperature of 7000 K immediately downstream of the normal shock on the wire, the half-width is more than doubled to 74 mÅ. The half-width calculation is based on a formulation

by Thorne [1988], which gives it as

$$\Delta\lambda_D = 7.16 * 10^{-7}\lambda_0\sqrt{T/M}\,, \tag{4.1}$$

where T is the temperature in Kelvin, and M is the mass number of the atom. The Doppler absorption spectrum, assumed to be Gaussian, is given by

$$\kappa(\lambda) = \kappa_0 \exp\left\{-\left[\frac{(\lambda-\lambda_0)}{\Delta\lambda_D}2\sqrt{\ln 2}\right]^2\right\}\,. \tag{4.2}$$

Thus, though minimal absorption appears to be taking place through the propane flame, the absorption level would be perceptible, but not excessive, in typical flow conditions. The variation of both the refractive index and the absorption coefficient with wavelength in the line is fairly large and depends on the broadening of the line. Fine wavelength adjustments of the dye laser thus become necessary to obtain a given level of absorption and to avoid excessive absorption such as that shown in Figure 4.1.

Figure 4.5 shows the tuning of the laser by scattering its light onto a backwall, after passing through a propane flame rich in sodium. The level of absorption taking place is evident by observing the shadow of the flame on the backwall: with the laser frequency adjusted outside of the absorption spectrum, the light passes through the flame with little or no absorption, and no shadow (except for the apparatus) appears on the wall; as the frequency of the laser is adjusted within the spectrum, however, the width and contrast of the flame shadow may be used to infer the absorptivity of sodium at this frequency and temperature. The sensitivity of the dye laser to adjustment is such that approximately three revolutions of a micro dial linked to a diffraction grating controlling the dye laser frequency are required to span the absorption spectrum of one of the D-lines. This resolution was found to be satisfactory for the purposes of the experiment.

The fundamental flow tagging mechanism described so far is simple, but the development of a technique to insert the sodium in the flow at a *specific* location, in a reliable, repeatable way, proved to be more tedious than anticipated and was subject

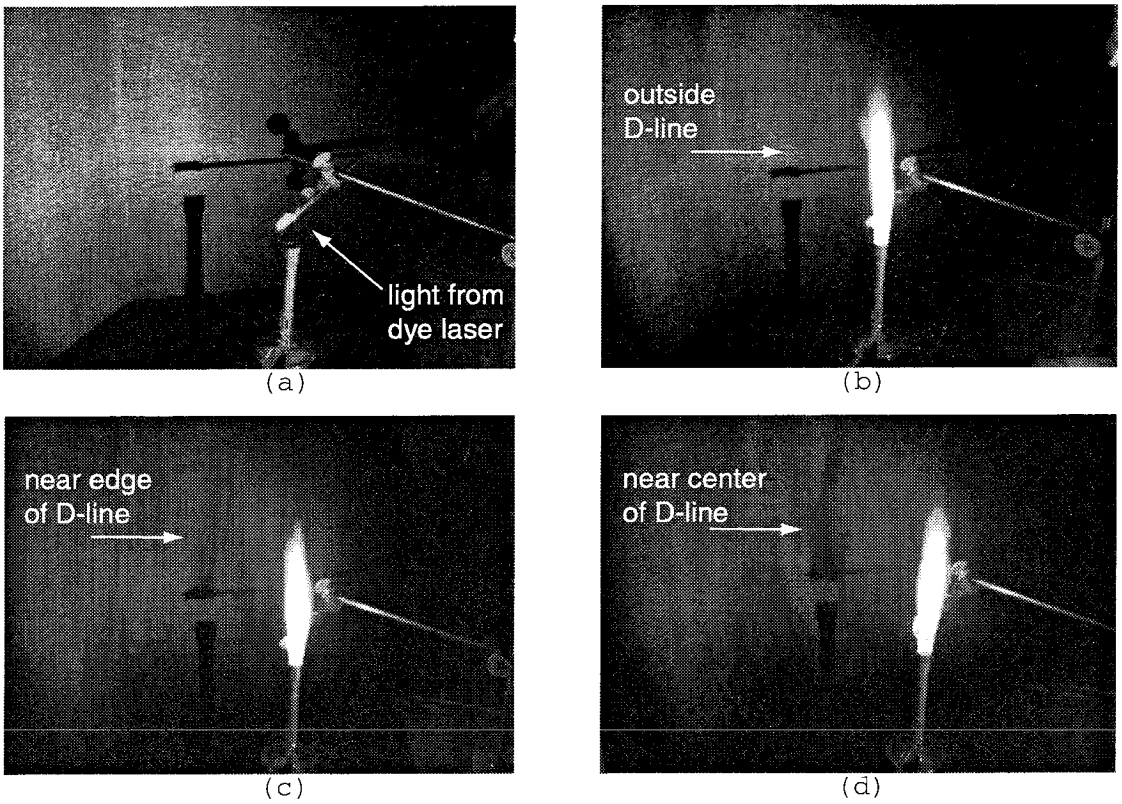

Figure 4.5. Adjusting the dye laser frequency using a propane flame saturated with sodium. Image (a) shows the setup, with scattered laser light (coming from the right) illuminating a propane burner and casting its shadow on a back board. Above the burner is a metal rod with crystallized NaCl. In the subsequent shots, the dye laser is tuned: (b) several mÅ from the sodium D-line; (c) near the edge of the D-line, and (d) near the center of the D-line.

to continuous changes throughout the course of this study. For instance, using sodium chloride as the source of sodium atoms introduced other problems which affected the reliability of the technique. Growing salt crystals by painting brine directly onto a wire stretched vertically (or nearly so) across a model proved to be a significant source of contamination of the wire: the liquid brine is prone to run along the wire, therefore seeding a large area of the flow with sodium. Contamination precluded the recycling of the wire for more than one shot. Even with the most careful handling, providing accurate seeding points without contaminating the wire was always challenging. In order to try and minimize this type of contamination, different substances were tested to replace brine as a 'filler' for NaCl: wax, grease and glue saturated with salt were tried but proved to be less reliable than brine, despite its other problems.

In order to minimize the chances of contaminating the wire with brine, salt crystals were grown on the wire as it was stretched horizontally above a test bench, outside of the test section. In this manner, crystals of arbitrary thickness could easily be grown by painting brine in multiple passes over the desired seeding source location. The wire, with (dry) NaCl crystals can then be mounted vertically over the model and adjusted so that the crystals are aligned with the desired locations within the shock layer. The additional handling involved with this, however, is not ideal, as the brittleness of the salt crystals sometimes causes them to shatter as the wire is mounted in the test section. Furthermore, even if the salt crystal does not break while the wire is being handled, it may be sufficiently weakened so that it breaks off from the wire in a single event, due to the pressure jump caused by the incoming flow during a shot. If this occurs early enough, the whole crystal is removed from the wire and no streak is visible on the shadowgraph; if it occurs sufficiently close to the time when the shadowgraph is recorded, parts of the salt crystal are still visible in the shadowgraph and give the impression of small streaks emanating from within the shock layer. This problem is illustrated in Figure 4.6.

4.3.1 Alternative sources of sodium

Despite several disadvantages, sodium was used in the form of salt crystals grown on wires for most of this experimental study. Different ways to attach sodium chloride to the wire were tested, in the hope of developing a method that would minimize the possibility of sodium contamination of the flow outside the streaklines, and create a source of sodium atoms that is not so brittle as to break off in the flow.

Late in this development process, a new seeding material was tried: pure sodium. Sodium metal in pure form, however, reacts violently with water (even with the water vapor present in air), so that it must be handled with care at all times, and stored in kerosene when not used. Even during the short period of time between attaching sodium lumps to the wire and evacuating the test section, the sodium has time to visibly react with water in air.

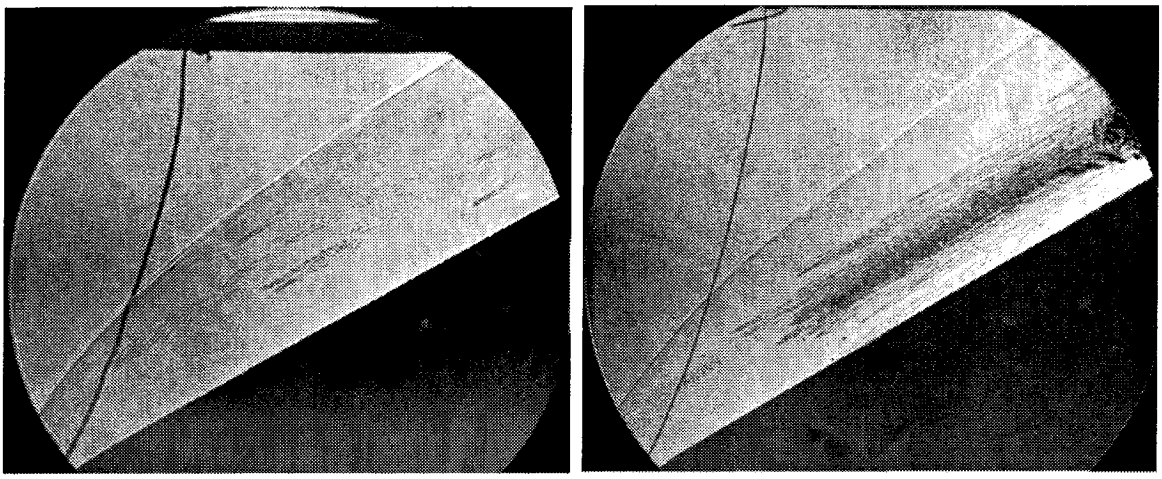

(a) (b)

Figure 4.6. Examples of the brittleness of the salt crystals causing flow tagging problems. Parts of the crystal, having broken off the wire, are still being convected by the flow. Since the crystal is heavier than the surrounding gas, it acts as a source of sodium atoms further downstream. In (a), hardly any of the crystal is left on the wire by the time the shadowgraph is taken, while in (b), it remained on the wire sufficiently long to provide useful information about the flow.

There were advantages, however, which made the consideration of this metal appealing for the purposes of flow tagging:

1. The paste-like nature of sodium allows clumps to be directly attached to the wire, *i.e.*, the sodium may be attached to the wire after it is mounted over the model in the test section, thus minimizing handling and reducing the risk of contamination.

2. Pure sodium eliminates the dissociation step previously required with NaCl. Hence, higher concentrations of sodium may be expected to tag the flow. Also, this may extend the range of applicability of this technique by reducing the lower limit of temperature where it works.

3. Sodium metal is not brittle. Randomly tagging the flow by breaking off the wire thus appears to be less likely[1].

[1]Still, sodium metal has very little strength when attached to a wire, so that the possibility of having it beak off during a shot is, in theory, not eliminated.

Pure sodium was used with success in the experiment, as shown in Figure 4.7. This figure shows two streaks generated at a reservoir condition of 10 MJ/kg. The streak closest to the body, barely visible in this picture, was made using the traditional salt crystal method. Above that streak, another streak was generated using sodium metal. This streak was placed in the region of high vorticity generation, and exhibits some instability towards the end of the picture. Results such as these will be used in following sections to discuss the primary instability mode of the shear layer produced by curved shocks. Unfortunately, while it is now clear that sodium metal is better

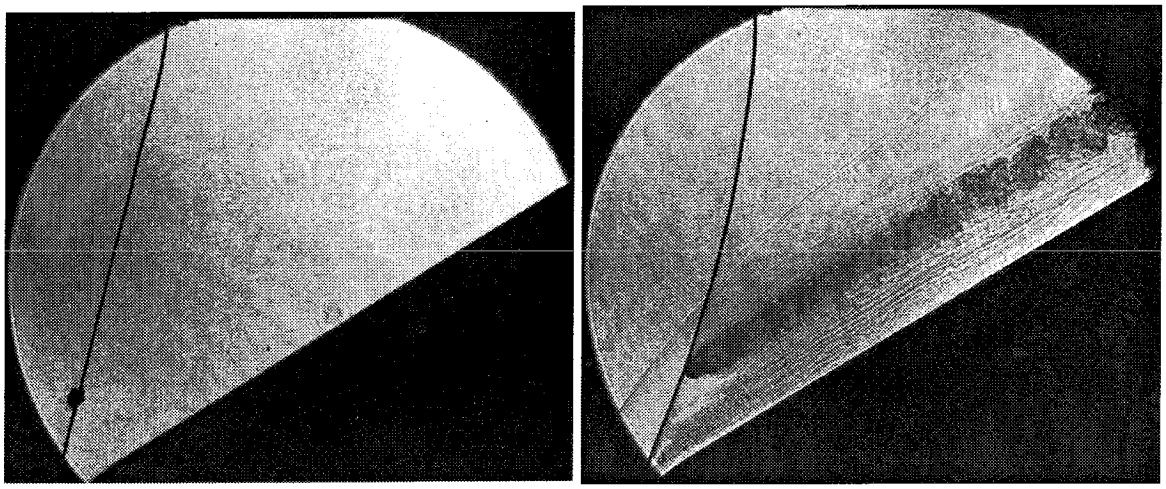

(a) (b)

Figure 4.7. Comparison of sodium lumps versus NaCl in tagging the flow. Figure (a) shows the wire setup before the shot. The sodium metal, pasted onto the wire, is clearly visible above the model. The salt crystal is to the left of the field of view. Figure (b) shows a shadowgraph of the flow over the model. The increased concentration of sodium along the streak generated by the metal lump is clearly evident, when compared to the streak produced by the NaCl (below).

suited for the purposes of flow visualization than NaCl, it was used for only a few shots towards the end of the study.

4.3.2 Limits in the range of applicability of Sodium Wire Streakline Visualization

While there are no clear upper limits to the maximum enthalpy at which this technique will work, the effectiveness of using sodium to visualize flows at low enthalpy is

limited. For these flows, the width of the D-line is substantially reduced, compared to higher enthalpy conditions, so that precise adjustments of the laser frequency become critical. Moreover, the concentration of sodium in the flow is also reduced by the lower temperatures, compounding the problem of detecting clear streaks in the flow. In the current series of experiments, it has not been possible to observe streaklines at the lower enthalpy condition (5 MJ/kg), probably as a result of these two factors. Perhaps with accurate spectrometers to adjust the laser frequency, the lower range of temperature may be extended down to the lower limit of detectability of sodium in the flow.

4.3.3 Line-of-sight integration

Two-dimensional images such as the ones obtained in the methods discussed here are projections of a three-dimensional flow. The images therefore represent the integrated effect along the line of sight. In the case of SWSV, however, the sodium streak being visualized is concentrated in a small region near the mid-plane of the model, in a zone where three-dimensionality is not an important issue. Therefore, the streak is confined to a narrow, nearly two-dimensional part of the flow. The region of integration in the line of sight is the width of the streak itself, which is small compared with the span of the model. SWSV may therefore also be used to study the three-dimensional nature of more complex flows by varying the spanwise location of the source, but such a study was not done in the present series of experiments.

4.4 The effect of the wire on SWSV results

A drawback of SWSV is that it does not permit the investigation of the flow in a non-intrusive manner. In a study focused on flow stability, it is important to be able to separate possible wire effects from the stability of the shear layer on its own.

In the following sections, two effects of the wire on the flow are discussed: the interactions with the shock produced by the model, and the effects of the wire wake on the flow.

4.4.1 Effect of the wire on the shock

In order to seed specific areas of the flow and improve the reliability of the technique, it was found that placing the wire downstream of the shock generated by the model, directly into the shock layer, produced the best results. This procedure means that at some point along its length, the wire pierces the shock generated by the model. Hence, the wire interacts with the shock in two ways: the shock generated by the

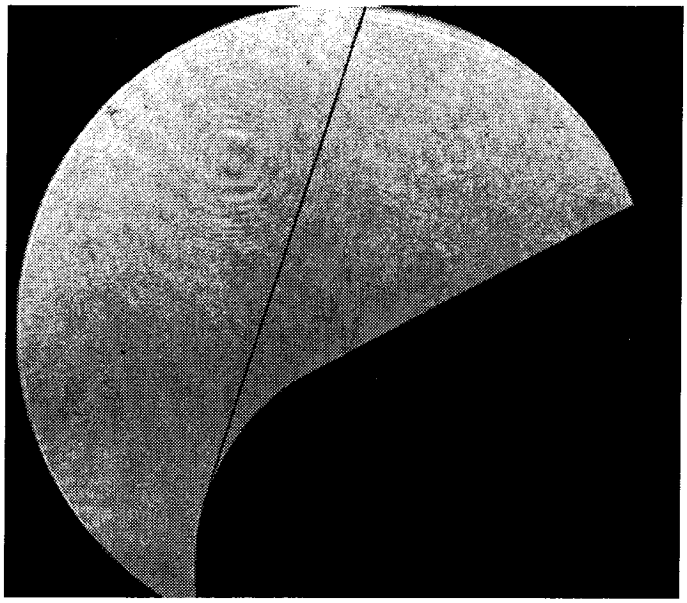

Figure 4.8. SWSV pre-shot setup, showing the angle between the wire and the model (here with the 6.35 cm radius leading edge). This angle is intentionally kept relatively small, in part to help in reducing the interaction between the wire and the shock.

wire interacts with the model shock, and the wake behind the wire disturbs the model

shock.

Shock-shock interaction

During a typical SWSV experiment, the wire is stretched from a region close to the model's leading edge at an angle of 30° to 45° with respect to the model surface, for a length of about 20 cm (a photograph of the typical setup is shown in Figure 4.8). The 1.9 cm radius leading edge was manufactured with a through-hole, approximately one nose radius downstream of the tip, for the purpose of locating the wire further downstream through the shear layer. This setup prevents the shock from the wire-holder (above the model) from interfering with that of the main body, and provides a relatively long span over which the wire can be seeded with salt crystals. It is therefore inevitable in this setup, however, that the wire intersects the plane of the shock from the model at some point along that span, but by keeping the angle between the wire and the model relatively small, this interaction occurs far from the region of high vorticity generation, and so has a minimal effect on the shear layer. Wherever this intersection occurs, the interaction between the two shocks may be expected to alter the flow somewhat. Although the shock produced by the wire is not resolved by the shadowgraphs, the localized disturbance produced on the shock generated by the model is visible, as shown in Figure 4.9.

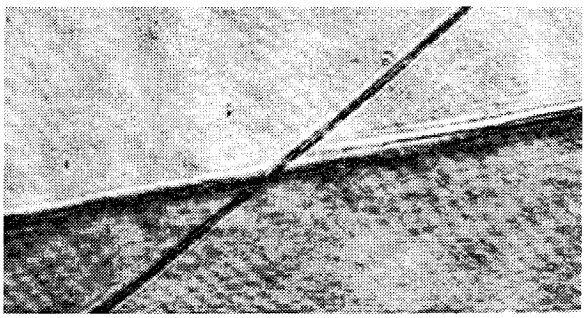

Figure 4.9. Wire shock interacting with the shock generated by the model.

The effect seen in Figure 4.9 is localized, and by keeping it far from the region of high vorticity generation, it is not believed to compromise the shear layer.

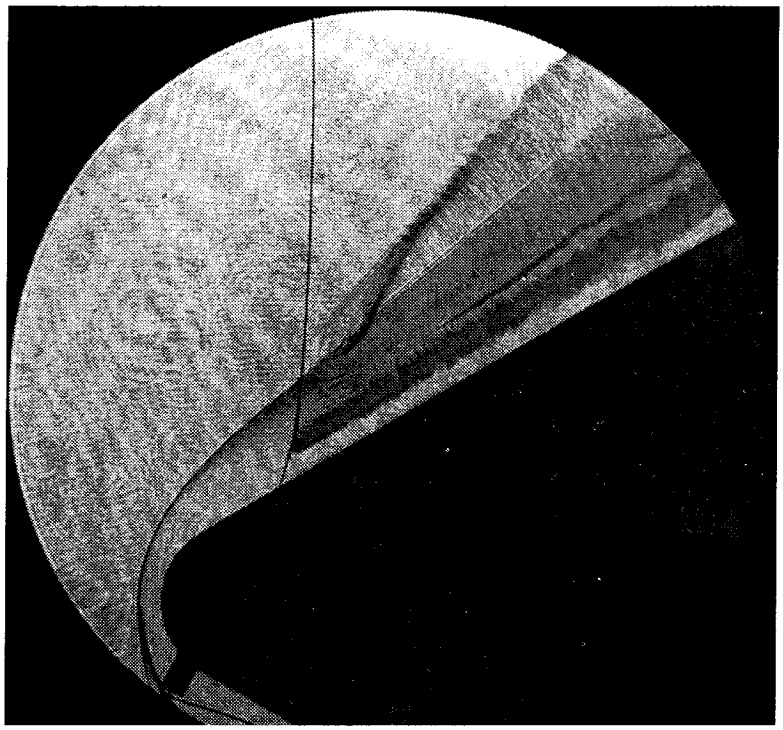

Figure 4.10. Entrainment of a streakline within the wire wake, above the plane of the shock.

Wake-shock interaction

In some cases, entrainment of sodium onto the wire wake in the direction along the wire was observed. This was particularly evident when streaks were produced in the vicinity of the intersection of the wire with the shock. By investigating this region with SWSV, the critical region appeared to be localized very near the intersection of the wire and the shock; no entrainment affecting the streak seemed to occur in the shear layer. When parts of the seeding point fall within a region of a few wire diameters around the point of intersection, the streak may be entrained into the wake of the wire, as shown in Figure 4.10.

In brief, beyond the immediate zone surrounding the intersection of the wire and the shock, there does not appear to be any effect on the streaklines due to either shock/shock interaction or the shock-wake interaction.

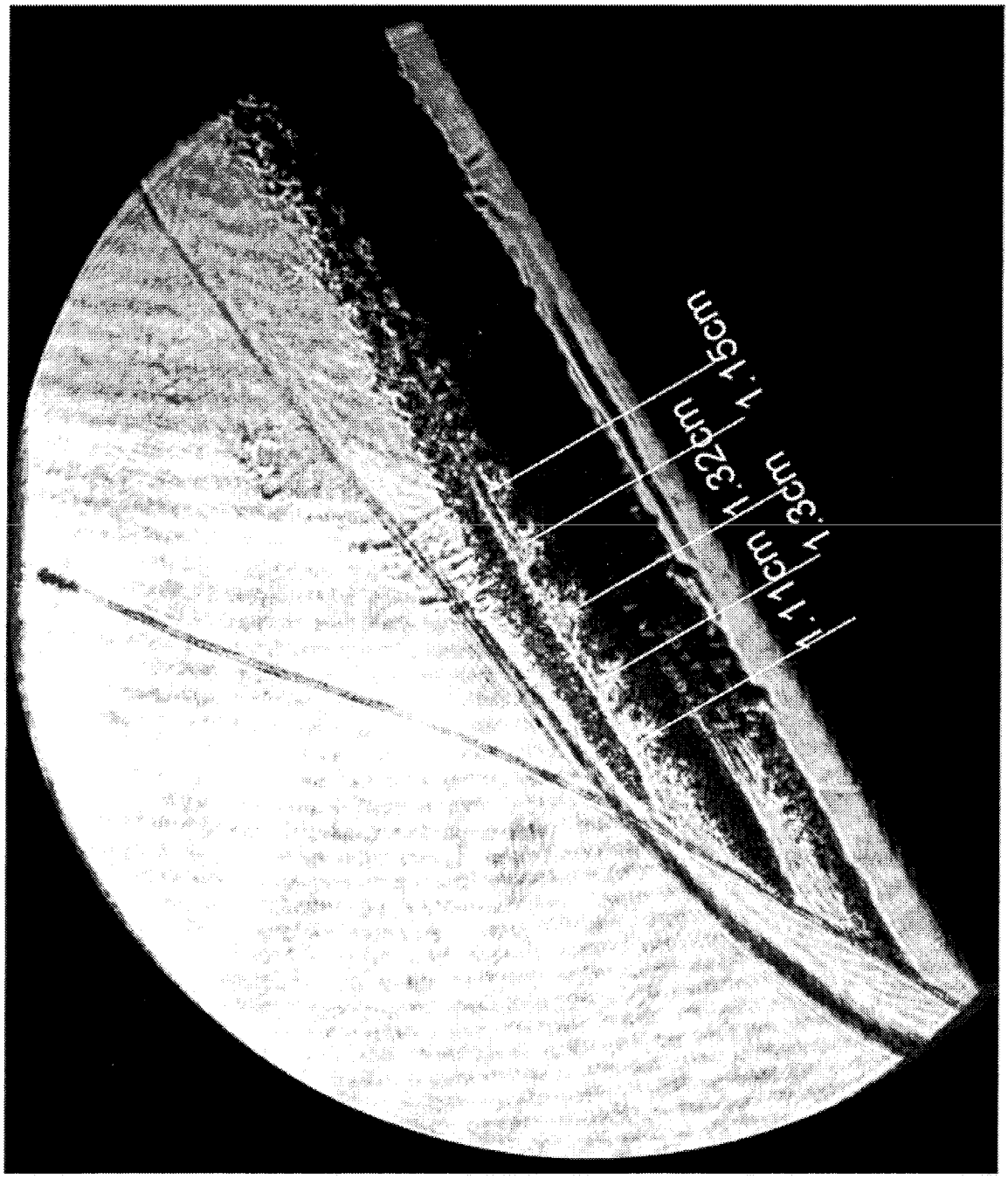

Figure 4.11. Streaklines through the shear layer.

4.4.2 Wire wake instabilities versus an instability in the shear layer

The effect of the wire on the flow is of course not limited to its intersection with the shock. Since the wire is essentially a cylinder in cross flow, it is conceivable that it, not the curved shock, may be responsible for any structures observed in a streakline. The geometry of the model and of the optics system being known, quantitative measurements can be made to verify whether any observed structures are shed by the wire or correspond to an instability in the shear layer. One of the clearest examples of the results of our investigation that may be used to discuss this situation is presented in Figure 4.11. This shadowgraph shows the flow over the wedge model with the 3.5 cm leading edge. A wire, 0.61 mm in diameter, is stretched through the shear layer and used for SWSV. The wire has three sodium source points, spaced at 2.5 cm intervals, spanning the shock layer from the body to the shock. The bottom streakline is aligned with a streamline near the stagnation point of the wedge; the center streakline is aligned approximately with the streamline that passes through the point of maximum vorticity generation (*i.e.*, the center of the shear layer); and the top streakline is very close to the oblique (nearly straight) part of the shock.

The middle streakline in Figure 4.11 strongly suggests that an instability has developed in the shear layer; the wavelength of that instability may easily be measured from the shadowgraph. The dimensions are shown in the figure. Contrary to a free shear layer, which tends to grow rapidly in a direction normal to the flow, the shear layer produced by the curved shock is bounded on one side by the body surface and on the other by the shock, thus limiting its spatial growth. Nevertheless, by the end of the shadowgraph, the three streaks have completely mixed together. Also, the bottom streak (closest to the body), which is not in a region of high shear in the flow, remains relatively undisturbed for most of its trajectory.

This shadowgraph thus appears to provide us with the prevalent wavelength of the instability that develops in the shear layer produced by a curved shock. But another possible source for the vortices observed is the wire wake. Its features are discussed

next.

The cylinder in cross flow

The test condition of Figure 4.11 corresponds to Condition 1 in Table 3.1. Using the actual T5 reservoir conditions recorded during the shot[2] as input to a non-equilibrium nozzle flow program NENZF (Lordi *et al.* [1966]), the flow conditions at the exit plane of the nozzle can be computed. This free stream flow is then used as input into Candler's code (see Chapter 2), which computes the steady-state flow over the blunt wedge and provides estimates for the flow conditions downstream of the shock near the region where the wire seeds the flow. These conditions are listed in Table 4.1.

Table 4.1. Local flow conditions at the source point of the three streaklines seen in Fig. 4.11.

Streakline	U	M	T	P	Re
top	2850 m/s	2.4	4400 K	108 kPa	1200
middle	2400 m/s	1.9	5160 K	107 kPa	800
bottom	1500 m/s	0.9	5900 K	182 kPa	630

The viscosity used for the Reynolds number calculation in this Table is computed using a formulation described by Blottner *et al.* [1971], which gives the dynamic viscosity of partially dissociated nitrogen in equilibrium as

$$\mu = 0.1 \exp[(0.268 \ln T + 0.31778) \ln T - 11.3155] \frac{\text{kg}}{\text{m} \cdot \text{s}}, \tag{4.3}$$

where T is in Kelvin.

The cylinder in cross flow is a problem that has received considerable attention over the last half-century (for a review, see, *e.g.*, Williamson [1996]). Such a flow is known to produce periodic oscillations in the wake of the cylinder over a large range of Reynolds numbers. The frequency of these oscillations is usually measured

[2]Required specifically are the reservoir pressure and the reservoir temperature. The former is measured directly in the lab, while the later may be computed from an equilibrium calculation across the reflected shock, performed here using a code written by McIntosh [1969].

in non-dimensional form, in terms of the Strouhal number given by

$$S = \frac{fd}{U_\infty}, \tag{4.4}$$

where S is the Strouhal number, f is the shedding frequency of the structures observed downstream of the cylinder and d is the cylinder diameter. The value of the Strouhal number for flows around cylinders has been verified by many independent studies to remain constant at around $S = 0.2$ for a large range of Reynolds numbers, from as low as $Re = 200$, all the way up to $Re = 10^7$ (White [1991]). Additional studies done on yawed cylinders (Van Atta [1968]), have shown that this result is also applicable to cylinders inclined with respect to the flow, if the Strouhal number is formed with the component of velocity normal to the cylinder (see Equation (4.5)). This procedure has been shown to be valid for yawing angle ranging from 0° (cylinder perpendicular to the flow) to about 80° beyond which the wake is described as 'chaotic' (Lewis [1993]).

Since the flow geometry and properties of Figure 4.11 have been identified, a wire wake analysis may be performed to determine if the wavelength observed can indeed be due to the wire. The component of velocity normal to the wire is used to calculate the Strouhal number. In this case therefore, we have

$$S = \frac{fd}{U_\perp}, \tag{4.5}$$

where $U_\perp = U \sin\phi$, and ϕ is the angle between the cylinder and the flow. From Figure 4.11, $\phi \approx 30°$. The shedding frequency for a cylinder is given by

$$f = \frac{U}{\lambda}, \tag{4.6}$$

where λ is the wavelength of the vortices. Substituting the values pertaining to the streakline of Figure 4.11 into Equation (4.5), we get $S \approx 0.08$, well below the expected value for vortices shed from a cylinder. Furthermore, we observe that the two streaks emanating from above and below the center streak (corresponding to the center of

the shear layer) do not exhibit the large structures present in the center streak. The variation in $U_\perp$ across the shear layer, responsible for variation in Reynolds number computed in Table 4.1, is not enough to vary that parameter outside the range for which the Strouhal number is constant. The top streakline is, however, clearly turbulent, perhaps as a results of this increased Reynolds number, though again no large scale structures are visible. Hence, this further supports the hypothesis that the structures observed in the center streak are due to the shear layer.

Finally, we note that the component of velocity perpendicular to the wire in all of these streaks is only marginally subsonic for the center streak and supersonic for the top streak. It is important to consider, therefore, what happens to the stability of the flow in the wake of a cylinder at Mach numbers greater than 1.

The cylinder in supersonic flow

Hot wire studies in the wake of cylinders in supersonic flows, performed in the sixties in the Graduate Aeronautical Laboratories of the California Institute of Technology, have looked specifically at this problem (Behrens [1966]). In these studies, the width of the outer wake behind the wire was measured, and the spectrum of frequencies of instability was determined. The main instability mode, for given wire diameters, was found to occur in the outer wake of the cylinder in hypersonic flows (meaning in that region of the flow far from the coalescing free shear layer produced by the boundary layer separating around the cylinder, and downstream from the wake shock). These instabilities developed over several hundred diameters downstream of the cylinder. It would appear therefore that the structures observed here cannot be due to an instability of the outer wake of the wire either, since they appear in the shadowgraph much closer to the wire.

4.4.3 Wire vibration effect

Another possible source for the vortices observed in Figure 4.11 is a vibration of the wire itself, which might cause the vortex shedding to lock into this frequency. The

natural frequency of such a wire is given by

$$\omega_n = \frac{\pi\sqrt{(T/\delta)}}{L}, \tag{4.7}$$

where T is the tension in the wire; δ is the mass per unit length of the wire; and L is the length of the wire.

For the case of Figure 4.11, $L \approx 28\,\text{cm}$ and $\delta \approx 2.3$ g/m. The tension in the wire, due to the drag of the flow and the lift of the prongs supporting it (they are at a 1° angle of attack with respect to the flow in this figure), is estimated at approximately 20 N. Substituting these values into Equation (4.7),

$$\omega_n \approx 1000\frac{\text{rad}}{\text{sec}}, \tag{4.8}$$

which corresponds to a period of 6 ms. This frequency is more than an order of magnitude lower than what would be required to explain the structures observed in Figure 4.11, and therefore cannot be accountable for the structures observed.

A T5 control study

The combination of large yaw angles and supersonic (or transonic) flow over cylinders in the current experiment casts doubts on the applicability of past studies to the present situation. It was determined that the best way to eliminate these doubts was to run a control experiment where the effect of the wire on the flow could be independently studied. The goal of this control experiment was therefore to isolate the role of the wake of the wire in flows similar to those of interest here, from that of the shock-produced shear layer. The test configuration of this experiment was similar to the one discussed so far, and the flow condition used was the same. Taking advantage of the fact that the leading edge on the model can be changed easily, a sharp leading edge was mounted on the mainbody of the wedge, with setup shown in Figure 4.12. Thus, any shock curvature effects were eliminated from the flow, and the visualization was focused entirely on the effect of the wire on the flow. Finally,

wires of varying diameters were used, so that flows over a range of Reynolds number could be compared.

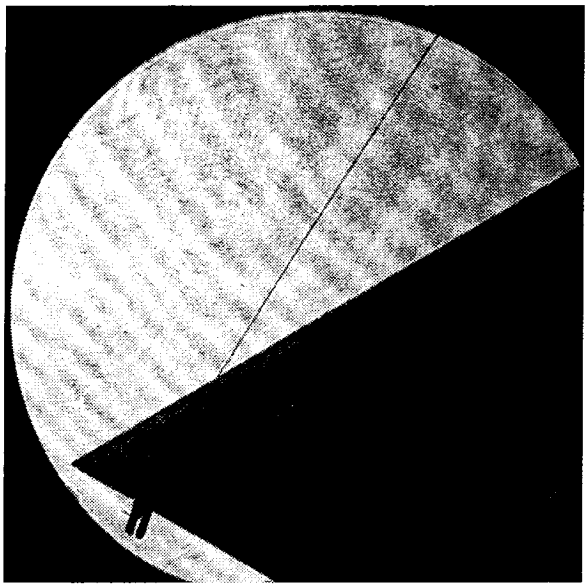

Figure 4.12. Sharp leading edge setup for wire control study in T5. Note that the wire is fitted through the leading edge so that the angle between the wire and the surface of the wedge is comparable to that of the experiment.

The results of this experiment are shown in Figure 4.13. They do not suggest that a significant broadening of the streak occurs as a result of the wire wake, or even that a favored mode of instability is present in the flow. Both of these would be present if the wake of the wire had become unstable. The streak shown in the figures does, however, exhibit turbulent features; these are believed to be the result of the ablation process of the sodium from the wire, and are comparable to the top streak of Figure 4.11. The computed wavelength of the structures that would be shed by a cylinder at a Strouhal number of 0.2 is included (to scale) in these figures. There does not appear to be a correlation with wire diameter in all three shots in this figure, suggesting that these types of flow do not exhibit the Karman vortex streets associated with incompressible flows across cylinders, but fall more in line with the observations of Behrens [1966], who noted that the instabilities did not develop until further downstream. As a result of this, we believe that the structures observed in Figure 4.11 are due to an instability in the shear layer produced by the curved shock.

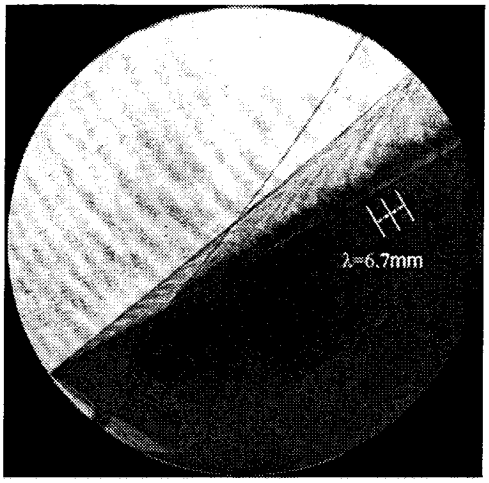

(a)

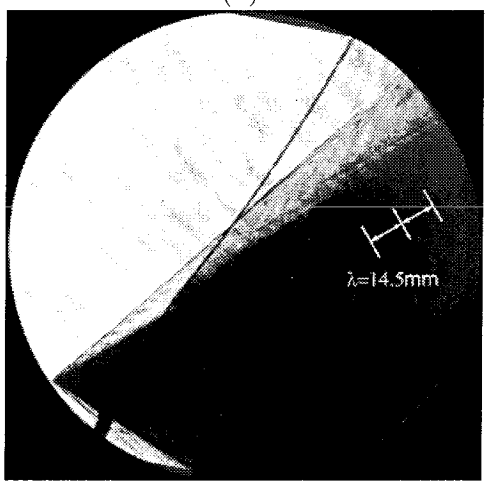

(b)

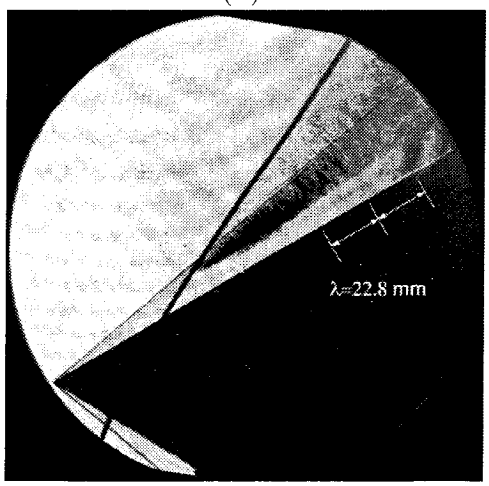

(c)

Figure 4.13. Test of the wire wake instability. All three shots use Condition 1 listed in Table 3.1. The wire diameters is the proper scaling parameter here. It is 0.5 mm in (a); 1.0 mm in (b) and 2.0 on (c). The corresponding (expected) wavelength is shown to scale in the figures.

4.5 Summary of results from SWSV

Sodium Wire Streakline Visualization (SWSV) was used to visualize the flow over the wedge model, using the three nitrogen test conditions described in Chapter 3, and repeated for convenience in Table 4.2. The estimated density ratios across the normal part of the shock (based on equilibrium calculations of the flow) for each of these conditions has been added to the Table. Carbon dioxide was also used as a test gas in some tests but the success of SWSV with this gas has been limited, because of continuing problem with the positioning of the sodium source on the wire too close to the intersection with the shock and with controlling the absorption level at the shot condition.

Table 4.2. Nominal T5 conditions and approximate density ratios for planar flow study.

	h_{res}	P_{res}	M_∞	U_∞	ρ_∞	T_∞	ρ_2/ρ_1
Condition 1	11 MJ/kg	20 MPa	5.7	4300 m/s	0.018 kg/m^3	1450 K	8.5
Condition 2	20 MJ/kg	27 MPa	5.0	5500 m/s	0.018 kg/m^3	3020 K	10.8
Condition 3	4 MJ/kg	14 MPa	6.2	2700 m/s	0.036 kg/m^3	580 K	6.2

More than one shot was performed at each condition over several series of experiments, seeding different regions of the shear layer. To summarize, the main purpose of varying these parameters was to determine whether or not the shear layer became unstable under these conditions by observing whether discernible structures existed within the sodium streaklines. Whenever such structures could be found, they were to be correlated with the nose radius of the model.

Eighty-eight shots were performed in this manner; in Table 4.3, they are broken down by series and by the type of leading edge used. Out of these shots, nine were performed using the sharp leading edge for the control study discussed previously. The remaining shots fall into the following groups:

- seven shots had improper exposure of the film, due to either excessive or insuf-

ficient light intensity at the time of the shot;

- thirty-three shots had no streaklines, due either to brittle crystals which broke off the wire before the film was exposed, or because the laser was tuned too far from the D-line spectrum, or because at the test condition used, very little absorption by the sodium atoms takes place (eight shots performed at Condition 3 fall into this group);

- twenty-one shots had visible streaks but did not exhibit clear signs of an instability in the shear layer. Some of these shots had problems with the salt crystal breaking off and tagging the flow randomly during the tests; others had problems due to the streakline source being too close to the point of intersection of the wire and the shock, as discussed earlier in this chapter. A few shots in this group also had clear streaklines that did not show evidence of an instability; and

- eighteen shots had streaklines in which some larger scale structures could be observed.

Table 4.3. Summary of Sodium Wire Streakline Visualization experiments conducted.

Series	Condition used, from Table 4.2	Leading edge radius	Number of shots
1	1,2	3.5 cm	24
2	1	1.9 cm	1[a]
3	1,2,3, CO2	1.9 cm	34
	1	(sharp)	9
	2	3.5 cm	7
5	1,2,3	6.35 cm	13

[a]SWSV experiments were aborted due to dye laser failure.

The last group of eighteen shots, which used either the absorption or the enhanced refractivity techniques discussed in this chapter to visualize the streaklines, may be

used to draw some conclusions about the stability of the shear layer produced by curved shocks. The quality of the data, however, varied significantly from one shot to the next, as many shots exhibited some of the problems associated with the sodium wire technique discussed in this chapter. The shots were therefore further subdivided into three categories to reflect different levels of confidence with which the wavelength of observed structures could be measured.

The shots for which structure wavelengths could be unambiguously measured over several cycles (such as the one shown in Figure 4.11), were put in a category called 'A'; those for which discernible structures could be seen, but for no more than 2 cycles, were classified in a category 'B'; and those shots exhibiting only one or two vortices over the span of the model, or where the flow was poorly resolved by the shadowgraph, were classified as 'C'.

Using these criteria, six shots fell within category 'A', five in 'B', and seven in 'C'. The shots in each of these categories are presented in Figure 4.16, Figure 4.17, and Figure 4.18, respectively. The wavelength of the structures measured in these shots is also overlaid (to scale) on the figures. Of the eighteen shots, eleven shots

Table 4.4. Summary of the eighteen shots with observable instability.

Category	Condition used, from Table 4.2	Leading edge radius	Number of shots
A	1	1.9 cm	3
A	1	3.5 cm	1
A	1	6.35 cm	1
A	2	1.9 cm	1
B	1	1.9 cm	2
B	2	1.9 cm	1
B	2	3.5 cm	1
B	2	6.35 cm	1
C	1	1.9 cm	3
C	1	3.5 cm	1
C	2	1.9 cm	2
C	2	6.35 cm	1

were at Condition 1 (five in Category A, two in B and four in C), and seven shots were performed at Condition 2 (one in Category A, three in Category B and three in Category C). There were no shots performed using either Condition 3 (low enthalpy nitrogen) or using carbon dioxide as a test gas that yielded visible streaklines with structures. The summary of these shots by category, condition and leading edge radius is presented in Table 4.4.

From the discussion and the results of Chapter 1 (see, *e.g.*, equation (1.16)), one important length scale in the shear layer produced by a curved shock is the shock curvature at the normal shock point. Since the shock curvature is itself a function of the model shape, the associated, physical dimension on the model is its leading edge radius. The wavelength data obtained from Figures 4.16 to 4.18 was plotted against the wedge leading edge radius. The result is presented in Figure 4.14.

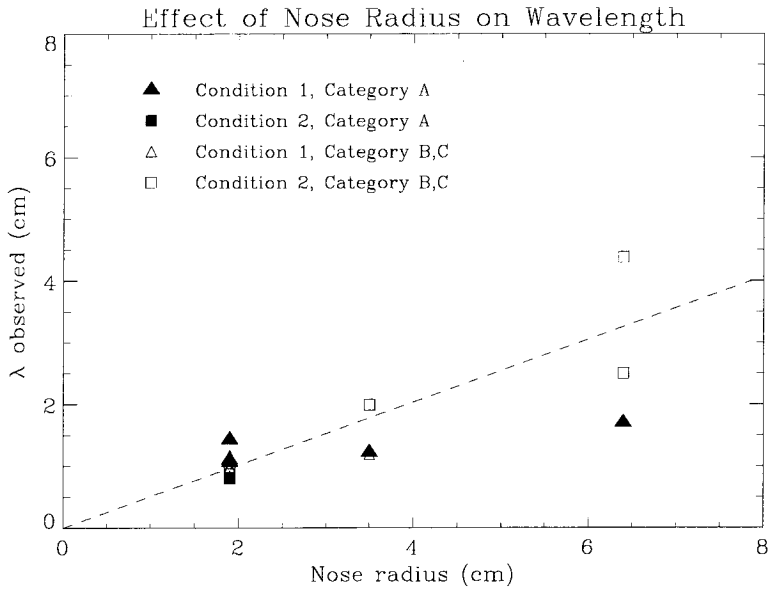

Figure 4.14. Correlation between the wavelength of the structures observed in the shear layer and the nose radius. The trend is obtained from Figure 4.15.

The overall trend of these data is that the observed wavelength tends to increase proportionally with increasing leading edge radius, within the range of leading edges used in this experiment. The same data, non-dimensionalized by the nose radius, are plotted in Figure 4.15 and are used to obtain an estimate for the correlation between

the two. This non-dimensionalized plot shows that there is a range of disturbance wavelengths, between approximately one third to three quarters of the leading edge radius, where the disturbances are more likely to be amplified in the shear layer. A best fit line through this plot suggests that the instability in the shear layer is most susceptible to disturbance wavelengths of about one half of the leading edge radius.

Finally, the fact that some shots were performed at very similar conditions and produced streaklines in which these instabilities were not evident suggests that in addition to the wavelength of the disturbances, there is also a minimum threshold in their amplitude at the conditions studied. The nature of piston-driven shock tunnels is such that the flow produced is intrinsically noisy, but it is difficult to estimate the level of the noise or the variation in its level from shot to shot. It would therefore appear that at these conditions in T5, the shear layer is only marginally susceptible to disturbances in the shock layer. This would mean that the density ratio across the bow region of the curved shock needs to be approximately ten or more before these instabilities develop. As mentioned in Chapter 3, this is close to the maximum density ratio that may be produced in T5 flows.

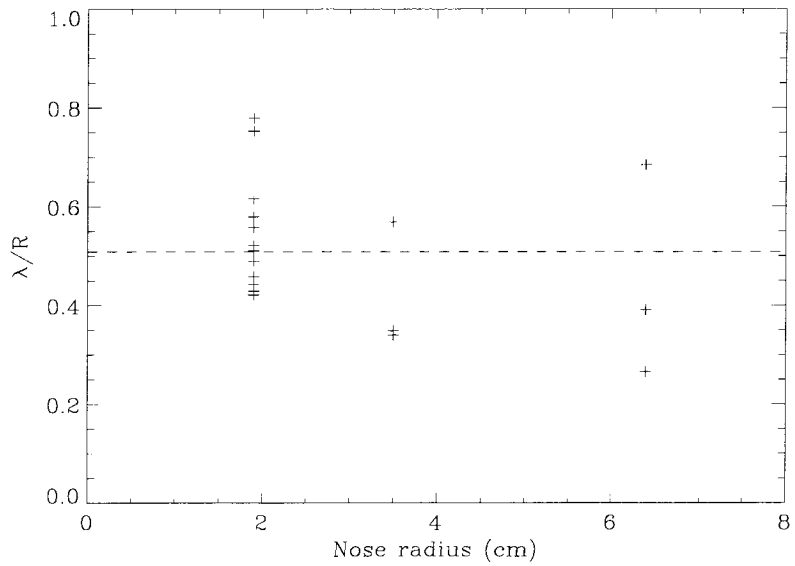

Figure 4.15. Plot of the wavelength observed in the shear layer, non-dimensionalized with the nose radius. The dash line is the arithmetic mean of the data.

While the results presented here are suggestive of an instability of the kind expected, they are not sufficiently convincing to draw firm conclusions on their own. For instance, the data points shown in Figure 4.14 and 4.15 have a relatively large spread, possibly due to the T5 test conditions which can produce only a limited density ratio and thus require large amplitude disturbances to trigger an instability in the shear layer. At significantly higher density ratios, lower disturbance amplitudes may be sufficient to trigger the same instability, *i.e.* one centered around a wavelength equal to approximately half of the leading edge radius.

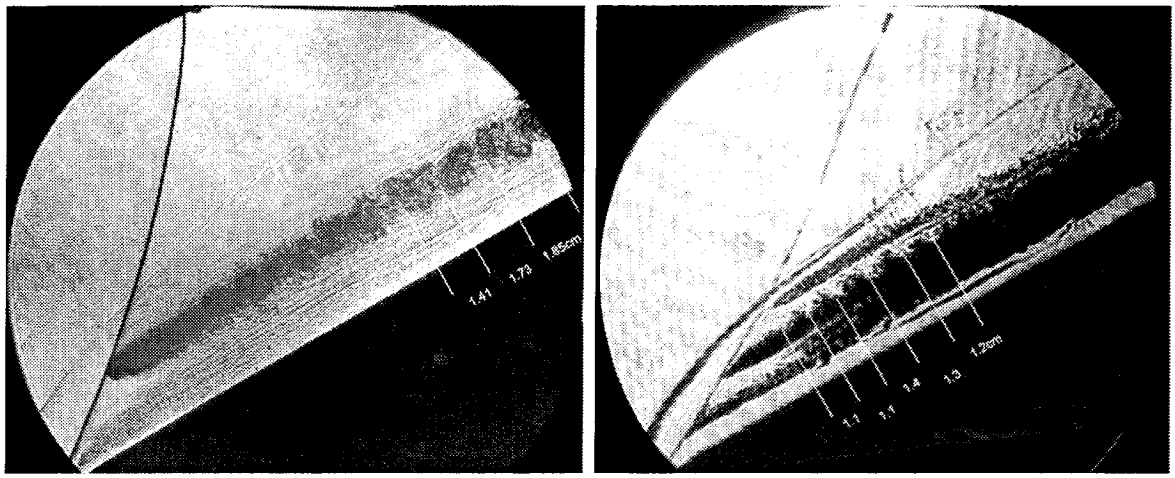

(a) Shot 1864
6.35 cm leading edge; Condition 1

(b) Shot 1339
3.5 cm leading edge; Condition 1

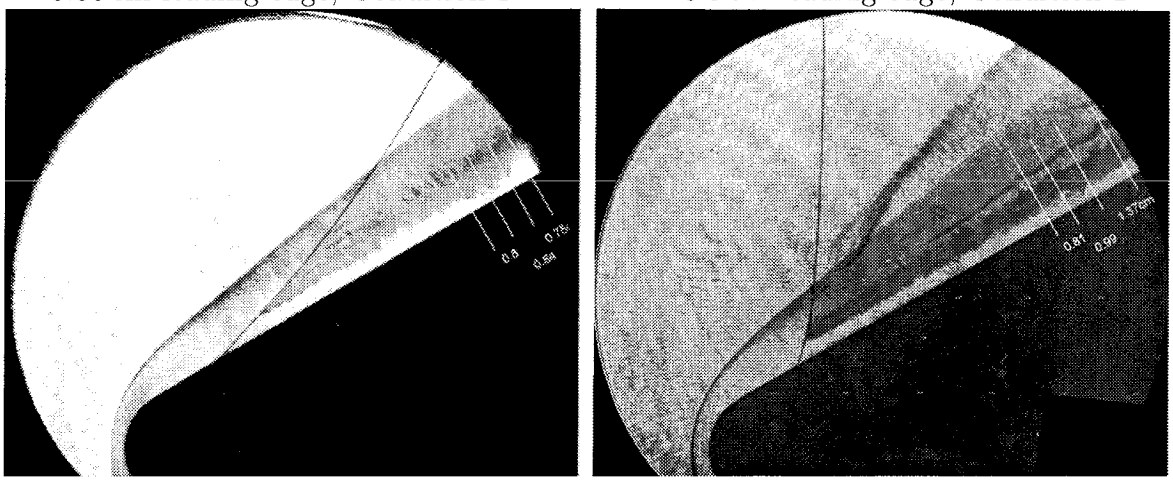

(c) Shot 1705
1.9 cm leading edge; Condition 2

(d) Shot 1710
1.9 cm leading edge; Condition 1

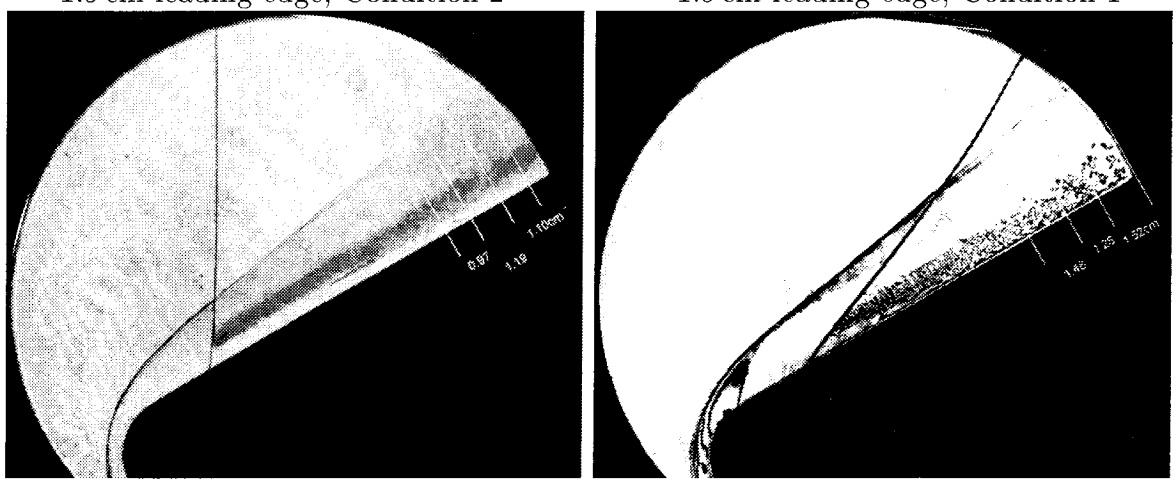

(e) Shot 1714
1.9 cm leading edge; Condition 1

(f) Shot 1685
1.9 cm leading edge; Condition 1

Figure 4.16. Shots in Category A.

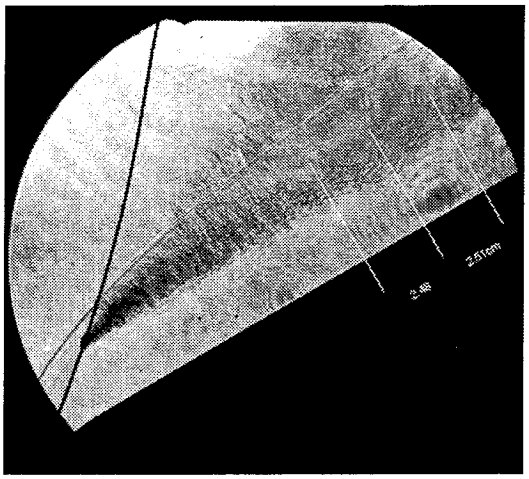

(a) Shot 1867
6.35 cm leading edge; Condition 2

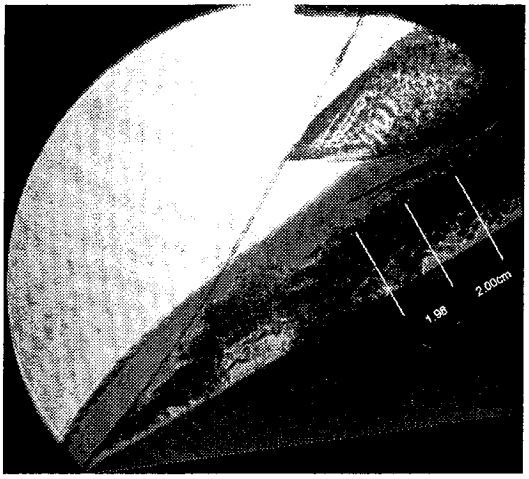

(b) Shot 1345
3.5 cm leading edge; Condition 2

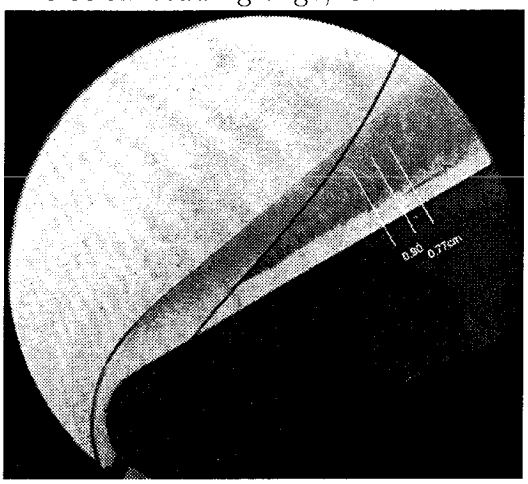

(c) Shot 1697
1.9 cm leading edge; Condition 1

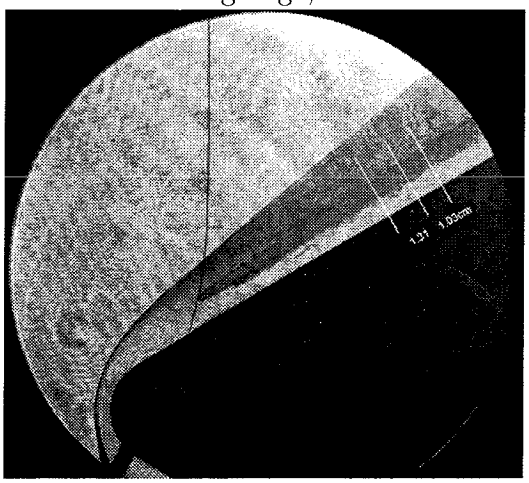

(d) Shot 1711
1.9 cm leading edge; Condition 1

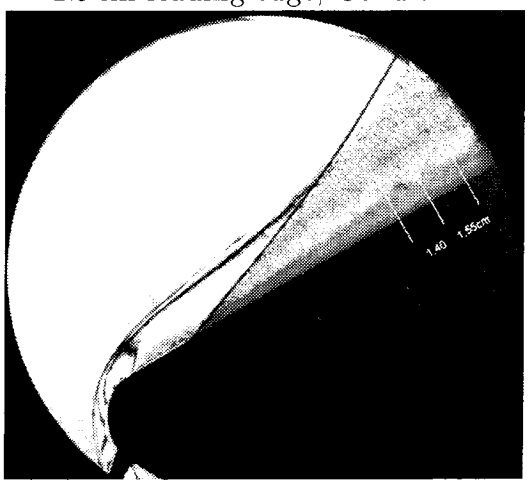

(e) Shot 1688
6.35 cm leading edge; Condition 2

Figure 4.17. Shots in Category B.

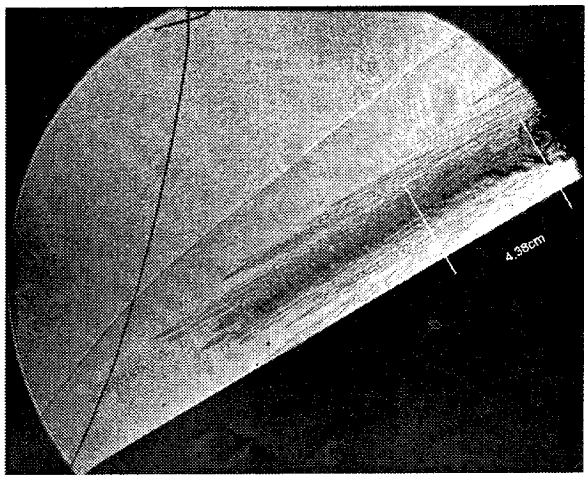

(a) Shot 1861
6.35 cm leading edge; Condition 2

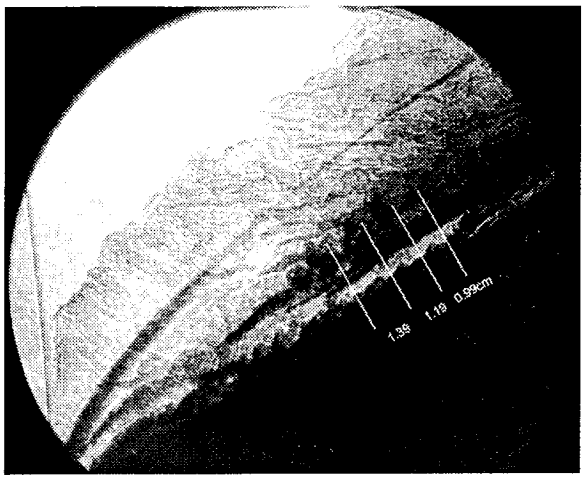

(b) Shot 1337
3.5 cm leading edge; Condition 1

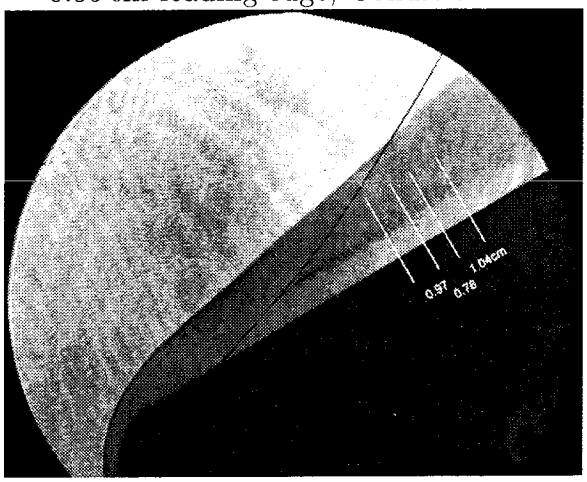

(c) Shot 1700
1.9 cm leading edge; Condition 2

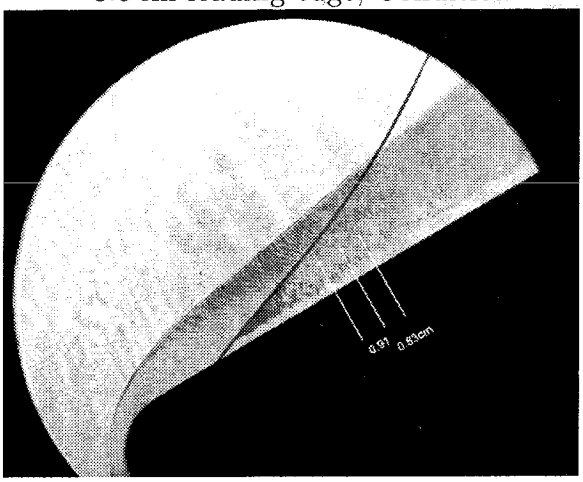

(d) Shot 1702
1.9 cm leading edge; Condition 2

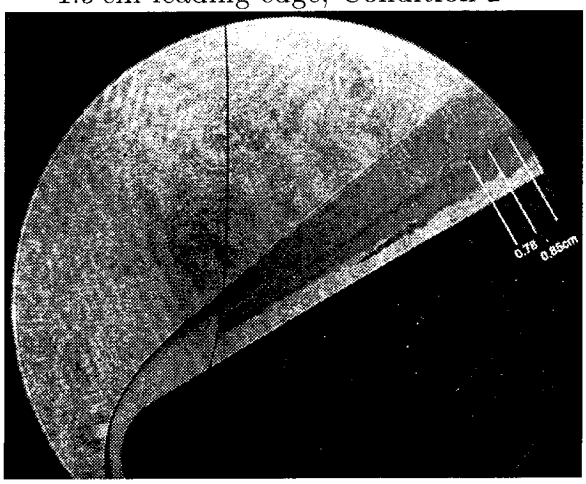

(e) Shot 1708
1.9 cm leading edge; Condition 1

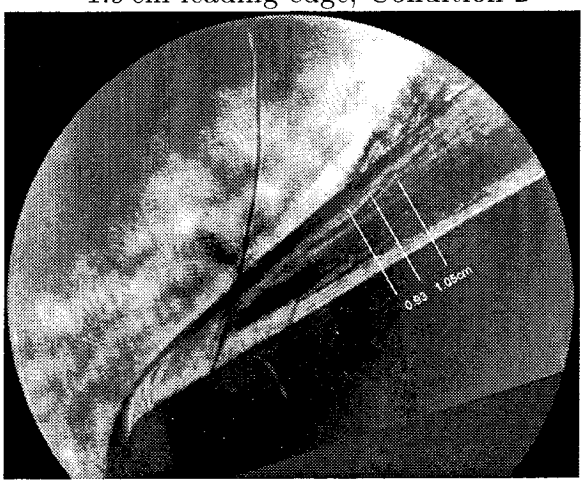

(f) Shot 1712
1.9 cm leading edge; Condition 1

Figure 4.18. Shots in Category C.

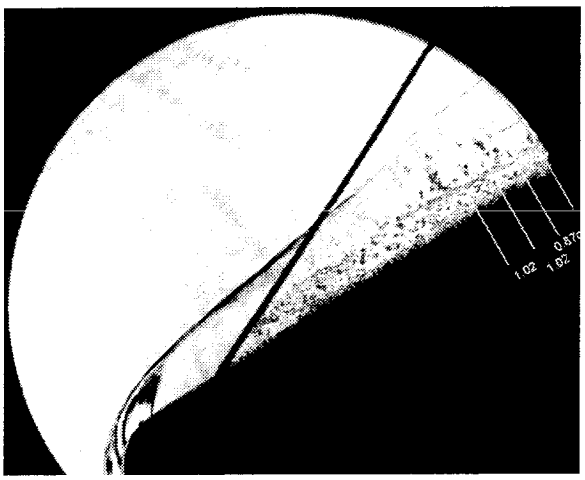

(g) Shot 1686
1.9 cm leading edge; Condition 1

Figure 4.19. Shots in Category C (continued).

Chapter 5 Flows with high density ratios

5.1 A numerical investigation of the stability of the shear layer at high density ratios

The stability of the shear layer produced by the curved shock over a hemicylindrically blunted wedge was investigated by Hornung [1998] using a flux-limited, operator-split Euler solver and the programming environment Amrita[1]. The intent of the simulation was to investigate the effect of the shear layer instability discussed in Chapter 4 in flows at high density ratio. For this purpose, inviscid, non-reacting simulations of the flow were made to simulate conditions closer to the Newtonian limit[2] than possible in the T5 test section. Choosing a ratio of specific heats of 1.1 and a Mach number of 9, simulations of flows with a density ratio of 16.8 across the normal part of the shock were performed. The grid used is body-fitted, and adaptive mesh refinement is used to give increased resolution in regions of high density gradients.

The non-uniformity of body-fitted grids is known to introduce numerical noise in the flow. The peak noise level introduced by the grid in these computations is typically 0.3% of the free-stream density, which is not enough to trigger an instability in the shear layer as shown in Figure 5.2(a).

5.1.1 Specifying external disturbances

In order to investigate the stability of the shear layer produced by the curved shock over the wedge, the prescribed free-stream flow over the wedge was modified to include a suitable source of oscillation at the inflow boundary in the form of a velocity oscillation which varied from zero at the axis of symmetry to a prescribed peak at

[1]For a description of Amrita, see Quirk [1998].

[2]The term 'Newtonian limit' refers to hypersonic flows with vanishingly thin shock layers, where the density ratio across the shock is infinite.

a position corresponding roughly to the shock ordinate of the point of maximum vorticity generation at the shock and back to zero again at the upper limit of the computational domain.

The prescribed flow disturbance in the free-stream was chosen as

$$\frac{V}{U_\infty} = A(y/R)\sin(\frac{2\pi U_\infty t}{\lambda}) , \tag{5.1}$$

where V is the y–component of velocity, R is the nose radius, t is time, and λ is the wavelength of the disturbance. A plot of the amplitude function A is shown in Figure 5.1.

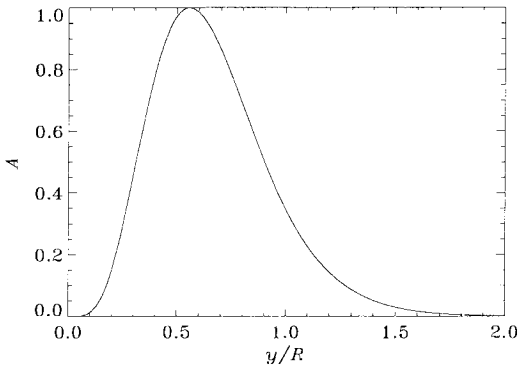

Figure 5.1. Amplification function to control the position of the free-stream noise.

The maximum amplitude of the disturbances was set at 1% of the free-stream speed, meaning that an oscillatory y-component of velocity, up to 1% of the free-stream velocity, is imposed at the inflow boundary. The wavelengths investigated (referring to disturbances introduced in the free-stream) were λ/R = 0, 0.333, 0.733, 1.0, 1.5, and 3.0. The effect of these disturbances on the flow is shown in Figure 5.2.

Certain important features of the flow become apparent from this investigation. At imposed wavelengths of 1/3 of the nose radius or less, the disturbances do not appear to grow in the shear layer and their effect is negligible. When the imposed wavelengths are close to the nose radius of the body, however, significant changes occur in the flow. Small structures develop rapidly in the shear layer, as shown in 5.2(c). These structures travel supersonically with respect to the flow between the shear layer and the body so that oblique shocks form and reflect off the body surface and reimpinge upon the shear layer. Further downstream, the preferred wavelength of the visible structures appears to increase, approaching the wavelength most apparent

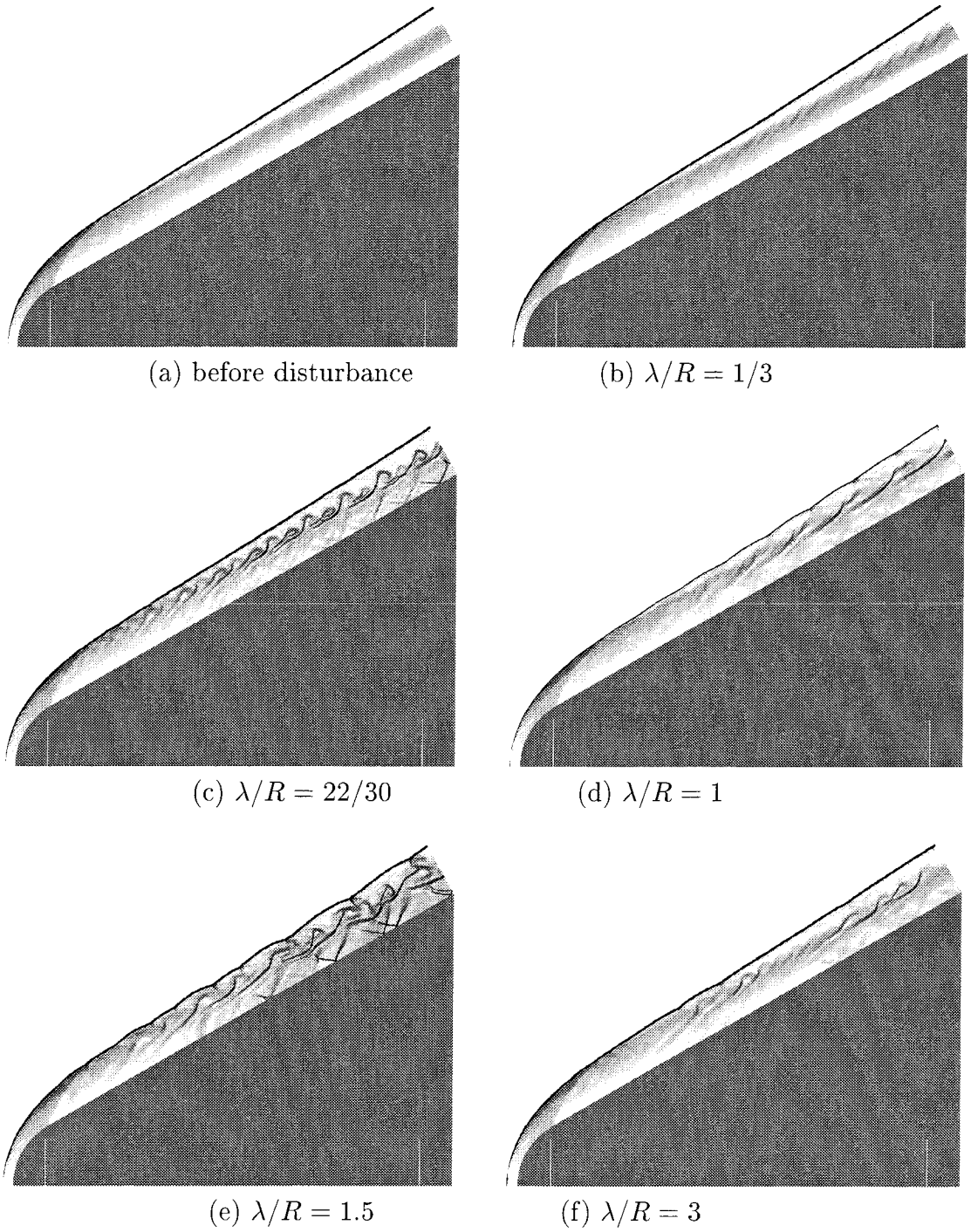

(a) before disturbance (b) $\lambda/R = 1/3$

(c) $\lambda/R = 22/30$ (d) $\lambda/R = 1$

(e) $\lambda/R = 1.5$ (f) $\lambda/R = 3$

Figure 5.2. Computed effect of disturbances on the shear layer over a cylinder wedge. The prescribed disturbances, of wavelength λ, are introduced in the free-stream on the left-most boundary. The images are fractional pseudo-schlieren visualization of the computed flow. Grey shading is a monotonic function of the magnitude of the fractional density gradient. The density ratio at the normal point on the shock is about 16.8. The amplitude of the disturbances is 1% of the free-stream velocity in all cases except in (a) where the flow is undisturbed.

in 5.2 (d), at $\lambda/R = 1$. At that point and slightly above (*i.e.*, $\lambda/R = 1.5$), the large scale structures deform the main shock, causing visible triple points to occur on it. At the imposed wavelength $\lambda/R = 3$ and above, the growth rate is reduced again.

Since the frequency of the imposed disturbances does not change as they pass through the shock, the ratio U/λ must be preserved. The structures that appear in Figure 5.2, amplified from the free-stream disturbances, therefore have shorter wavelengths in the shock layer than in the free stream. These structures are sufficiently clear that their wavelength in the shear layer may be measured directly. This is done in Figure 5.3, for the cases where the imposed wavelengths are 0.733 and 1, respectively. The results fall well within the range of the experimental data shown in Figures 4.14 and 4.15 and also show that the preferred wavelengths are somewhat distributed, *i.e.*, not confined to a single value.

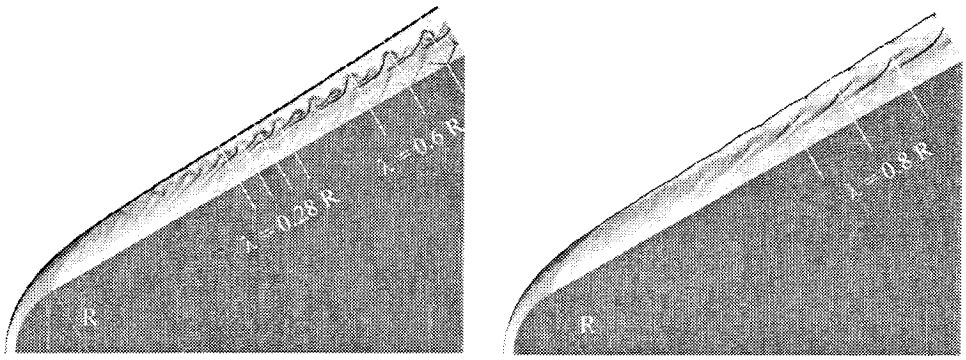

Figure 5.3. Measured wavelength of the structures observed in Figure 5.2 (c) & (d).

5.1.2 The preferred wavelength compared to the vorticity thickness

Another length scale of importance is the vorticity thickness of the shear layer. In the case of a free shear layer, for instance, the vorticity thickness is the most important length scale in the flow. The wavelength of the structures that develop within such a shear layer are broadly distributed around the mean value $\lambda = 3.5\,\delta_\omega$, where δ_ω is the vorticity thickness (see Roshko [1992]). Since a free shear layer thickness (and its

associated vorticity thickness) grows with downstream distance, the mean wavelength of the structures observed grows in the same way. We wish to determine whether the vorticity thickness is related in a similar way to the wavelength of the structures observed in Figure 5.3 and in the experiments described in Chapter 4.

Using the velocity profile across the shock layer for the undisturbed case of Figure 5.2(a), the vorticity thickness was computed using the maximum slope method. In this method, a line is drawn tangent to the velocity profile at the inflection point in the shear layer; the distance, normal to the flow, between each of the points at which it intersects the asymptotes of the velocity profile and a line drawn through the inflection point in the direction of the flow, determines the vorticity thickness. The method is illustrated in Figure 5.4.

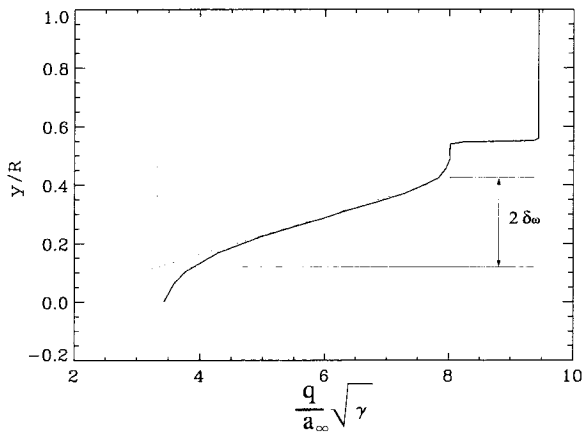

Figure 5.4. The vorticity thickness δ_ω, defined by the shear layer maximum slope. The shear layer profile is based on data obtained in a traverse of the flow shown in Figure 5.2(a). The traverse is made in a direction normal to the body, starting at the body surface and going beyond the shock into the free-stream. The velocity q, non-dimensionalized by the free-stream speed of sound a_∞ and the square root of the ratio of specific heats, is represented by the solid line in the plot. The jump in velocity across the shock is evident in the figure. Note that the velocity at the body surface does not quite reach the asymptotic limit, estimated here by the leftmost dash line.

The vorticity thickness is therefore approximately 15% of the nose radius in this case. Assuming a mean expected wavelength of 0.5 nose radii in the shock layer (obtained in the experiment and close to what is seen in Figure 5.3), the ratio of the wavelength observed to the vorticity thickness is approximately 3.5, in good agreement with the expected wavelength of structures in a free shear layer.

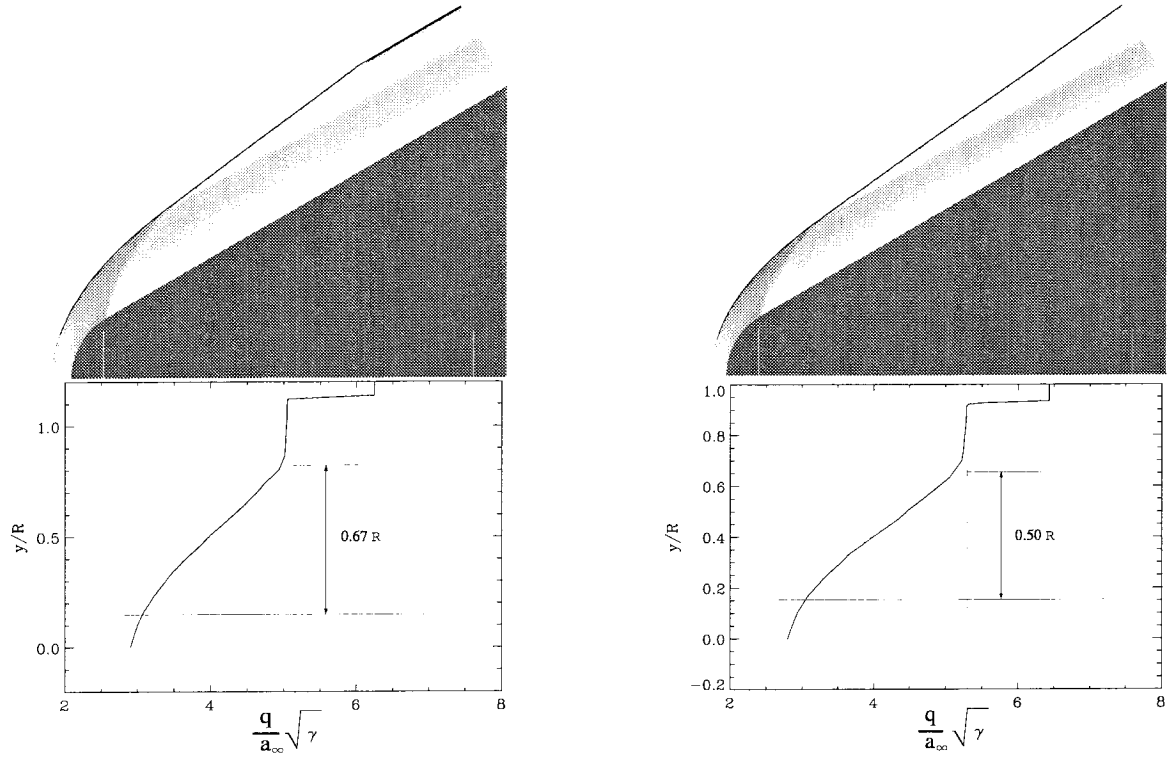

(a) $\rho_2/\rho_1 = 8.4$

(b) $\rho_2/\rho_1 = 10.46$

(c) $\rho_2/\rho_1 = 14.9$

(d) $\rho_2/\rho_1 = 16.8$

Figure 5.5. The vorticity thickness over the wedge, at four density ratios. The traverses are taken along a line midway between the two white lines on the body. The discontinuity in the shock in (a) is caused by the limited size of the grid domain. It does not affect the flow in the region where the traverse is made. No disturbances have been added to the flow.

Several additional simulations of the flow over the wedge were performed, using density ratios across the normal shock of 8.4, 10.5 and 14.9 (the example discussed so far had a density ratio of 16.8). The geometry of the wedge is unchanged in these simulations. Varying the density ratio across the shock accomplishes several things:

- it directly affects the thickness of the shear layer, and therefore the vorticity thickness,
- it enables the investigation of the minimum disturbance amplitude required to produce visible instability in the shear layer (over the length of the wedge used in these computations), as a function of density ratio, and
- it enables testing whether the structure wavelengths scale like the nose radius (*i.e.*, the wavelength remains unchanged at the different conditions) or whether they scale like the vorticity thickness.

The vorticity thickness, as defined in Figure 5.4, is shown for these four different cases in Figure 5.5. Clearly, the vorticity thickness is largely affected by the density ratio. At infinite density ratio, the shock layer is infinitesimally thin and the vorticity thickness is necessarily zero. The trend is illustrated by plotting the vorticity thickness versus the inverse of the density ratio. The result is presented in Figure 5.6. The effect on the preferred wavelength is discussed next.

5.1.3 Effect of the density ratio on the wavelength of the structures in the shear layer

An investigation of the effect of the vorticity thickness on the stability of the shear layer was conducted; the results of this investigation are presented in Appendix C. In this study, the conditions used for the three lower density ratios in Figure 5.5 were subjected to free-stream disturbances of varying wavelengths and amplitudes for the purpose of determining whether the vorticity thickness changed the preferred wavelength of the structures observed in Figure 5.2.

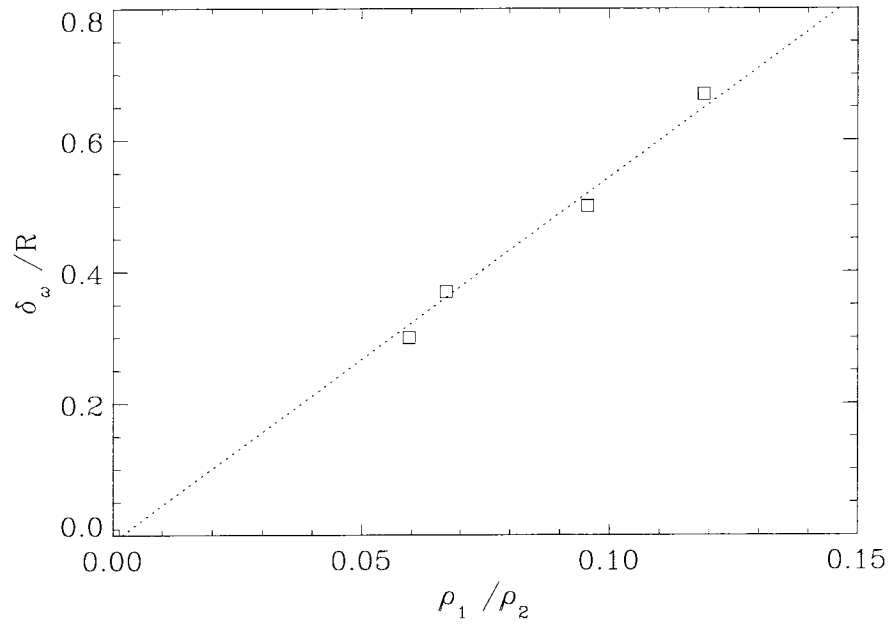

Figure 5.6. The vorticity thickness versus the inverse density ratio across the normal part of the shock, for the computations shown in Figure 5.5.

This investigation suggests that the preferred wavelength scales to some extent with the vorticity thickness. The main effect of an increase in vorticity thickness is twofold:

1. The effect of disturbances of a given amplitude in triggering a visible instability is greatly reduced with the larger vorticity thicknesses. For example, disturbance amplitudes of 2% (at any frequency) have a barely perceptible effect on the shear layer with a vorticity thickness of 0.67 R. This is consistent with the low density ratios associated with large vorticity thickness (see Figure 5.6), which results in lower vorticity throughout the shear layer.

2. The range of wavelengths of the structures that appear in the shear layer is increased with larger vorticity thickness. For example, free-stream disturbances with wavelength as high as four times the nose radius still produce visible structures in the shear layer at density ratio of 8.4 and 10.5, whereas disturbances of the same wavelength do not grow in a shear layer at density ratios of 15 and

above.

5.1.4 A numerical simulation of flows with density ratio of twenty five

Figures 5.2(c) and 5.2(d) illustrate the effect that an instability in the shear layer associated with a curved shock with a maximum density ratio of 17 may have on the shock shape. To better appreciate the effect of very high density ratios on the stability of the shear layer, the flow was computed over a wedge at a $M_\infty = 10$ and $\gamma = 1.05$ (corresponding to $\rho_2/\rho_1 = 29.3$ across the normal part of the shock). Such a condition provides useful insight into what might happen near the Newtonian limit, especially in terms of the minimum disturbance level required to trigger a visible instability in the shear layer.

The result, presented in Figure 5.7, suggests that the flow loses all order, even when disturbed by only the slight noise generated by the grid. The turbulence is so

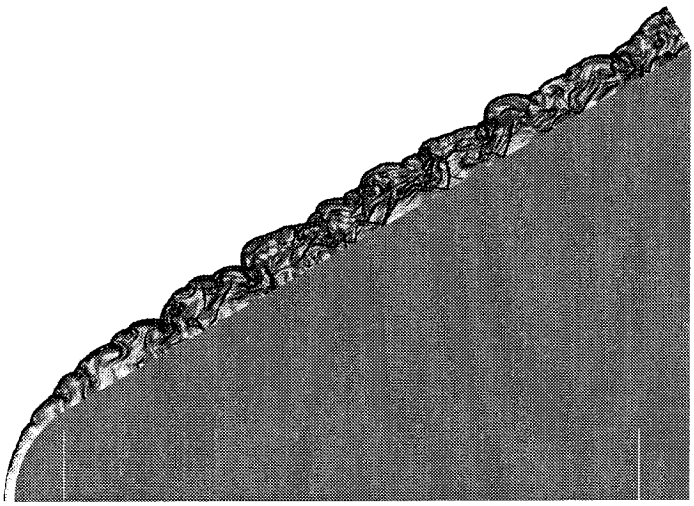

Figure 5.7. Computed flow over a wedge at a density ratio of 29.3. No external disturbances are added to the flow.

complete that it is no longer possible to detect a favored wavelength for the structures in the shear layer. The effect of this is a breakdown of the shape of the shock, a

feature that had only started to appear in computations at a density ratio of 16.8 (see Figure 5.2(c)) when the shear layer was excited at the right frequency. Thus, this phenomenon becomes more pronounced as the Newtonian limit is approached.

It is not suggested that specific features seen in in the two-dimensional flows of Figure 5.7 correspond to real flows, but if even the qualitative trend that is observed in the simulations as the Newtonian limit is approached is real, the consequences for real flows would be important. A series of experiments aimed at visualizing flows closer to this regime than possible in the T5 test section was therefore undertaken.

5.2 The T5 Light Gas Gun experiments

The standard configuration of T5 cannot produce flows with density ratios exceeding about 12 over a test model. Higher density ratios are theoretically possible, however, for objects traveling at high speed in a gas having a low ratio of specific heats, as shown by Equation (1.17). Thus, sending a projectile into such a gas at sufficiently high speeds provides a simple way to study flows at very high density ratios. The T5 Light Gas Gun facility, described in Chapter 3 is therefore ideally suited for this purpose.

5.2.1 Selection of a test gas

In polyatomic molecules, the rise in temperature associated with the passage through a normal shock causes vibrational excitation of the gas molecules, which lowers the ratio of specific heats and increases the density ratio. Moreover, the endothermic chemical reactions characterizing the dissociation of gas molecules after passage through a strong shock causes the temperature to decrease along streamlines, as chemical equilibrium is reached. The pressure is relatively unaffected by this, so that the thermal equation of state demand that the density increases along streamlines (provided that the molar mass of the mixture does not change too much). These two effects combine to produce higher density ratios across the shock than if the gas was perfect (with its

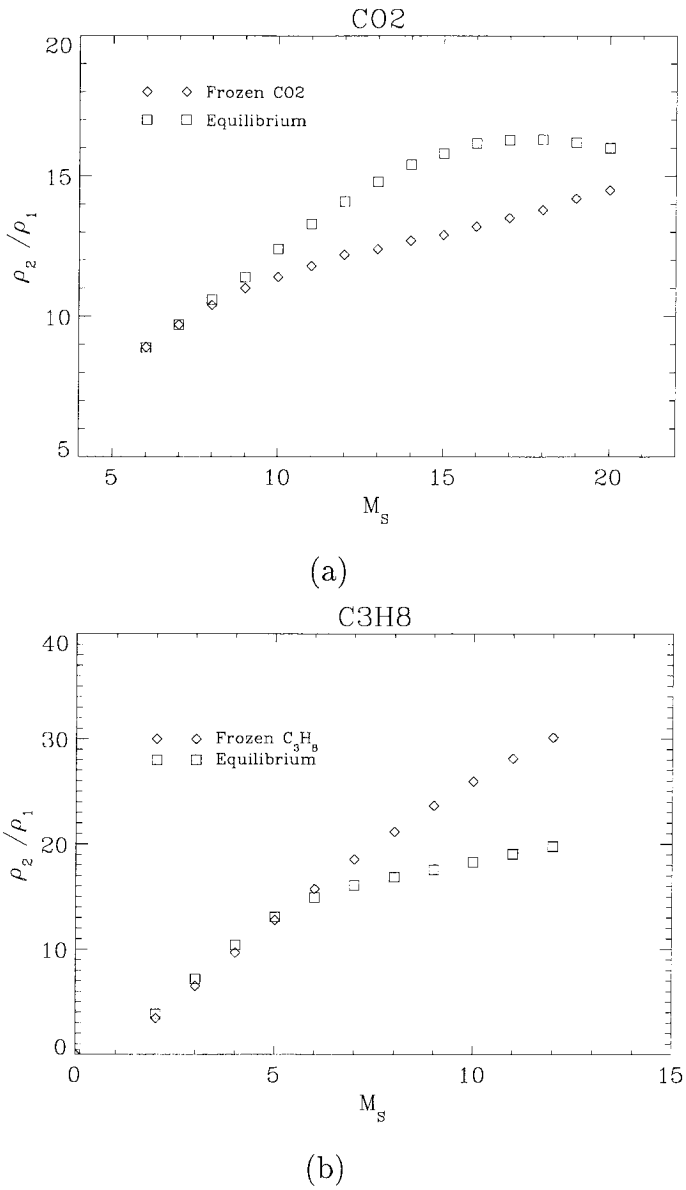

Figure 5.8. Computed density ratio versus Mach number for normal shocks in carbon dioxide (a) and propane (b).

γ fixed at room temperature), making it possible to reach density ratios close to 20 in real gases.

Two gases were considered to produce a large range of density ratios: carbon dioxide and propane. Density ratios were computed for the two limiting cases of frozen and equilibrium flows using STANJAN (see Reynolds [1986]). These computations assume that the gases are in thermodynamic equilibrium downstream of the shock

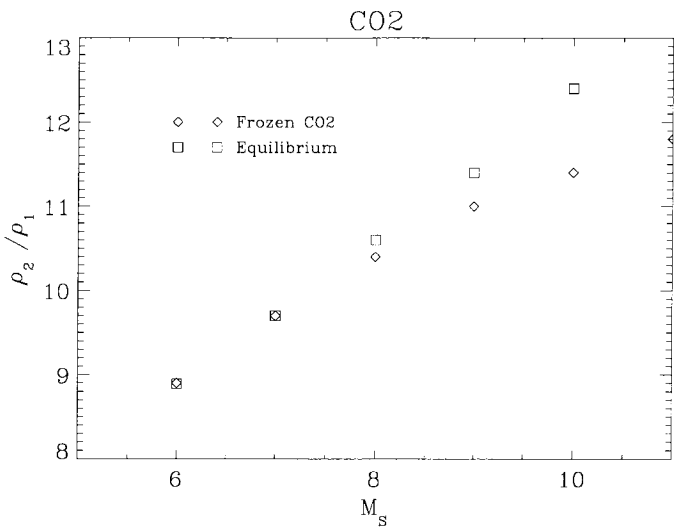

Figure 5.9. Density ratio across normal shock in CO_2 versus Mach number for the range of conditions applicable to the gun experiment.

in both cases. The density ratios obtained in this manner are plotted against Mach number in Figure 5.8. In the region immediately downstream of the curved shock the gas is in a state of chemical non-equilibrium so that the effective density ratio, for the sake of vorticity production, is bracketed by the two curves. In the case of carbon dioxide for the range of conditions of interest (M=10 and less), the difference between the frozen and equilibrium limits is small (see Figure 5.9) so that the density ratio may be approximated closely.

The dissociation of the gas after the shock ultimately causes the density ratio to decrease, as can be seen in Figure 5.8. When the degree of dissociation of the gas reaches a certain level, the molar mass of the resultant gas mixture is substantially reduced compared to the non-dissociated gas, so that the net effect is a reduction in density ratio compared to the frozen solution. In carbon dioxide this point is reached at a Mach number of approximately 22, while in propane it occurs much sooner, at a Mach number of approximately 5.

Thus, for the upper limit of operation of the T5 Light Gas Gun in these experiments (approximately 2700 m/s, or $M \approx 10$ in CO_2 and $M \approx 11$ in C_3H_8), propane appears well-suited for running experiments at density ratios nearly twice as high as

that achievable in T5 tunnel operation.

5.2.2 Sources of disturbances in the shear layer produced by a projectile

In Figure 5.7 the instability causing the breakdown of the shock layer and shock shape was triggered by small disturbances produced by the grid. Disturbances must be present for an instability to develop in the flow even at high density ratios.

Unlike the test gas in the typical free-stream in T5, the gas in the test section of the Light Gas Gun is stationary. No external disturbances are added to the flow in the experiments. Any disturbance affecting the shear layer must therefore be produced by the projectile itself.

The boundary layer as a source of disturbances

A turbulent boundary layer in hypersonic flow is a convenient source of disturbances in the flow for this experiment. Germain [1994] showed that structures in the turbulent boundary layer on a cone in hypervelocity flows can cause small shocks to propagate in the shock layer. To determine whether the boundary layer is turbulent in the Light Gas Gun experiments, the Reynolds number, based on projectile diameter, is estimated for the lowest speeds expected. For propane this is 1260 m/s; for carbon dioxide, it is 2200 m/s. The Reynolds number is defined as:

$$Re_d = \frac{\rho U_\infty d}{\mu}. \tag{5.2}$$

The diameter of the spherical projectile is fixed throughout the experiments at 2.54 cm. The density and temperature are computed based on equilibrium calculations across the normal shock at the given speed using STANJAN.

The viscosity is estimated from kinetic theory, which specifies that the dynamic viscosity is proportional to the square root of the temperature. The sample results computed in this way give an estimate of the minimum Reynolds number over the

projectile in all experiments. They are tabulated in Table 5.1.

Table 5.1. Sample Reynolds number calculations for 25.4 mm diameter projectile in Light Gas Gun experiment.

	speed [m/s]	T_2 [K]	μ_2 [N·s/m^2] kinetic theory	ρ_2 [kg/m^3]	Re (min)
C_3H_8	1260	630	1.60E-5	22.6	4.45E7
CO_2	2200	2170	3.86E-5	19.0	1.67E7

A conservative analysis thus places the Reynolds number in the tens of millions for the Light Gas Gun experiments. The boundary layer is therefore turbulent.

5.2.3 Results of the experiment

The data recorded in the Light Gas Gun experiments consists of shadowgraphs of the flow over the projectiles and speed measurements, as described in Chapter 3. Two types of projectiles were used in the experiments: nylon and polycarbonate (see Chapter 3 for details regarding material selection). Nylon projectiles were initially used in all experiments but the high pressure required to produce the higher speeds desired invariably caused them to fragment. The discontinuity on the projectile surface thus produced has an effect on the shock, which makes it difficult to separate from the effect due solely to the shear layer instability. Figure 5.10 shows an example of a projectile traveling at 2400 m/s through carbon dioxide. The density ratio is approximately 11.3. The shock, in the region where the projectile is damaged, experiences a bulge. The shear layer is clearly being disturbed by shocks produced at the broken surface of the projectile. Our numerical investigation of flows at varying density ratios (see Appendix C) showed that at this condition the amplitude of the disturbances needs to be about 4% to cause visible effects on the shear layer stability. The effect of this disturbance on the shear layer is seen for some distance downstream in Figure 5.10. The side of the projectile that is not damaged does not exhibit an instability in the shear layer.

Experiments at density ratios less than 15

For the shots where the projectile appears intact in the shadowgraph disturbances produced by the turbulent boundary layer are insufficient to cause a visible instability in the shear layer (consistent with the flow over the lower part of the projectile in Figure 5.10). Figures 5.11 and 5.12 show the results obtained in propane and carbon

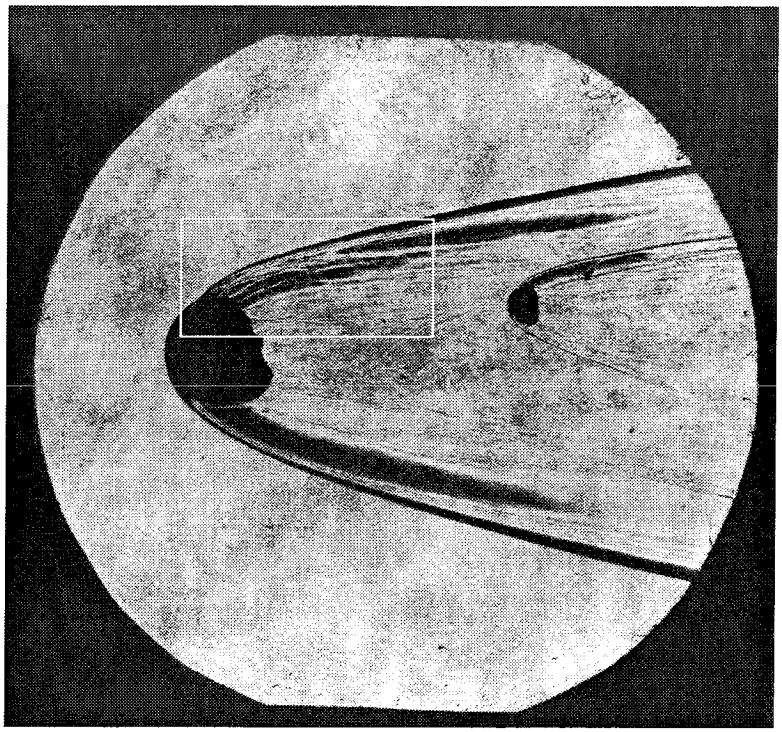

(a)

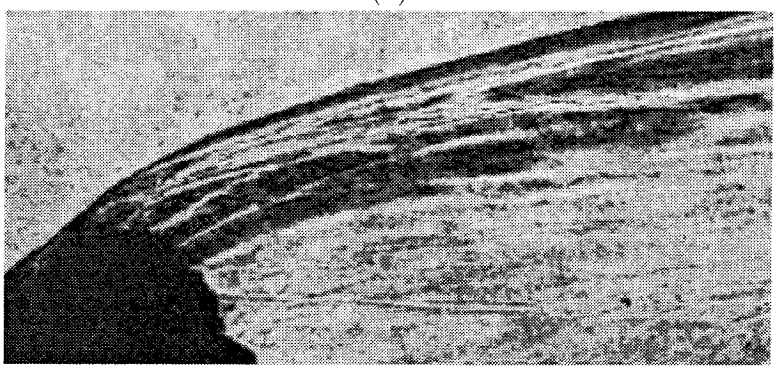

(b)

Figure 5.10. Broken projectile traveling at 2400m/s in CO2. The density ratio is approximately 11.3. Figure (b) shows a bulge in the shock near where the projectile has been damaged.

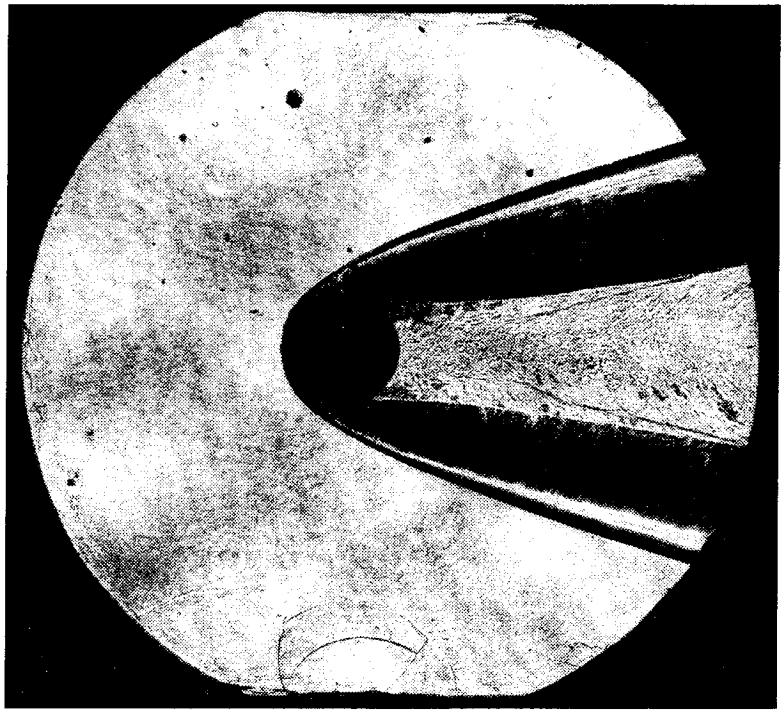

(a)

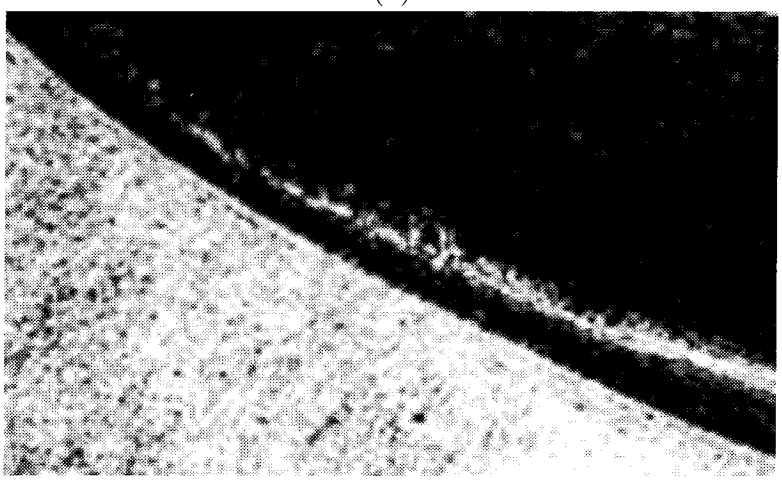

(b)

Figure 5.11. Density ratio below 15: the projectile is traveling at 1260m/s in C_3H_8. The shock is smooth at this density ratio. The figure in (b) shows an enlargement of the shock surface near the region of maximum vorticity generation.

dioxide. The projectile is traveling at 2700 m/s in carbon dioxide shot and 2260 m/s in propane corresponding to density ratios of approximately 12 and 13, respectively. Even with the remarkably thin shock layer around the projectile due to the high Mach number in Figure 5.12, the shear layer appears unperturbed at this density ratio. The

similar density ratio achieved in propane occurs at less than half the speed, explaining the distinctly different shock shape. Again, the shock is smooth and exhibits none of the effect of an unstable shear layer.

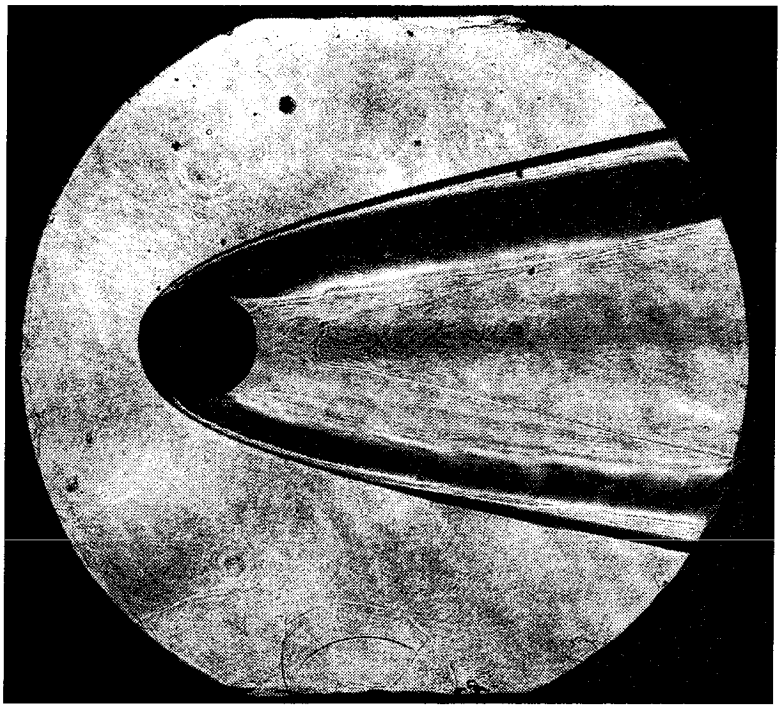

(a)

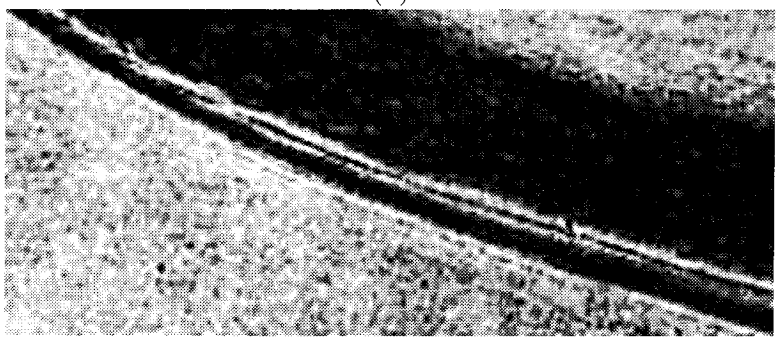

(b)

Figure 5.12. Density ratio below 15: the projectile is traveling at 2700m/s through carbon dioxide. Figure (b) shows an enlargement of the shock surface near the region of maximum vorticity generation.

Experiments at density ratios above 15

Results from shots performed at density ratios above 15 are presented in Figures 5.13 and 5.14. The distinctive shock perturbations predicted in the numerical simulation presented in Figures 5.2 and 5.7 are clearly apparent in these figures.

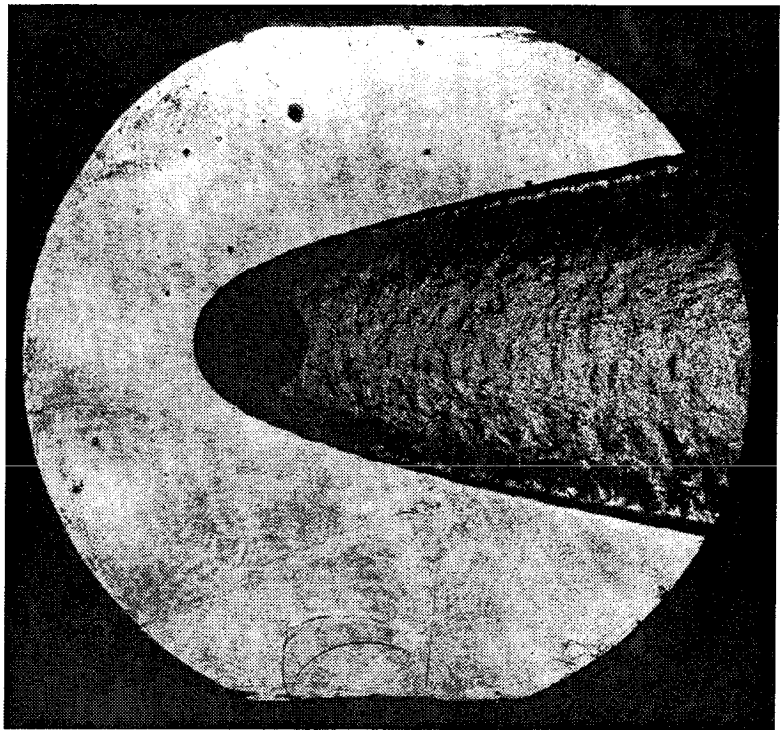

Figure 5.13. Density ratio above 15: projectile traveling through propane at 2200m/s, corresponding to $\rho_2/\rho_1 = 17.3$ (equilibrium).

The enlargement of the shock profile near the bow region (Figure 5.14(b)) highlights the irregularity of the profile. The axisymmetric nature of the flow around the projectile means that the perturbations of the shock may also be observed through the wake, immediately behind the projectile. The periodic features of the shock perturbation is evident in the figures. The density ratio in these shots is about 18 and 20, respectively. Thus, the experiment provides an upper bound on the lower limit of the density ratio across the normal part of the shock, at which small disturbances (of the order of those produced by a turbulent boundary layer) are sufficient to cause a breakdown in the shape of the shock in real gas flows commensurate with the predictions of numerical studies in perfect gases.

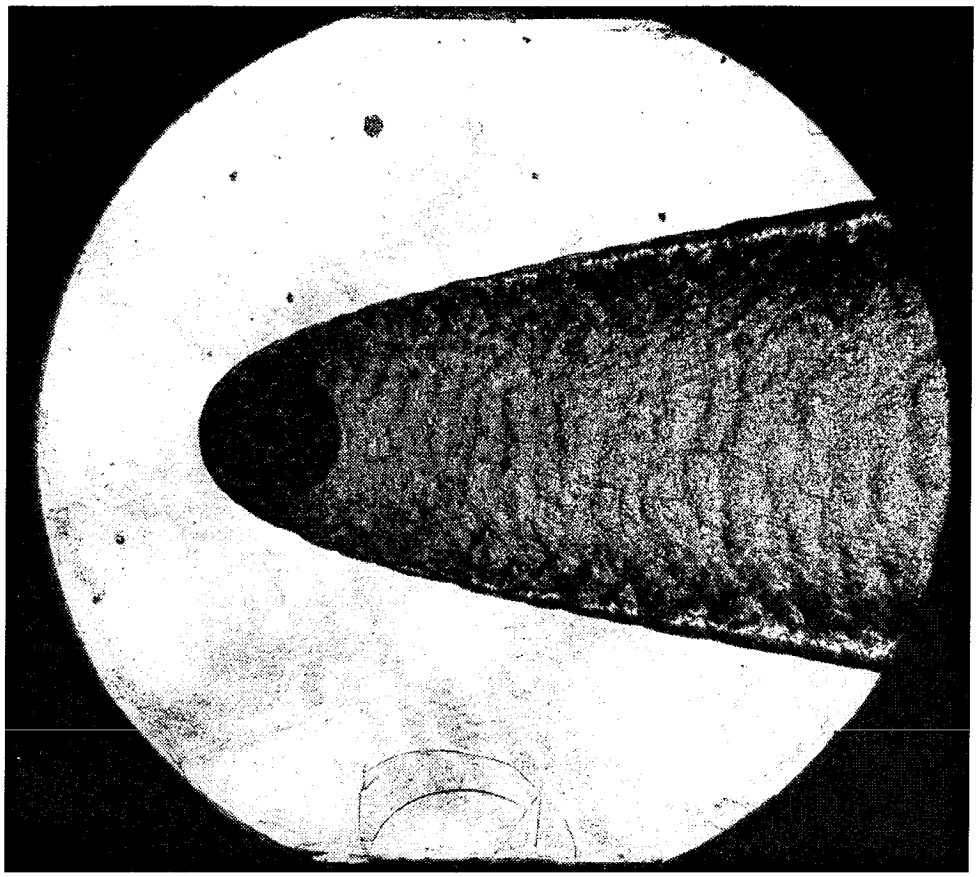

(a)

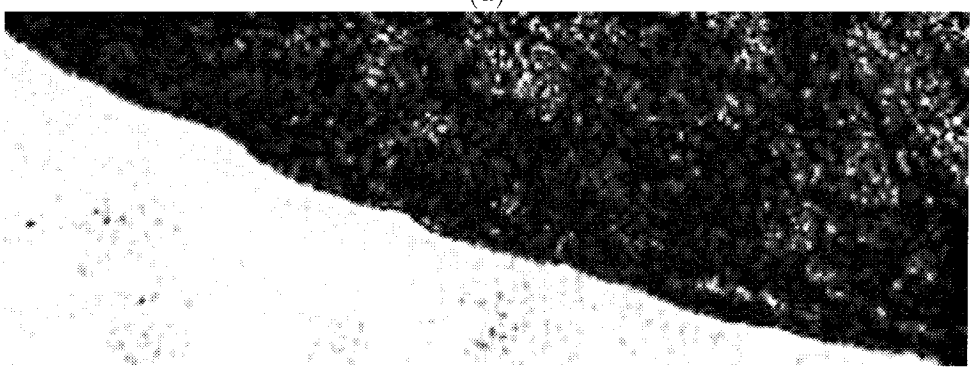

(b)

Figure 5.14. Density ratio above 15: projectile traveling through propane at 2700m/s, corresponding to $\rho_2/\rho_1 = 20$. Figure (b) shows an enlargement of (a) near the region of maximum vorticity generation. Note the undulations on the shock surface.

Interpreting the shadowgraphs

The shadowgraphs shown in this chapter feature dark bands in the shock layer over the projectile. These were found to be caused by a combination of the refractivity

of the gas in the shock layer and the geometry of the optical system. Light that is bent beyond a certain angle, in the configuration used in the T5 Light Gas Gun experiments, does not reach the photographic plate. Although the contrast in the shock layer that results from this appears to be excessive, it does not affect the results presented here.

A detailed discussion of this caustic effect is included in the Appendix D.

5.3 Comparison with numerical simulations

The distortion of the shock predicted by the numerical simulations at high density ratios was confirmed experimentally. The qualitative features of the flow in the experiment may be correlated better when compared with a computation over a similar body. The flow over a sphere at conditions similar to those of the experiments was therefore computed to determine whether the value of the density ratio at which the shear layer was experimentally found to be unstable can be bracketed in the same way with the computation. The highest density ratio used experimentally which still showed an unperturbed shock and stable shear layer is shown in Figure 5.11. At that condition (the projectile is traveling at 1260 m/s in propane) the density ratio is approximately 13. The perfect gas condition that best approximated the shock profile, stand-off distance and density ratio in the numerical simulation used $\gamma = 1.13$ and $M = 5.5$. The result of that simulation, overlaid onto the experimental result, is shown in Figures 5.15.

Similarly, at the conditions corresponding to Figure 5.14, the projectile is traveling at 2700 m/s in propane and produces a density ratio of approximately 20. Using the criteria outlined above, a simulation with $\gamma = 1.07$ and $M = 10$ corresponds to the experimental data. The result is overlaid on the experimental shadowgraph in Figure 5.16.

The features of the flow in the wake (note the recompression shock) agree well with the experiment in both cases. The distortion of the shock in the high density ratio simulation also matches qualitatively the experiment.

In both of the computations shown in Figures 5.15 and 5.16 the disturbance introduced at the inflow boundary is of the form specified by Equation (5.1), with maximum amplitude of 0.5%, as defined at the beginning of the chapter. Thus, the two figures show that the critical density ratio at which small disturbances cause instability is bracketed by the density ratios (13 and 18, respectively) of these two figures, in both the computation *and* the experiment.

5.4 Stability of shocks in dissociating gases

The instability of shocks in *exothermic* (detonating) processes has been documented (see, *e.g.*, Strehlow [1968] or McVey and Toong [1971]). Is there an equivalent mechanism due to the endothermic nature of dissociating gases which may be responsible for instabilities in shock waves? According to Fickett and Davis [1979], the stability of the shock depends solely on the shape of the Hugoniot curve. In the case of a dissociating gas, the Hugoniot may reach a point at sufficiently high pressure where the slope becomes positive. Indeed, this was observed in normal shocks by Griffiths *et al.* [1975]. Since the flow conditions studied in the experiments presented in this thesis span a region of the Hugoniot curve that has negative slope throughout (even at the normal shock point), this phenomenon is not responsible for any instability observed in the flow. We note again that the critical density ratio at which the instability occurs in the experiments was also bracketed by numerical simulations of a perfect gas where no account of the flow chemistry is included.

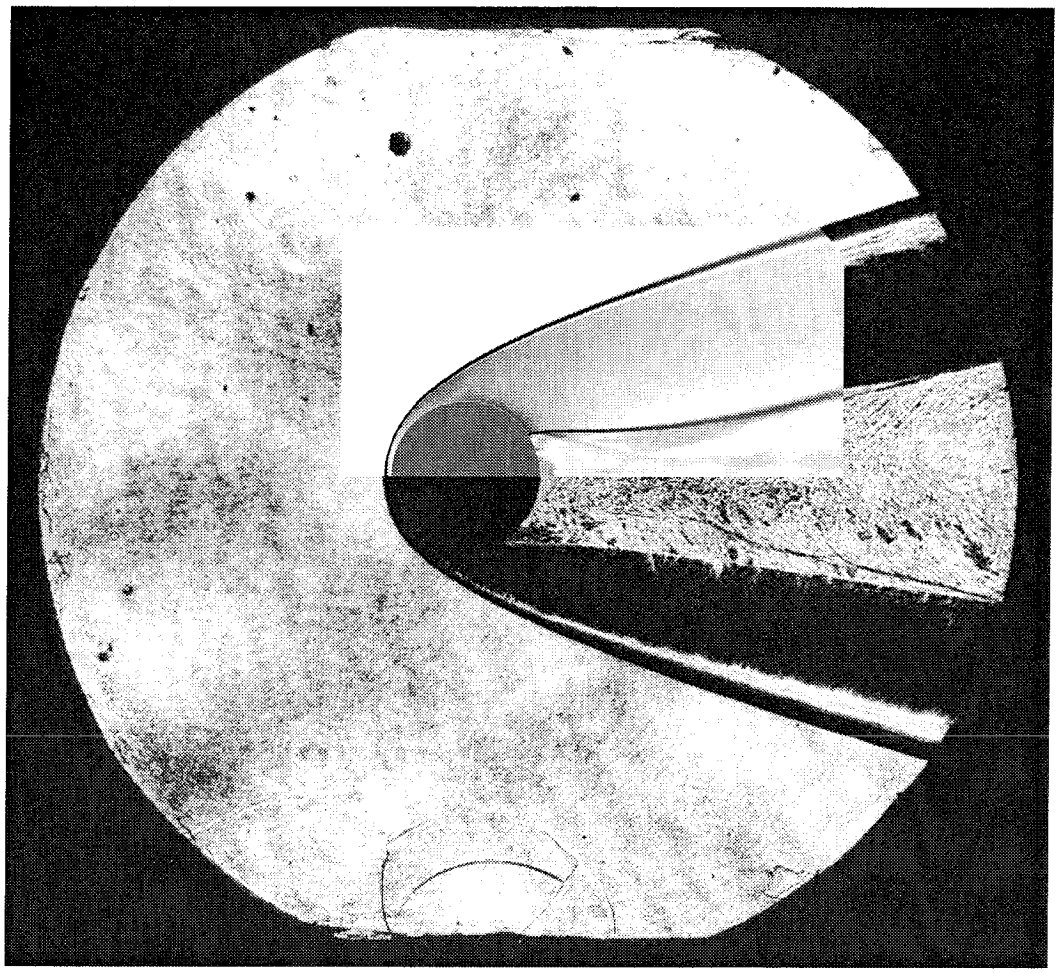

Figure 5.15. Overlay of Figure 5.12 (a) with a simulation of a perfect gas flowing over a sphere at M=5.5 and γ=1.13.

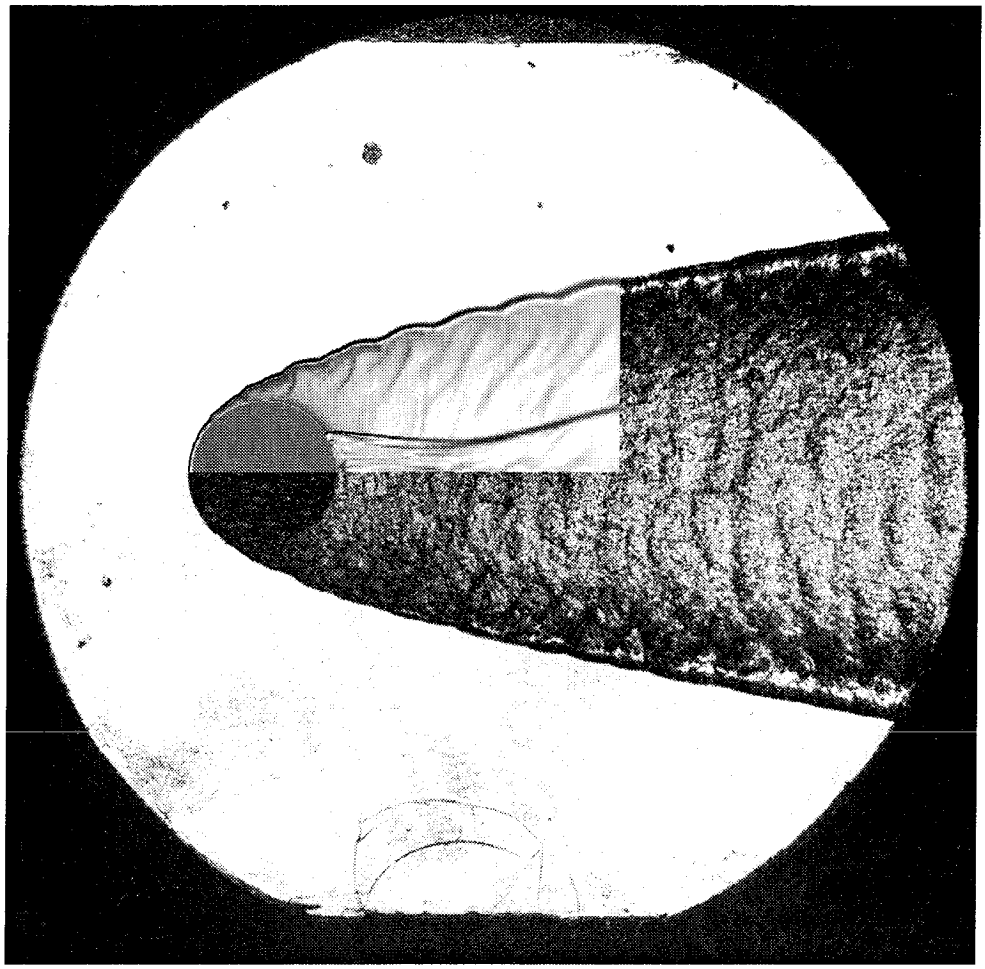

Figure 5.16. Overlay of Figure 5.14 with a simulation of a perfect gas flowing over a sphere at M=10 and γ=1.07.

This page is intentionally blank.

Chapter 6 Conclusion

An instability in the shear layer produced by a curved shock has been observed directly for the first time. The density ratio across the shock has been identified as the most important parameter in determining the overall stability of the shear layer.

Through an experimental program carried out in the T5 Hypervelocity Laboratory, a new technique to visualize streaklines in hypervelocity flows called Sodium Wire Streakline Visualization (SWSV) has been developed and used to observe the flow in the shock layer over a blunt wedge. The results obtained using this technique were not entirely conclusive because the density ratios produced across the shock in the wind tunnel were not sufficiently high for the instability to develop significant structures from the ambient disturbances in the flow.

The preferred wavelength of structures that develop in the shear layer was investigated by numerical simulations of perfect-gas flows. Specifically, the effect of vorticity thickness and of disturbance amplitude and wavelength were studied numerically, and showed that the preferred wavelength is broadly distributed around a value equal to one half of the wedge leading edge, commensurate with the experimental results obtained using SWSV. The numerical study pointed to a flow regime, as the Newtonian limit is approached, where the shock itself breaks down and becomes distorted by the instability.

An experiment aimed at investigating real gas flows near this regime was undertaken in the T5 Light Gas Gun facility. Projectiles were sent into carbon dioxide and propane at speeds up to 2700 m/s. The density ratios that can be reached in such an experiment approach 20. This experiment found that in flows with density ratios across the normal part of the shock exceeding 18, the instability in the shear layer produced by the curved shock causes a significant distortion of the shock, and periodic oscillations develop on its surface. Both the numerical simulations and the experiments bracketed the same critical density ratio at which this transition occurs.

Bibliography

J. D. Anderson. *Hypersonic and High Temperature Gas Dynamics.* McGraw-Hill Book Company, 1989.

A.S. Baryshnikov, A.P. Bedin, V.G. Maslennikov, and G.I. Mishin. Stability of a bow shock. *Soviet Technical Physics Letters*, 5(3):113–114, 1979.

A.P. Bedin. Characteristics of the relaxation instability of shock waves in molecular gases in the example of trifluoriodomethane. *Zhurnal Tekhnicheskoi Fiziki*, 59: 152–155, 1989.

H.W. Behrens. *Flow field and stability of the far wake behind cylinders at hypersonic speeds.* Ph.D. thesis, California Institute of Technology, 1966.

J. Bélanger. *Studies of Mixing and Combustion in Hypervelocity Flows with Hot Hydrogen Injection.* Ph.D. thesis, Graduate Aeronautical Laboratories, California Institute of Technology, Pasadena, California, 1993.

J. Bélanger, M. Kaneshige, and J. E. Shepherd. Detonation initiation by hypervelocity projectiles. In *Proceedings of the 20th International Symposium on Shock Waves*, Pasadena, USA, 1995.

G. Blendstrup, D. Bershader, and P. Langhoff. Recent results of resonant refractivity studies for improved flow visualization. In *Proceedings of the 12th International Symposium on Shock Waves*, Jerusalem, Israel, 1979.

F.G. Blottner, M. Johnson, and M. Ellis. Chemically reacting viscous fow program for multi-component gas mixtures. Technical Report SC-RR-70-754, Sandia Laboratories, Albuquerque, New Mexico, 1971.

G. Candler. *The Computation of Weakly Ionized Hypersonic Flows in Thermo-Chemical Nonequilibrium.* Ph.D. thesis, Stanford University, Stanford, California, 1988.

T.N. Canning, A. Seiff, and C.S. James. Ballistic range technology. Technical Report 138, AGARD, 1970.

S.Y. Chernyavskii, N.N. Baulin, and A.S. Mkrtumov. High-speed flow of a mixture of hydrogen and oxygen over blunt bodies. *Combustion, explosion and shock waves*, 1973.

J.W. Cleary. An experimental and theoretical investigation of the pressure distribution and flow fields of blunted cones at hypersonic mach numbers. Technical Report TN D-2969, NASA Technical Note, 1965.

J.W. Cleary. Effects of angle of attack and nose bluntness on the hypersonic flow over cones. In *AIAA 4th Aerospace Sciences Meeting*, 1966. Paper 66-414.

J.W. Cleary. Effects of angle of attack and bluntness on the shock-layer properties of a 15° cone at a mach number of 10.6. Technical Report TN D-4909, NASA Technical Note, 1968.

W.D. Crozier and W. Hume. High-velocity light-gas gun. *Journal of Applied Physics*, 28(8), 1957.

E. B. Cummings. *Laser-Induced Thermal Acoustics.* Ph.D. thesis, Graduate Aeronautical Laboratories, California Institute of Technology, Pasadena, California, 1995.

L.E. Ericsson. Effect of nose bluntness and cone angle on slender-vehicle transition. *AIAA Journal*, 26(10), 1988.

A.V. Fedorov. Instability of the entropy layer on a blunt flat plate in supersonic flow. *Zhurnal Prikladnoi Mekhaniki i Tekhnicheskoi Fiziki*, 5:63–69, 1990.

W. Fickett and W.C. Davis. *Detonation.* University of California Press, 1979.

T.F. Fric and A. Roshko. Vortical structures in the wake of a transverse jet. *Journal of Fluid Mechanics*, 279, 1994.

P. Germain. *The Boundary Layer on a Sharp Cone in High-Enthalpy Flow.* Ph.D. thesis, Graduate Aeronautical Laboratories, California Institute of Technology, Pasadena, California, 1994.

V.P. Goddard, J.A. MacLaughlin, and F.N.M. Brown. Visual supersonic flow patterns by means of smoke lines. *Journal of the Aero/Space Sciences*, 26:761–762, 1959.

R.W. Griffiths, R.J. Sandeman, and H.G. Hornung. The stability of shock waves in ionizing and dissociating gases. *Journal of Physics D: Applied Physics*, 8:1681–1691, 1975.

W. D. Hayes and R. F. Probstein. *Hypersonic Flow Theory.* Academic Press, New York, 2nd edition, 1966.

H.G. Hornung. 28th lanchester memorial lecture – experimental real-gas hypersonics. *aeronautical journal*, 92(920):379–389, 1988.

H.G. Hornung. Shock layer instability near the newtonian limit of hypervelocity flows. In *13th Australasian Fluid Mechanics Conference*, 1998.

K. Itoh, S. Ueda, T. Kumoro, K. Sato, M. Takahashi, H. Miyajima, and Kanya Koga. Design and construction of HIEST (High Enthalpy Shock Tunnel). In *JSME International Conference on Fluid Engineering*, Tokyo, Japan, 1997.

M. Kaneshige. *Gaseous Detonation Initiation and Stabilization by Hypervelocity Projectiles.* Ph.D. thesis, California Institute of Technology, 1999.

C.G. Lewis. *The effect of an axial flow component on a circular cylinder wake.* Ph.D. thesis, University of California, San Diego, 1993.

M.J. Lighthill. Dynamics of a dissociating gas. part 1: Equilibrium flow. *Journal of Fluid Mechanics*, 2(1):1–32, 1957.

J.A. Lordi, R.E. Mates, and J.R. Moselle. Computer program for the numerical solution of nonequilibrium expansions of reacting gas mixtures. Technical Report NASA CR-472, NASA, 1966.

J. Lukasiewicz. *Experimental Methods of Hypersonics.* Marcel Dekker Inc, New York, 1973.

R.W. MacCormack and G.V. Candler. The solution of the navier-stokes equations using gauss-seidel line relaxation. *Computers and Fluids*, 17(1):135–150, 1989.

H. Mach, F. Rössler, and W. Struth. Messung der Stosswellentemperatur vor einem Geschoss in Tetrachlorkohlenstoffdampf. In *Proceedings of the Sixth International Congress on High-Speed Photography.* Institut Saint-Louis, France, 1962.

L. Mach. Uber die Sichtbarmachung von Luftstromlinien. *Z. Luftschiffahrt Phys. Atm.*, 6:129–139, 1896.

M.K. McIntosh. A computer program for the numerical calculation of equilibrium and perfect gas conditions in shock tunnels. Technical Note CPD 169, Australian Defense Scientific Service, 1969.

J.B. McVey and T.Y. Toong. Mechanism of instabilities of exothermic hypersonic blunt-body flows. *Combustion Science and Technology*, 1971.

W. Merzkirch. *Flow visualization.* Academic Press, 1974.

G.I. Mishin and N.P. Mende. *Aerophysical Studies of Supersonic Flows [in Russian].* Nauka, 1967.

W.H. Press, S.A. Teukolsky, W.T. Vetterling, and B.P. Flannery. *Numerical Recipes in FORTRAN: The Art of Scientific Computing.* Cambridge University Press, 2nd edition, 1992.

J.J. Quirk. A computational facility (for cfd modeling). In *VKI 29th CFD Lecture Series*, Brussels, 1998. von Karman Institute for Fluid Dynamics.

Lord Rayleigh. On the stability, or instability, of certain fluid motions. *Proceedings of the London Mathematical Society*, 11:57–70, 1880.

W.C. Reynolds. The element potential method for chemical equilibrium analysis: Implementation in the interactive program stanjan. Technical report, Department of Mechanical Engineering, Stanford University, 1986.

A. Roshko. Instability and turbulence in shear flows. *Theoretical and Applied Mechanics*, 1992.

B. Rousset. Calibration and study of the contoured nozzle of the t5 free-piston hypervelocity shock tunnel. Engineer's Thesis, 1995. Graduate Aeronautical Laboratories, California Institute of Technology.

S. R. Sanderson. *Shock Wave Interaction in Hypervelocity Flow.* Ph.D. thesis, Graduate Aeronautical Laboratories, California Institute of Technology, Pasadena, California, 1995.

E.J. Softley. Transition of the hypersonic boundary layer on a cone: Part II - experiments at M=10 and more on blunt cone transition. Technical report, General Electric Space Sciences Laboratory, 1968.

R.J. Stalker. Mt-44. Technical Report MT-44, National Research Council of Canada, 1961.

K.F. Stetson. Effect of bluntness and angle of attack on boundary layer transition on cones and biconic configurations. In *17th Aerospace Sciences Meeting*, New Orleans, LA, 1979. AIAA.

K.F. Stetson, E.R. Thompson, Donaldson J.C., and Siler L.G. Laminar boundary layer stability experiments on a cone at Mach 8, Part 2: Blunt cone. In *AIAA 22nd Aerospace Sciences Meeting*, 1984.

R.A. Strehlow. *Fundamentals of Combustion.* International Texbok Company, 1968.

A.P. Thorne. *Spectrophysics.* Chapman and Hall, 1988.

C. Truesdell. On curved shocks in steady plane flows of an ideal fluid. *Journal of Aeronautical Sciences*, 19:826–828, 1952.

C.W. Van Atta. Experiments on vortex shedding from yawed circular cylinders. *AIAA Journal*, 6(5), 1968.

A. Vazsonyi. On rotational gas flows. *Brown University - Quaterly Applied Mathematics*, 3(1):29–37, 1945.

C.-Y. Wen. *Hypervelocity Flow Over Spheres.* Ph.D. thesis, Graduate Aeronautical Laboratories, California Institute of Technology, Pasadena, California, 1994.

C.-Y. Wen and H. G. Hornung. Non-equilibrium dissociating flow over spheres. *Journal of Fluid Mechanics*, 299, 1995.

F. M. White. *Viscous Fluid Flow.* McGraw-Hill, Inc., 2nd edition, 1991.

C.H.K. Williamson. Vortex dynamics in the cylinder wake. *Annual Review of Fluid Mechanics*, 28, 477–539 1996.

Appendix A T5 tunnel flow

This appendix presents data pertinent to the work done with the hemicylindrically-blunted wedge used in the T5 tunnel flow study.

Included here are the T5 operating conditions, test section free-stream flow conditions and diagnostics used for each shot. The stagnation condiditons were computed using ESTC (McIntosh [1969]; the free-stream conditions were computed using NENZF (Lordi *et al.* [1966])).

The surface measurements (average heat transfer and pressure) recorded during the T5 tunnel flow experiments are not used in this thesis and are therefore not included here. These may be found in a separate Graduate Aeronautical Laboratories, California Institute Of Technology (GALCIT) report.

A.1 Test conditions

Table A.1: T5 run conditions for every shot in standard tunnel operation

Series	Shot #	ST Gas	Nom. Cond.	P_{2R} (psi)	P_{CT} (kPa)	% He	P_{ST} (kPa)	Throat (mm)	Nozzle cTrd cNcl	P_0 (MPa)	h_0 (MJ/kg)
1	1326	N_2	2	600	95	100	20	30	T	26.2	19
1	1327	N_2	2	600	95	100	20	30	T	25.8	20.5
1	1328	N_2	1	450	80	90	35	30	T	19.4	10.8
1	1329	N_2	1	450	80	90	35	30	T	19.1	10.2
1	1330	N_2	1	450	80	90	35	30	T	18.9	9.9
1	1331	N_2	1	450	80	90	35	30	T	19.5	10.3
1	1332	N_2	1	450	80	90	35	30	T	19.5	10.3
1	1333	N_2	1	450	80	90	35	30	T	18.9	10.2
1	1334	N_2	1	450	80	90	35	30	T	18.4	10.1
1	1335	N_2	1	450	80	90	35	30	T	19	9.8
1	1336	N_2	1	450	80	90	35	30	T	19.5	10.3
1	1337	N_2	1	450	80	90	35	30	T	18.5	10.2
1	1338	N_2	1	450	80	90	35	30	T	19.4	10.39
1	1339	N_2	1	450	80	90	35	30	T	19.3	10.38

Table A.1: (continued)

Series	Shot #	ST Gas	Nom. Cond.	P_{2R} (psi)	P_{CT} (kPa)	% He	P_{ST} (kPa)	Throat (mm)	Nozzle cTrd cNcl	P_0 (MPa)	h_0 (MJ/kg)
1	1340	N_2	1	450	80	90	35	30	T	19.4	10.4
1	1341	N_2	1	450	80	90	35	30	T	19.3	10.9
1	1342	N_2	1	450	80	90	35	30	T	20.1	10.55
1	1343	N_2	1	450	80	90	35	30	T	19.7	10.59
1	1344	N_2	1	450	80	90	35	30	T	19.3	10.63
1	1345	N_2	2	600	95	100	20	30	T	26.4	19.5
1	1346	N_2	2	600	95	100	20	30	T	26.8	20
1	1347	N_2	2	600	95	100	20	30	T	26.4	20.34
1	1348	N_2	2	600	95	100	20	30	T	26.3	20.83
1	1349	N_2	2	600	95	100	20	30	T	26.3	21.1
1	1350	N_2	1	450	80	90	35	30	N	20.1	10.6
1	1351	N_2	2	600	95	100	20	30	N	25.2	19.7
1	1352	N_2	1	450	80	90	35	30	N	19.2	10.4
1	1354	N_2	3	280	46	40	75	30	N	14.1	4.5
1	1355	N_2	3	280	46	40	75	30	N	12.8	3.85
1	1356	N_2	3	280	46	40	75	30	N	13.1	4
1	1357	N_2	1	450	80	90	35	30	N	19.8	10.7
1	1358	N_2	2	600	95	100	20	30	N	27.2	20
1	1359	CO_2	NA	800	93	93	37.5	30	N	40.4	10.22
1	1360	N_2	3	280	46	40	75	30	N	12.9	4.1
1	1361	N_2	2	600	95	100	20	30	N	27	20.8
1	1362	N_2	1	450	80	90	35	30	N	19.4	10.4
1	1363	N_2	3	280	46	40	75	30	N	12.2	3.8
1	1364	CO_2	NA	800	93	93	25	30	N	39	12.81
1	1365	N_2	1	450	80	90	35	30	N	19	9.4
1	1366	N_2	3	280	46	40	75	30	N	12.1	3.7
1	1367	N_2	2	600	95	100	20	30	N	26.6	20
1	1368	CO_2	NA	800	93	93	32	30	N	40.9	11.3
2	1607	N_2	1	450	80	90	35	30	N	20	9.3
2	1608	N_2	1	450	80	90	35	30	N	NA	NA
2	1609	N_2	1	480	80	90	35	30	N	22.1	11.56
2	1610	N_2	3	300	46	40	75	30	N	14.3	4.6
2	1611	N_2	2	600	95	100	20	30	N	26	19.8
2	1612	N_2	3	300	46	40	75	30	N	14.5	4.55
2	1613	N_2	1	480	80	90	35	30	N	23	12.29
2	1614	N_2	2	600	95	100	20	30	N	27.8	20.52
2	1615	N_2	3	300	46	40	75	30	N	14.2	4.64
2	1616	N_2	3	350	50	40	85	30	N	17.7	4.7
2	1617	N_2	3	300	46	40	75	30	N	12.4	4.32

Table A.1: (continued)

Series	Shot #	ST Gas	Nom. Cond.	P_{2R} (psi)	P_{CT} (kPa)	% He	P_{ST} (kPa)	Throat (mm)	Nozzle cTrd cNcl	P_0 (MPa)	h_0 (MJ/kg)
2	1618	N_2	2	600	95	100	20	30	N	30.8	20.61
2	1619	N_2	2	600	95	100	20	30	N	27.9	20.28
2	1620	N_2	3	300	46	40	75	30	N	14.6	4.63
2	1621	N_2	1	480	80	90	35	30	N	23	12.2
2	1622	CO_2	NA	550	74	84	40	30	N	28.7	6.81
3	1675	N_2	1	480	80	90	35	30	N	22.8	14.4
3	1676	N_2	1	480	80	90	35	30	N	21.6	12
3	1677	N_2	1	480	80	90	35	30	N	20.7	10.4
3	1678	N_2	1	480	80	90	35	30	N	20.1	10.63
3	1679	N_2	1	480	80	90	35	30	N	21	11.1
3	1680	N_2	1	480	80	90	35	30	N	21.4	11.31
3	1681	N_2	1	480	80	90	35	30	N	21.2	11.2
3	1682	N_2	1	480	80	90	35	30	N	22.1	11.48
3	1683	N_2	1	480	80	90	35	30	N	22	11.38
3	1684	N_2	1	480	80	90	35	30	N	22	11.47
3	1685	N_2	1	480	80	90	35	30	N	21.8	11.64
3	1686	N_2	1	480	80	90	35	30	N	22.2	11.85
3	1687	N_2	1	480	80	90	30	30	N	23	12.3
3	1688	N_2	1	480	80	90	35	30	N	22.7	12.5
3	1689	N_2	3	350	50	40	85	30	N	18	4.6
3	1690	N_2	3	320	50	40	85	30	N	14.1	4.3
3	1691	N_2	3	300	46	40	75	30	N	14.6	4.56
3	1692	N_2	3	300	46	40	75	30	N	14.8	4.6
3	1693	N_2	3	300	46	40	90	30	N	14.9	4.22
3	1694	N_2	3	300	46	40	100	30	N	15.1	4
3	1695	N_2	3	300	46	40	100	30	N	15.7	3.85
3	1696	N_2	3	300	46	40	100	30	N	15.8	3.9
3	1697	N_2	1	480	80	90	35	30	N	21.3	12.2
3	1698	N_2	2	600	95	100	20	30	N	27.3	20.2
3	1699	N_2	2	600	95	100	20	30	N	27.2	21.2
3	1700	N_2	2	600	95	100	20	30	N	27.4	22.3
3	1701	N_2	2	600	95	100	20	30	N	26.9	22
3	1702	N_2	2	600	95	100	20	30	N	26.1	21.1
3	1703	N_2	2	600	95	100	20	30	N	27.4	22.1
3	1704	N_2	2	600	95	100	20	30	N	27	21.7
3	1705	N_2	2	600	95	100	20	30	N	27.8	21.3
3	1706	CO_2	NA	550	74	84	40	30	N	27.8	7.11
3	1707	CO_2	NA	550	74	84	30	30	N	25.7	8.39
3	1708	N_2	1	480	80	90	35	30	N	22	12.07

Table A.1: (continued)

Series	Shot #	ST Gas	Nom. Cond.	P_{2R} (psi)	P_{CT} (kPa)	% He	P_{ST} (kPa)	Throat (mm)	Nozzle cTrd cNcl	P_0 (MPa)	h_0 (MJ/kg)
3	1709	CO_2	NA	600	95	100	15	30	N	27.2	17.2
3	1710	N_2	1	480	80	90	35	30	N	21.5	11.72
3	1711	N_2	1	480	80	90	35	30	N	22.1	11.34
3	1712	N_2	1	480	80	90	35	30	N	21.9	11.47
3	1713	N_2	1	480	80	90	35	30	N	22.6	11.74
3	1714	N_2	1	480	80	90	35	30	N	21.7	11.74
3	1715	CO_2	NA	480	80	90	23	30	N	21.7	9.82
3	1716	CO_2	NA	540	95	100	13	30	N	23.4	17.05
3	1717	CO_2	NA	540	95	100	11.5	30	N	22.9	18.52
3	1718	N_2	2	600	95	100	20	30	N	27.2	21.7
3	1719	N_2	2	600	95	100	20	30	N	27.5	21.5
3	1720	N_2	2	600	95	100	20	30	N	26.6	21.95
3	1721	N_2	2	600	95	100	20	30	N	26.6	21.5
3	1722	N_2	2	600	95	100	20	30	N	27.4	21.47
3	1723	N_2	2	600	95	100	20	30	N	27.2	21.3
3	1724	N_2	2	600	95	100	20	30	N	27.5	21.85
5	1855	N_2	1	480	80	90	35	15	N	20.5	10.98
5	1856	N_2	1	480	80	90	35	30	N	20	10.53
5	1857	N_2	1	480	80	90	35	30	N	20.3	10.83
5	1858	N_2	1	480	80	90	35	30	N	20.4	10.84
5	1859	N_2	1	480	80	90	35	30	N	19.5	10.91
5	1860	N_2	2	600	95	100	20	30	N	23.7	19.06
5	1861	N_2	2	600	95	100	20	30	N	23.5	18.39
5	1862	N_2	2	600	95	100	20	30	N	23.8	19.76
5	1863	N_2	2	600	95	100	20	30	N	23.8	19.76
5	1864	N_2	1	480	80	90	35	30	N	19.7	10.85
5	1865	N_2	3	300	46	40	100	30	N	NA	NA
5	1866	N_2	3	300	46	40	100	30	N	13.1	4.19
5	1867	N_2	2	600	95	100	30	30	N	25.4	15.7
5	1868	C_3H_8	NA	480	80	10	25	30	N	19.6	10.5
5	1869	C_3H_8	NA	400	43	21	100	30	N	26.4	2.28
5	1870	C_3H_8	NA	400	43	21	50	30	N	22.9	3.2
5	1871	C_3H_8	NA	400	43	21	100	15	N	29.8	2.3
5	1872	CO_2	NA	400	43	21	100	15	N	27.2	2.77
5	1873	CO_2	NA	400	43	21	100	15	N	25.1	2.73
5	1874	C_3H_8	NA	400	43	21	100	15	N	29.5	2.3
5	1875	N_2	3	300	46	40	100	30	N	13.9	3.54
5	1876	N_2	3	300	46	40	100	30	N	13.3	3.59
5	1877	CO_2	NA	300	46	40	65	30	N	16.1	3.4

Table A.1: (continued)

Series	Shot #	ST Gas	Nom. Cond.	P_{2R} (psi)	P_{CT} (kPa)	% He	P_{ST} (kPa)	Throat (mm)	Nozzle cTrd cNcl	P_0 (MPa)	h_0 (MJ/kg)
5	1878	N_2	3	300	46	40	100	30	N	12.5	3.26
5	1879	CO_2	NA	300	46	40	65	30	N	15.5	2.7
5	1880	N_2	3	300	46	40	100	30	N	12.4	3.31
5	1881	CO_2	NA	300	46	40	65	30	N	15.1	2.66
5	1882	CO_2	NA	300	46	40	65	15	N	15	2.66
5	1883	N_2	3	300	46	40	100	15	N	14.5	3.62

Abbreviations used in Table A.1:

cTrd (T): Contoured nozzle

cNcl (N): Conical nozzle

Table A.2: T5 test section data and diagnostics used

Shot #	Cond (N_2)	P_∞ (kPa)	T_∞ (K)	ρ_∞ (kg/m^3)	U_∞ (m/s)	M_∞	wire ϕ (mils)	LE rad. (in)	SWSV result	Q_s (ms)	nzl dist (cm)
1326	2	14.1	2857	0.0160	5370	5.17	24	1.375	BX	1.200	12.20
1327	2	14.2	3008	0.0151	5487	5.14	24	1.375	BX	1.200	17.40
1328	1	7.79	1450	0.0180	4264	5.68	24	1.375	NT	1.400	16.60
1329	1	7.51	1378	0.0183	4183	5.71	24	1.375	NL	1.400	16.60
1330	1	7.35	1335	0.0185	4135	5.73	24	1.375	NL	1.000	16.60
1331	1	7.68	1390	0.0186	4190	5.71	22	1.375	NL	1.000	14.20
1332	1	7.68	1386	0.0186	4192	5.71	22	1.375	NL	1.700	14.20
1333	1	7.4	1361	0.0183	4160	5.72	22	1.375	NL	0.500	9.00
1334	1	7.21	1365	0.0177	4168	5.71	22	1.375	NL	1.000	9.00
1335	1	7.29	1290	0.0190	4081	5.76	22	1.375	NL	1.000	9.00
1336	1	7.65	1372	0.0188	4177	5.72	22	1.375	NL	1.500	9.00
1337	1	7.23	1353	0.0180	4155	5.72	22	1.375	C	1.500	12.70
1338	1	7.64	1384	0.0186	4190	5.71	22	1.375	NL	2.000	12.60
1339	1	7.597	1382	0.0185	4187	5.71	24	1.375	A	1.500	12.60
1340	1	7.64	1384	0.0186	4190	5.71	24	1.375	NL	1.500	12.60
1341	1	7.77	1469	0.0178	4278	5.67	24	1.375	BX	1.500	12.70
1342	1	7.969	1411	0.0190	4219	5.7	24	1.375	NT	1.500	12.70
1343	1	7.83	1418	0.0185	4226	5.69	24	1.375	NT	1.500	12.60
1344	1	7.68	1424	0.0181	4232	5.69	22	1.375	NT	1.200	12.50
1345	2	14.3	2905	0.0159	5407	5.16	22	1.375	B	0.900	13.40
1346	2	14.7	2978	0.0159	5457	5.14	22	1.375	NL	0.900	13.20
1347	2	14.52	2997	0.0155	5474	5.14	24	1.375	NL	1.000	13.10
1348	2	14.58	3056	0.0152	5520	5.13	24	1.375	NL	1.000	13.20
1349	2	14.7	3089	0.0151	5544	5.12	24	1.375	NL	1.000	13.10
1350	1	6.52	1385	0.0159	4291	5.83	HOLO	1.375	NA	1.000	15.90
1351	2	11	2810	0.0127	5468	5.17	HOLO	1.375	NA	1.000	16.90
1352	1	6.2	1355	0.0154	4256	5.84	HOLO	1.375	NA	1.000	15.90
1354	3	4.6	532	0.0291	2863	6.12	HOLO	1.375	NA	1.000	14.80
1355	3	7.56	530	0.0481	2630	5.63	HOLO	1.375	NA	1.000	14.80
1356	3	5.94	517	0.0387	2701	5.85	HOLO	1.375	NA	1.400	-2.10
1357	1	9.22	1519	0.0204	4264	5.54	HOLO	1.375	NA	1.000	-1.10
1358	2	17.04	3130	0.0176	5464	4.9	HOLO	1.375	NA	1.000	0.00
1359	NA	54.3	2518	0.0976	3325	4.16	HOLO	1.375	NA	1.000	0.90
1360	3	5.754	527.3	0.0368	2730	5.86	HOLO	1.375	NA	NA	4.00
1361	2	15.1	3136	0.0155	5553	4.95	HOLO	1.375	NA	1.000	5.80
1362	1	7.81	1420	0.0185	4224	5.67	HOLO	1.375	NA	1.000	5.00
1363	3	7.28	524	0.0468	2614	5.63	HOLO	1.375	NA	1.000	4.00
1364	NA	10.21	2666	0.0170	3947	4.87	HOLO	1.375	NA	1.000	6.50
1365	1	6.83	1261	0.0183	3975	5.76	HOLO	1.375	NA	1.000	9.30
1366	3	7.25	521.3	0.0469	2606	5.62	HOLO	1.375	NA	1.000	8.10
1367	2	13.28	2961	0.0145	5493	5.06	HOLO	1.375	NA	1.000	10.70

Table A.2: (continued)

Shot #	Cond (N_2)	P_∞ (kPa)	T_∞ (K)	ρ_∞ (kg/m3)	U_∞ (m/s)	M_∞	wire ϕ (mils)	LE rad. (in)	SWSV result	Q_s (ms)	nzl dist (cm)
1368	NA	47.16	2570	0.0802	3492	4.24	HOLO	1.375	NA	1.000	11.70
1607	1	6.63	1026	0.0213	3856	5.96	20	0.750	NT	NA	8.20
1608	1	NA	NA	NA	NA	NA	HOLO	0.750	NA	NA	NA
1609	1	8.92	1625	0.0184	4454	5.6	HOLO	0.750	NA	1.500	7.60
1610	3	4.18	509	0.0277	2852	6.22	HOLO	0.750	NA	1.500	8.40
1611	2	13.1	2922	0.0140	5458	5.06	HOLO	0.750	NA	1.500	9.90
1612	3	4.04	496	0.0275	2840	6.3	HOLO	0.750	NA	1.500	10.40
1613	1	8.76	1673	0.0176	4533	5.62	HOLO	0.750	NA	1.500	11.30
1614	2	13.76	3017	0.0150	5539	5.05	HOLO	0.750	NA	1.500	11.60
1615	3	4.17	514	0.0273	2863	6.22	HOLO	0.750	NA	1.500	8.30
1616	3	5.22	523	0.0336	2882	6.2	HOLO	SHARP	NA	1.500	8.30
1617	3	3.57	3094	0.0256	2766	6.3	HOLO	SHARP	NA	1.500	8.20
1618	2	17.55	3157	0.0180	5535	4.94	HOLO	SHARP	NA	1.500	5.10
1619	2	15.1	3049	0.0160	5500	5	HOLO	0.750	NA	1.400	7.00
1620	3	4.54	522	0.0290	2857	6.16	HOLO	0.750	NA	1.400	5.60
1621	1	9.63	1693	0.0190	4505	5.55	HOLO	0.750	NA	1.400	6.50
1622	NA	13.96	895	0.0700	2638	5.23	HOLO	0.750	NA	1.450	6.70
1675	1	9.86	2090	0.0157	4860	5.39	20	sharp	S	1.000	9.88
1676	1	8.43	1675	0.0169	4522	5.6	20	sharp	S	1.000	10.10
1677	1	7.43	1362	0.0184	4213	5.76	20	sharp	S	1.000	10.14
1678	1	7.34	1398	0.0177	4249	5.74	41	sharp	S	1.000	9.78
1679	1	8.08	1483	0.0182	4326	5.68	41	sharp	S	1.000	8.64
1680	1	8.013	1512	0.0178	4368	5.68	80	sharp	S	1.000	10.03
1681	1	7.982	1525	0.0176	4380	5.67	80	sharp	S	1.000	9.93
1682	1	8.34	1541	0.0182	4397	5.67	20	sharp	S	1.000	9.98
1683	1	8.29	1525	0.0183	4380	5.67	20	sharp	S	1.000	9.85
1684	1	8.25	1537	0.0180	4396	5.68	20	0.750	NT	1.000	10.27
1685	1	8.063	1559	0.0174	4428	5.68	41	0.750	A	1.000	11.38
1686	1	8.278	1594	0.0174	4461	5.66	80	0.750	C	1.000	11.42
1687	1	8.805	1675	0.0177	4533	5.61	20	0.750	NT	1.000	11.09
1688	1	8.739	1707	0.0172	4563	5.6	41	0.750	B	1.000	11.26
1689	3	5.11	535.4	0.0322	2925	6.23	41	0.750	NT	1.010	10.36
1690	3	6.263	530	0.0398	2737	5.86	20	0.750	BX	1.010	9.84
1691	3	4.84	522	0.0312	2833	6.11	NA	0.750	NT	1.010	9.95
1692	3	4.872	526	0.0312	2844	6.11	41	0.750	NT	1.000	10.32
1693	3	6.72	521	0.0435	2711	5.86	41	0.750	NT	0.995	10.90
1694	3	8.95	528	0.0571	2625	5.63	41	0.750	NT	1.085	9.69
1695	3	9.36	525	0.0601	2615	5.63	20	0.750	NT	1.090	9.93
1696	3	7.297	506.4	0.0486	2671	5.84	41	0.750	NT	1.240	10.68
1697	1	8.165	1662	0.0165	4518	5.61	41	0.750	B	1.235	10.94
1698	2	13.53	2975	0.0147	5506	5.06	41	0.750	NT	1.200	11.22

Table A.2: (continued)

Shot #	Cond (N_2)	P_∞ (kPa)	T_∞ (K)	ρ_∞ (kg/m3)	U_∞ (m/s)	M_∞	wire ϕ (mils)	LE rad. (in)	SWSV result	Q_s (ms)	nzl dist (cm)
1699	2	13.64	3093	0.0141	5599	5.02	41	0.750	NT	1.040	11.45
1700	2	13.92	3226	0.0137	5705	5	20	0.750	C	0.995	11.65
1701	2	13.57	3192	0.0135	5684	5	80	0.750	NL	1.000	11.82
1702	2	12.99	3088	0.0134	5609	5.03	41	0.750	C	1.000	11.81
1703	2	13.83	3193	0.0138	5681	5	20	0.750	NT	1.240	11.83
1704	2	13.64	3152	0.0138	5646	5	20	0.750	NT	0.995	11.47
1705	2	13.82	3107	0.0143	5614	5.02	20	0.750	A	0.995	12.02
1706	NA	22.64	2177	0.0537	2958	4.295	41	0.750	NT	0.995	11.27
1707	NA	20.53	2415	0.0422	3154	4.32	20	0.750	NL	0.935	11.74
1708	1	8.219	1631	0.0169	4499	5.6	20	0.750	C	1.000	11.86
1709	NA	18.54	2998	0.0237	4119	4.43	20	0.750	NT	0.995	12.16
1710	1	7.94	1571	0.0170	4440	5.671	20	0.750	A	0.995	11.61
1711	1	8.017	1505	0.0179	4378	5.71	20	0.750	B	1.005	11.62
1712	1	7.98	1526	0.0176	4399	5.7	41	0.750	C	1.000	11.70
1713	1	8.31	1572	0.0178	4446	5.7	20	0.750	NL	1.000	11.87
1714	1	7.99	1573	0.0171	4440	5.67	20	0.750	A	0.995	11.82
1715	NA	11.68	2512	0.0221	3413	4.49	41	0.750	NT	1.000	11.91
1716	NA	14.27	2956	0.0186	4114	4.47	20	0.750	NT	0.995	12.20
1717	NA	7.9	2903	0.0103	4373	4.76	41	0.750	NT	1.000	12.39
1718	2	14.37	3189	0.0144	5642	4.97	20	1.375	NT	NA	9.28
1719	2	14.55	3168	0.0147	5622	4.98	20	1.375	NT	0.995	9.06
1720	2	14.04	3202	0.0139	5660	4.971	20	1.375	NT	1.000	9.43
1721	2	13.97	3169	0.0141	5634	4.98	41	1.375	NT	1.000	9.47
1722	2	14.3	3153	0.0145	5621	4.99	41	1.375	NT	1.000	9.72
1723	2	14.28	3154	0.0145	5618	4.98	80	1.375	NL	0.834	9.39
1724	2	14.43	3223	0.0142	5675	4.97	41	1.375	NT	0.840	9.91
1855	1	0.972	868	0.0038	4462	7.56	20	2.500	NT	NA	18.00
1856	1	6.05	1321	0.0154	4248	5.9	20	2.500	BX	NA	19.00
1857	1	6.2	1367	0.0152	4300	5.88	20	2.500	NT	1.000	19.30
1858	1	6.91	1404	0.0166	4293	5.79	20	2.500	NT	0.982	13.92
1859	1	6.62	1416	0.0157	4305	5.78	20	2.500	NL	0.965	14.00
1860	2	10.65	2733	0.0126	5390	5.17	41	2.500	NL	0.960	14.60
1861	2	10.4	2640	0.0128	5320	5.21	20	2.500	C	0.965	14.65
1862	2	11.62	2869	0.1310	5448	5.09	41	2.500	NT	0.960	11.15
1863	2	10.94	2831	0.0125	5458	5.13	41	2.500	NL	1.005	14.18
1864	1	6.66	1405	0.0159	4295	5.8	41	2.500	A	NA	14.10
1865	3	NA	NA	NA	NA	NA	41	2.500	BX	NA	NA
1866	3	3.37	440	0.0260	2730	6.4	41	2.500	NT	0.912	12.95
1867	2	10.37	2243	0.0154	5024	5.37	41	2.500	B	0.812	14.90
1868	NA	NA	NA	NA	NA	NA	NA	2.500	NA	0.812	14.54
1869	NA	NA	NA	NA	NA	NA	NA	2.500	NA	0.812	14.54

Table A.2: (continued)

Shot #	Cond (N_2)	P_∞ (kPa)	T_∞ (K)	ρ_∞ (kg/m3)	U_∞ (m/s)	M_∞	wire ϕ (mils)	LE rad. (in)	SWSV result	Q_s (ms)	nzl dist (cm)
1870	NA	NA	NA	NA	NA	NA	NA	2.500	NA	0.915	14.17
1871	NA	NA	NA	NA	NA	NA	NA	2.500	NA	0.910	13.87
1872	NA	1.86	394	0.0249	2091	6.61	NA	2.500	NA	0.910	14.00
1873	NA	1.74	389	0.0236	2079	6.62	NA	2.500	NA	1.820	13.50
1874	NA	NA	NA	NA	NA	NA	NA	2.500	NA	1.820	14.10
1875	3	3.74	369	0.0342	2516	6.43	HOLO	0.750	NA	1.215	8.70
1876	3	3.57	373	0.0322	2529	6.43	HOLO	0.750	NA	1.715	9.00
1877	NA	8.11	715	0.0589	2123	5.08	HOLO	0.750	NA	1.715	9.00
1878	3	3.65	342	0.0360	2410	6.4	HOLO	0.750	NA	1.715	4.00
1879	NA	8.52	622	0.0720	1967	5.05	HOLO	0.750	NA	1.720	3.80
1880	3	3.66	349	0.0350	2426	6.4	HOLO	0.750	NA	1.715	3.70
1881	NA	8.27	614	0.0709	1958	5.06	HOLO	0.750	NA	1.715	3.90
1882	NA	1.24	392	0.0166	2047	6.48	HOLO	0.750	NA	1.715	4.10
1883	3	0.63	224	0.0095	2602	8.52	HOLO	0.750	NA	1.715	1.90

Abbreviations used in Table A.2:

Q_s: Time of laser Q-switch, in miliseconds, with respect to beginning of pressure rise in reservoir.

nzl dist: Distance between nozzle exit plane and leading edge of model, in centimeters.

Comments specific to Sodium Wire Streakline Visualization results:

A,B,C: Category of the data (see Chapter 4)

BX: Bad eXposure; no visible streak

NL: No favored wavelength (λ) detectable

NT: No Trace

S: Sharp leading edge used

TF: Too Faint

X: broken salt crystal

NA: Not Applicable

Appendix B T5 Light Gas Gun

This appendix includes laboratory data pertinent to the work done with the T5 Light Gas Gun in the study of flows at high density ratios. Refer to Chapter 3, Section 3.4 for a description of the setup and of the various timing stations.

B.1 Timing data

Table B.1: T5 Light Gas Gun raw data

Shot #:	1841	1843	1844	1845	1846	1848	1849	1850	1853	1854
Gas:	CO_2	CO_2	CO_2	CO_2	CO_2	C_3H_8	C_3H_8	C_3H_8	CO_2	C_3H_8
DAS data:										
t_{bw} (ms)	0.984	0.792	0.988	0.976	0.800	0.814	x	0.826	0.800	1.692
t_{L1} (ms)	1.460	1.176	1.526	1.476	1.250	1.220	1.480	1.224	1.206	2.556
t_{P1} (ms)	1.226	1.306	1.684	1.634	1.400	1.302	x	1.392	1.342	2.786
t_{P2} (ms)	1.708	1.378	1.776	1.734	1.482	1.396	1.750	1.474	1.424	2.960
t_{L2} (ms)	1.612	1.298	1.662	1.628	1.380	1.348	1.566	1.352	1.326	2.824
t_{P3} (ms)	1.810	1.460	1.872	1.840	1.570	1.468	1.856	1.556	1.506	3.140
t_{L3} (ms)	1.696	1.366	1.742	1.716	1.454	1.424	1.716	1.422	1.400	2.976
t_{Qs} (ms)	1.698	x	1.764	1.736	1.474	1.446	1.752	1.442	1.422	2.998
TEK data:										
t_{pexit} (ms)	0.000	0.000	0.000	0.000	0.000	0.000	0.000	0.000	0.000	0.000
t_{bw} (ms)	x	0.776	0.992	0.992	0.808	0.808	0.984	0.816	0.800	1.700
t_{Qs} (ms)	x	1.392	1.776	1.744	1.472	1.448	1.752	1.440	1.432	3.000
delay(L3-Qs) (ms)	0.0000	0.0185	0.0185	0.0185	0.0185	0.0185	0.0185	0.0185	0.0185	0.0185
$t_{L3}(ms)$	x	1.3735	1.7575	1.7255	1.4535	1.4295	1.7335	1.4215	1.4135	2.9815
SPEEDS:										
DAS: (m/s)										
p1-p2	445	2976	2329	2143	2613	2280	x	2613	2613	1232
p2-p3	2101	2613	2232	2022	2435	2976	2022	2613	2613	1191
p1-p3	734	2783	2280	2081	2521	2582	x	2613	2613	1211
L1-L2	2172	2707	2428	2172	2540	2580	3840	2580	2752	1232
L2-L3	2249	2778	2361	2147	2553	2486	1259	2699	2553	1243
L1-L3	2200	2732	2403	2163	2545	2545	2200	2622	2676	1236

Table B.1: (continued)

	1841	1843	1844	1845	1846	1848	1849	1850	1853	1854
Gas:	CO_2	CO_2	CO_2	CO_2	CO_2	C_3H_8	C_3H_8	C_3H_8	CO_2	C_3H_8
BW-L3	2289	2840	2162	2203	2492	2672	x	2735	2717	1269
TEK: (m/s)										
BW-L3	x	2728	2146	2221	2525	2658	2179	2696	2665	1271
U_{ave} (m/s)	**2228**	**2746**	**2397**	**2196**	**2534**	**2614**	**2183**	**2677**	**2670**	**1258**
U_σ (m/s)	52	43	34	31	11	69	9	50	57	18
STANJAN (equi.):										
Cp (kJ/kg·K)	1.671	2.686	1.973	1.636	2.248	4.433	4.038	4.786	2.507	5.645
T_2 (K)	2207	2834	2447	2170	2612	1302	1077	1103	2747	472
P_2 (MPa)	8.02	12.4	9.47	7.819	10.62	11.58	8.25	12.25	11.67	2.72
v_2 (m^3/kg)	0.052	0.045	0.049	0.053	0.048	0.030	0.032	0.030	0.046	0.043
ρ_2 (kg/m^3)	19.135	22.311	20.218	18.986	21.053	33.223	31.046	33.613	21.810	23.374
v_1 (m^3/kg)	0.559	0.559	0.559	0.559	0.559	0.558	0.558	0.558	0.559	0.558
ρ_1 (kg/m^3)	1.788	1.788	1.788	1.788	1.788	1.791	1.791	1.791	1.788	1.791
a_1 (m/s)	270	270	270	270	270	252	252	252	270	252
M_∞	8.25	10.17	8.88	8.13	9.39	10.37	8.66	10.62	9.89	4.99
ρ_2/ρ_1	**10.7**	**12.48**	**12.48**	**10.62**	**11.78**	**18.54**	**17.33**	**18.76**	**12.2**	**13.05**
$\gamma_{equivalent}$	1.17	1.15	1.15	1.17	1.16	1.094	1.094	1.093	1.156	1.079

Notes regarding Table B.1:

- L1, L2, and L3 denote photodiode stations 1, 2, and 3, respectively, according to the setup shown in Figure 3.11.
- P1, P2, and P3 denote pressure transducer stations 1, 2, and 3, respectively, according to the setup shown in Figure 3.11.
- P_{exit} denotes the pressure transducer at the end of the launch tube.
- BW denotes the Break Wire (also referred to as 'Trip Wire' and 'CH2') at the entrance to the extension tube.
- Qs refers to laser Q-switching, the event that records the shadowgraph.

- U_{ave} and U_{σ} denote the average and standard deviation of the projectile speed, as defined in equations (3.2) and (3.3), respectively.

- The density ratio given is computed assuming chemical equilibrium downstream of the shock.

- $\gamma_{equivalent}$ represents the ratio of specific heats of a perfect gas that would produce the same density ratio at the Mach number given.

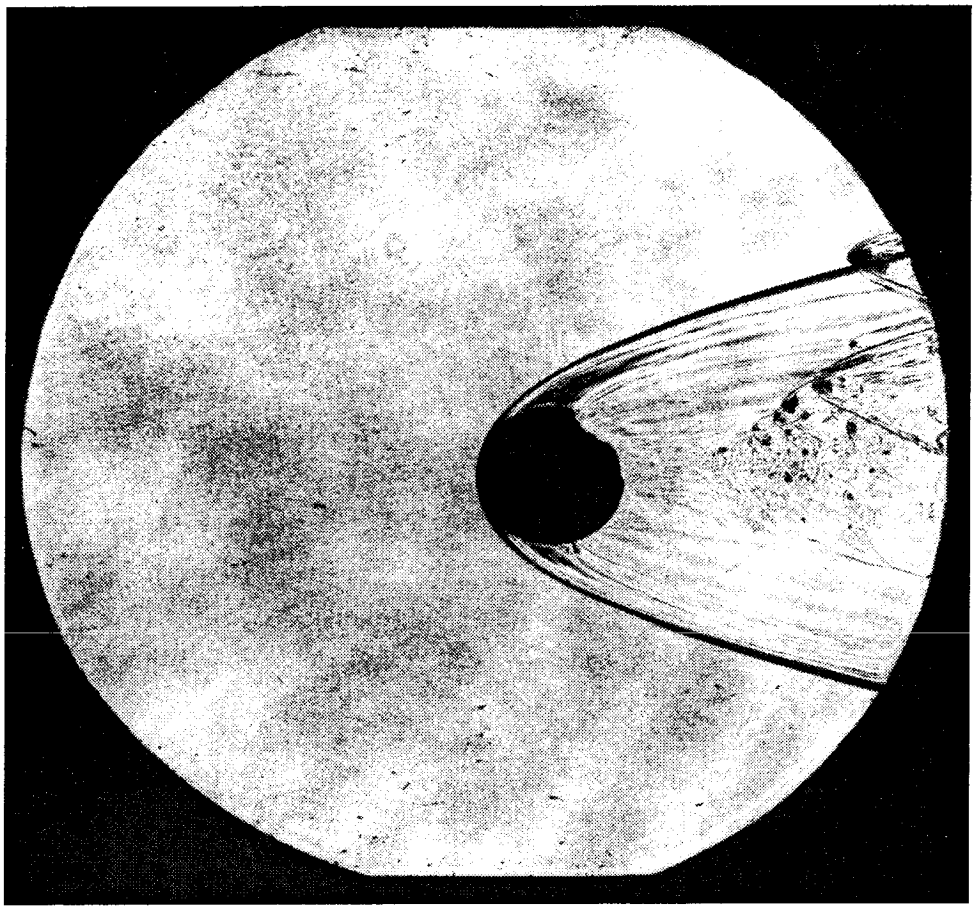

Shot 1841

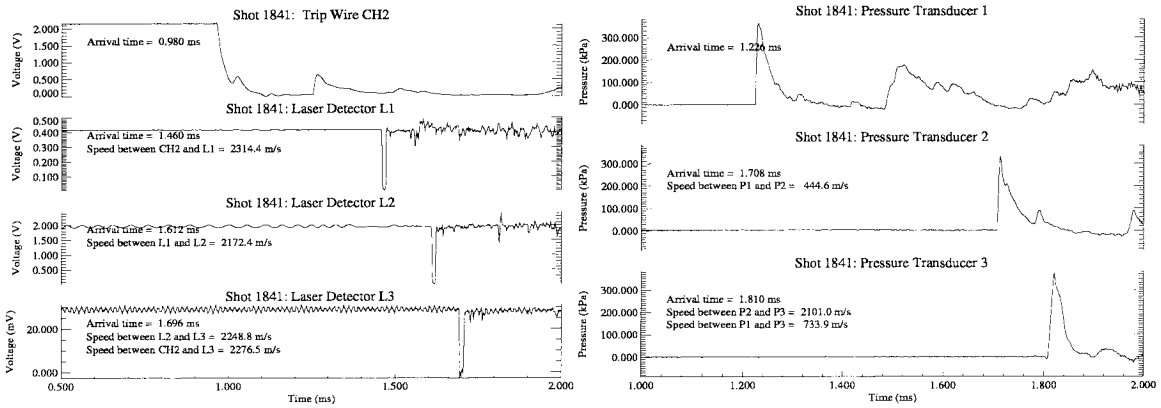

(a) Break wire and photodiode traces (b) Pressure transducer traces

Figure B.1. Shadowgraph and raw timing data (from T5 DAS) for shot 1841.

(No shadowgraph available for shot 1842)

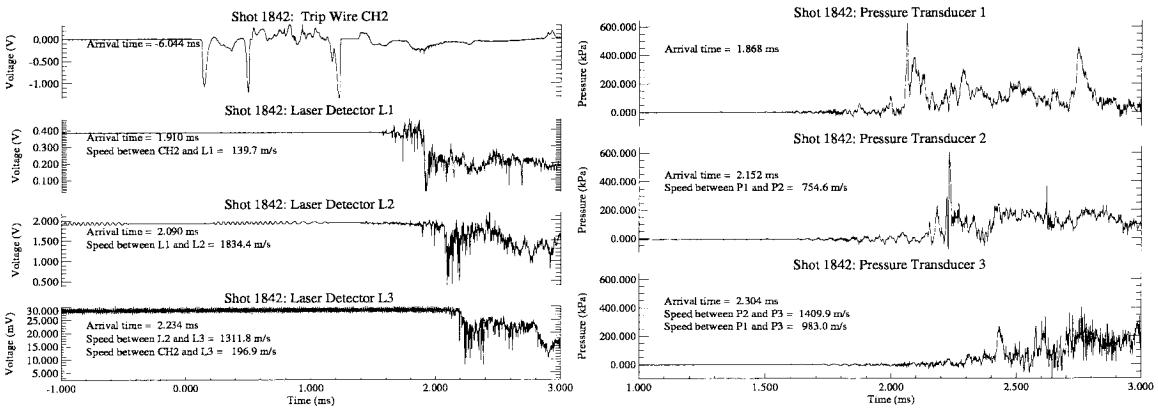

(a) Break wire and photodiode traces

(b) Pressure transducer traces

Figure B.2. Shadowgraph and raw timing data (from T5 DAS) for shot 1842.

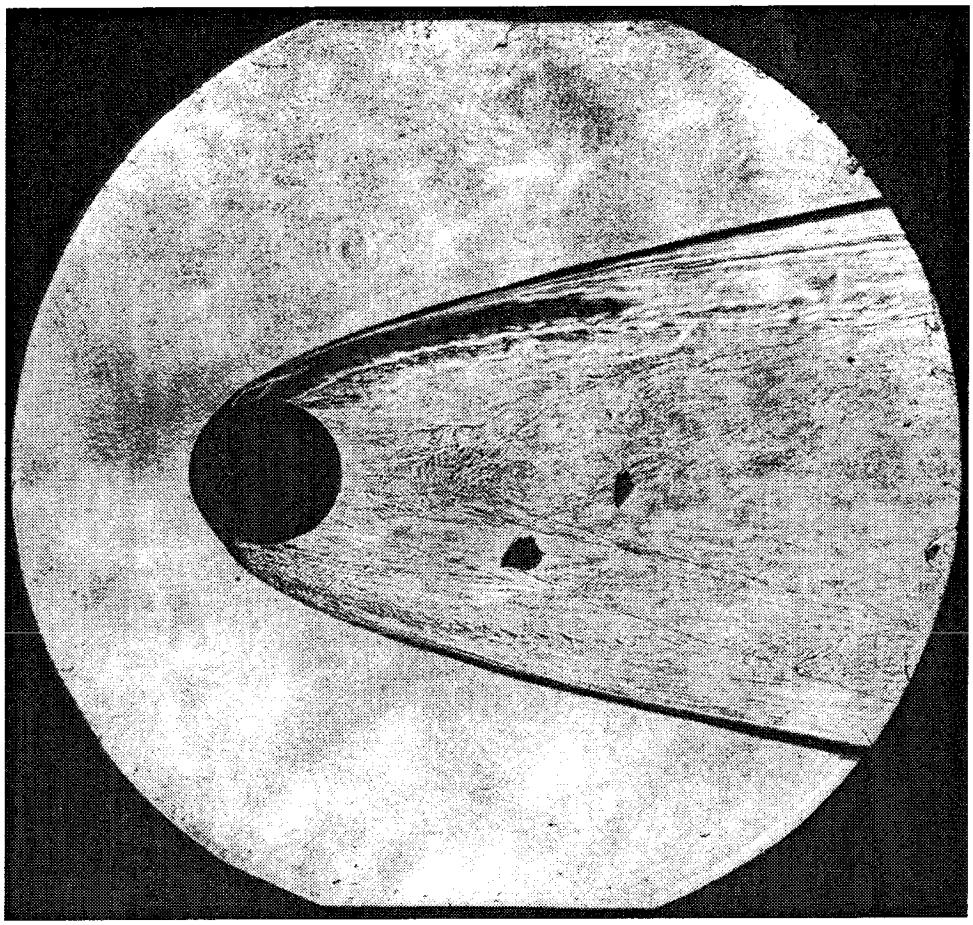

Shot 1843

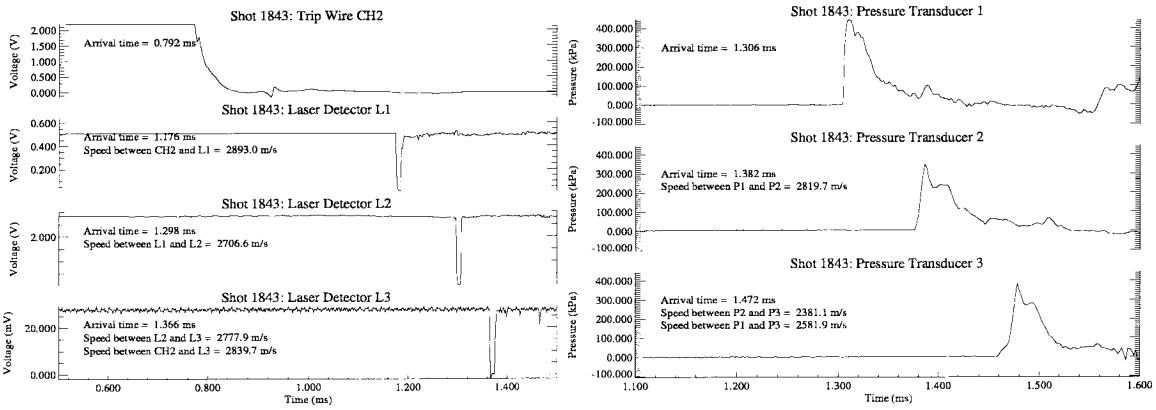

(a) Break wire and photodiode traces (b) Pressure transducer traces

Figure B.3. Shadowgraph and raw timing data (from T5 DAS) for shot 1843.

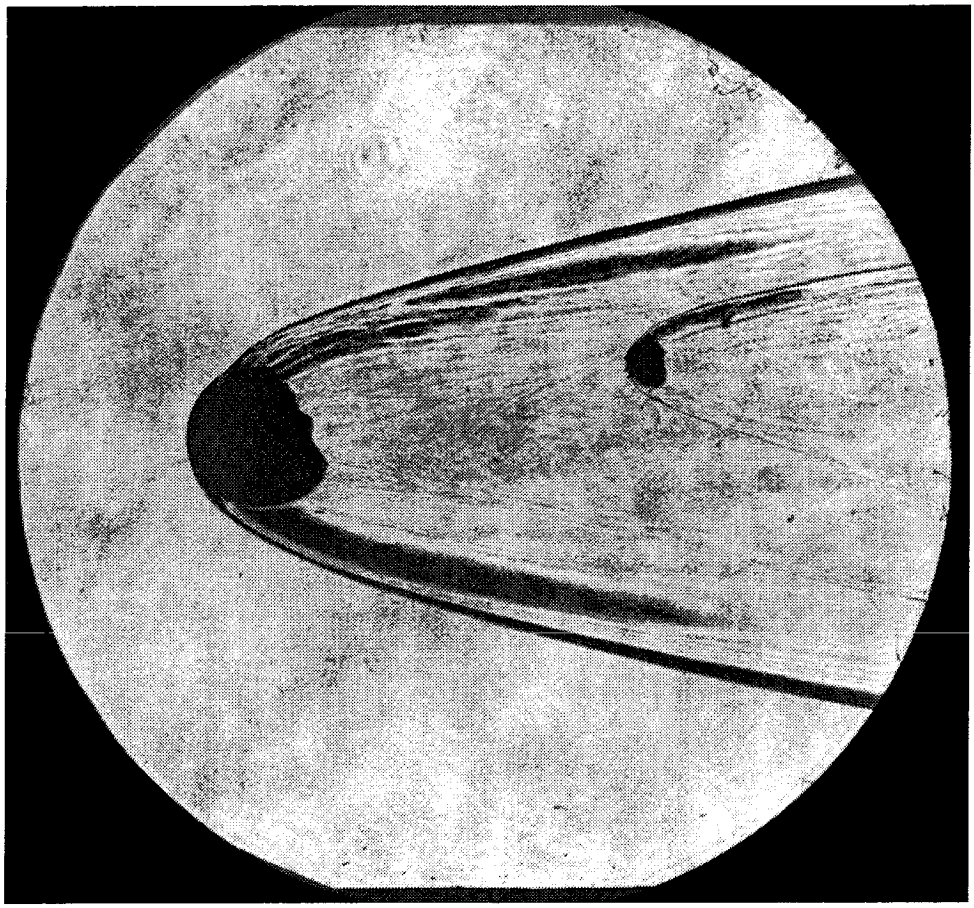

Shot 1844

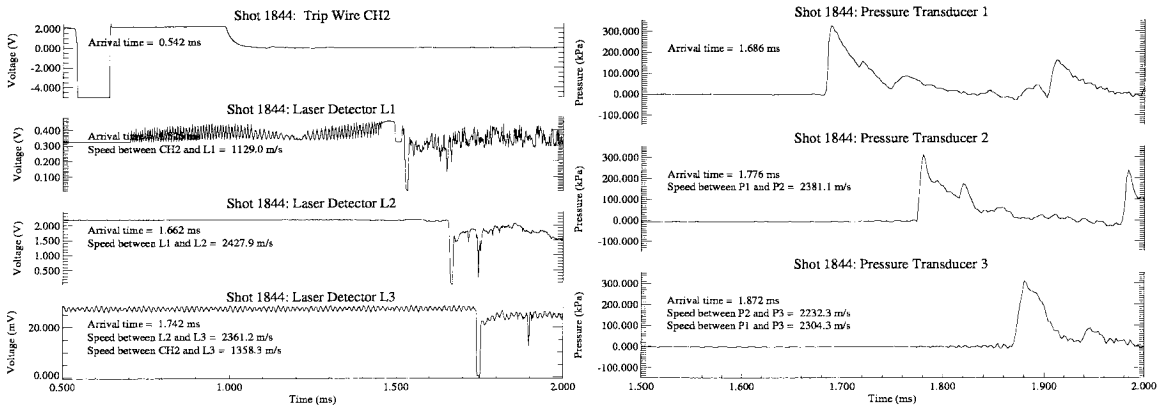

(a) Break wire and photodiode traces (b) Pressure transducer traces

Figure B.4. Shadowgraph and raw timing data (from T5 DAS) for shot 1844.

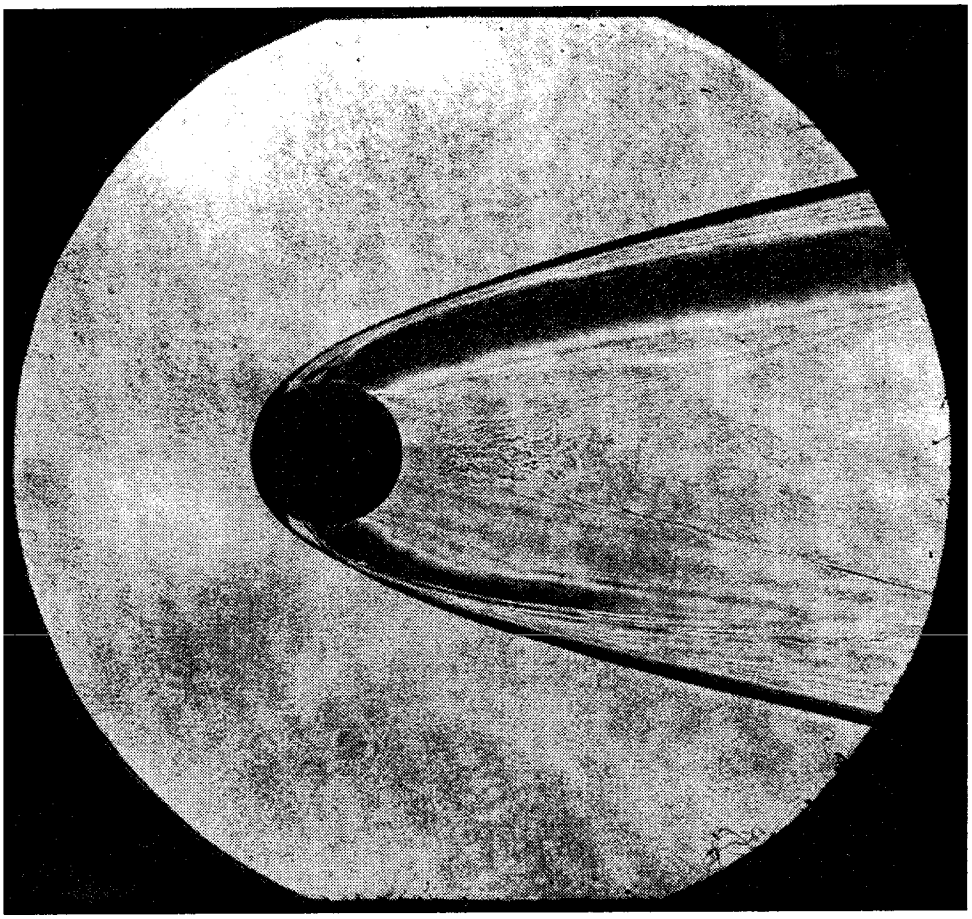

Shot 1845

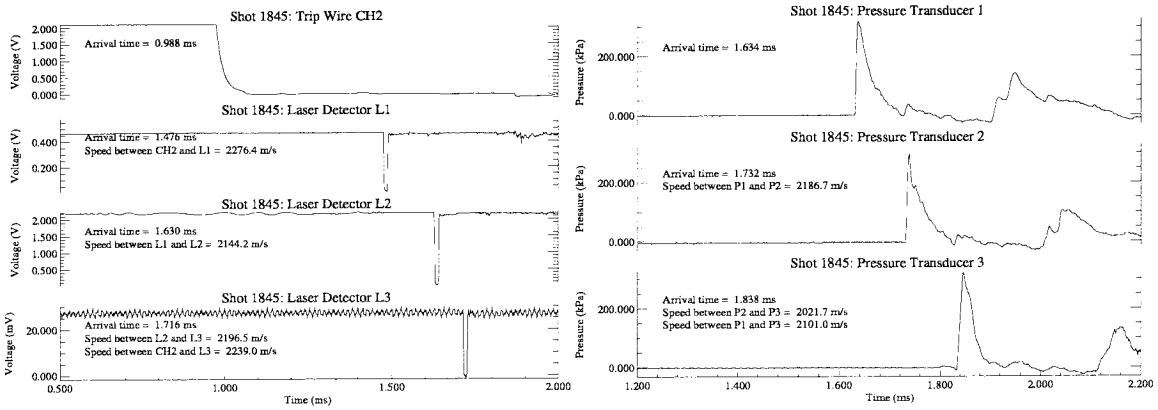

(a) Break wire and photodiode traces

(b) Pressure transducer traces

Figure B.5. Shadowgraph and raw timing data (from T5 DAS) for shot 1845.

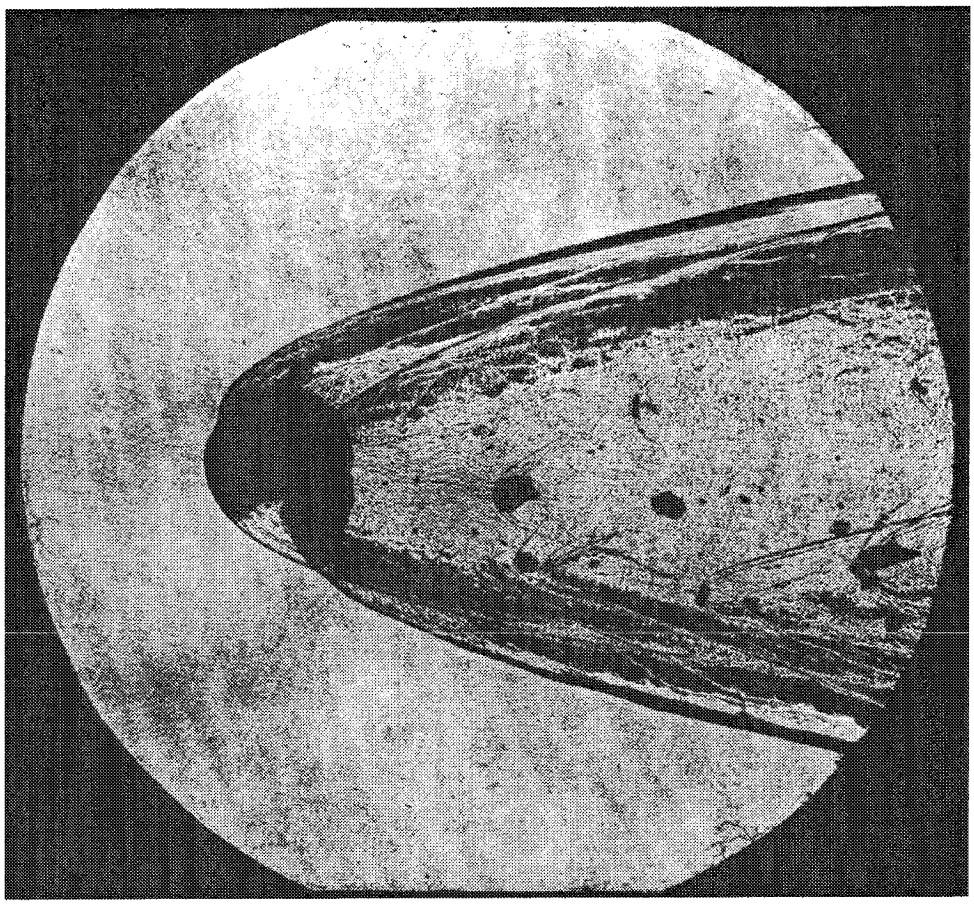

Shot 1846

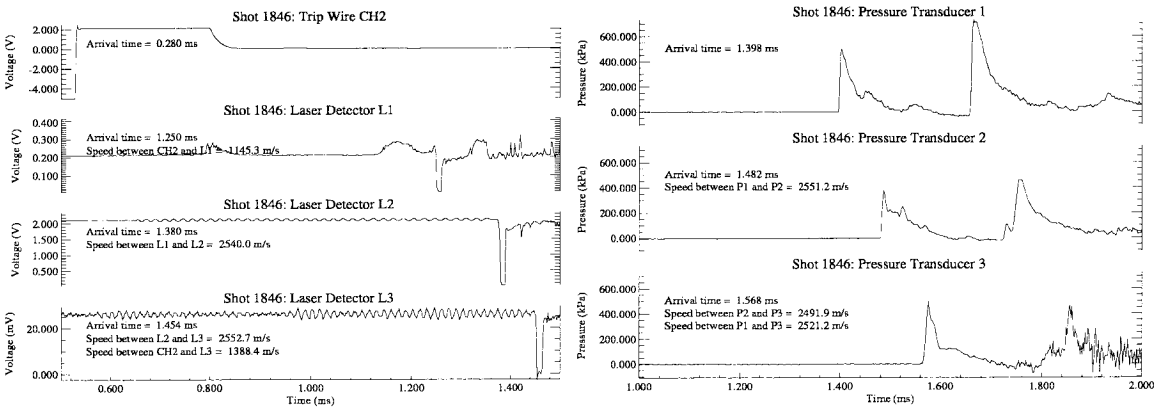

(a) Break wire and photodiode traces (b) Pressure transducer traces

Figure B.6. Shadowgraph and raw timing data (from T5 DAS) for shot 1846.

(No shadowgraph available for shot 1847)

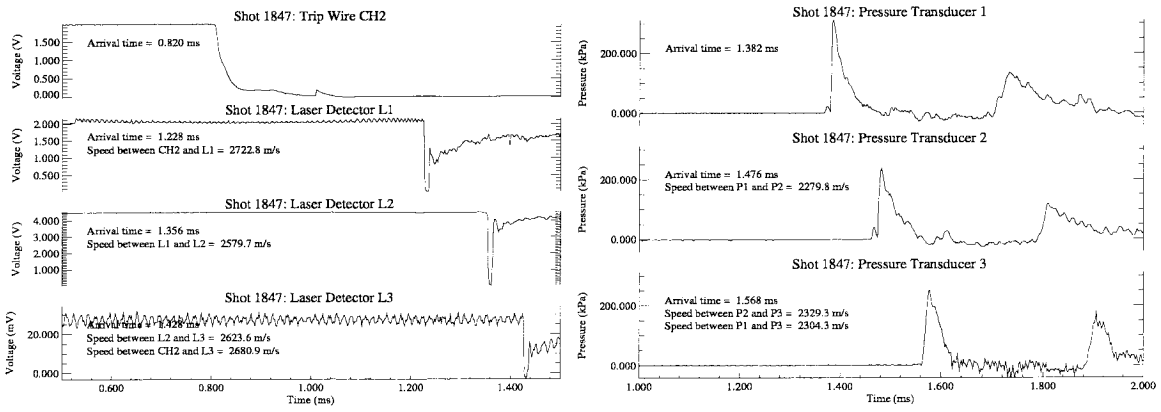

(a) Break wire and photodiode traces (b) Pressure transducer traces

Figure B.7. Shadowgraph and raw timing data (from T5 DAS) for shot 1847.

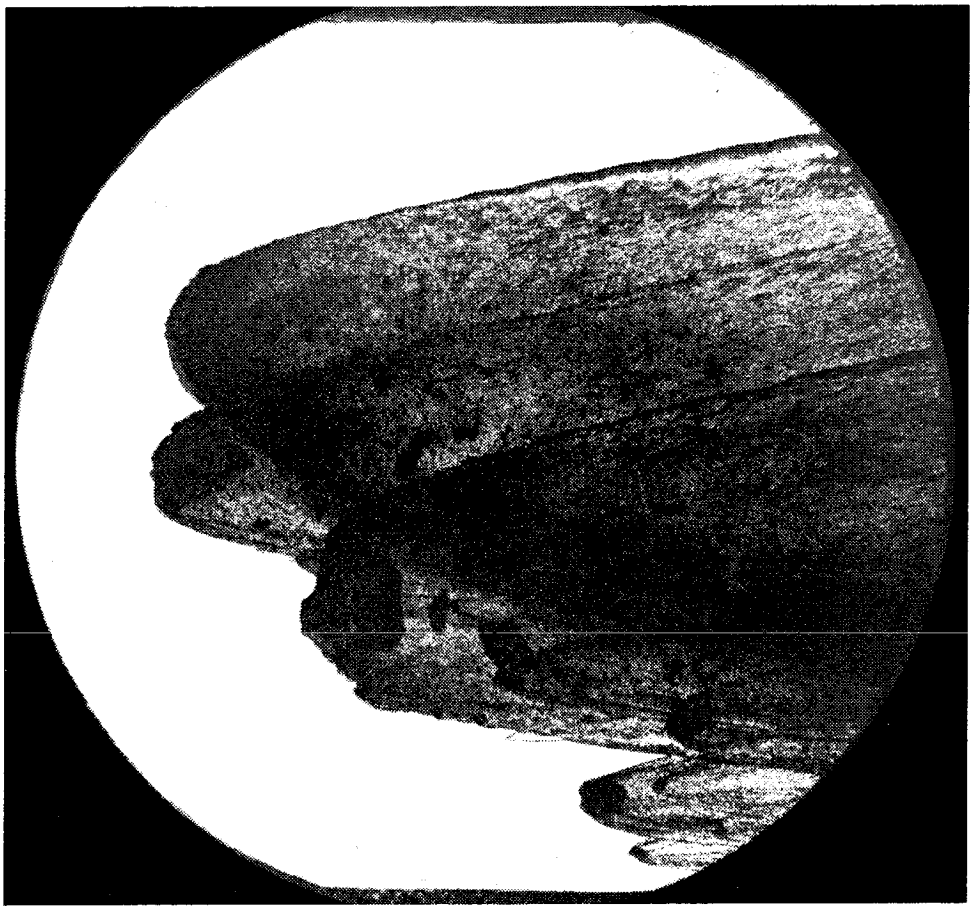

Shot 1848

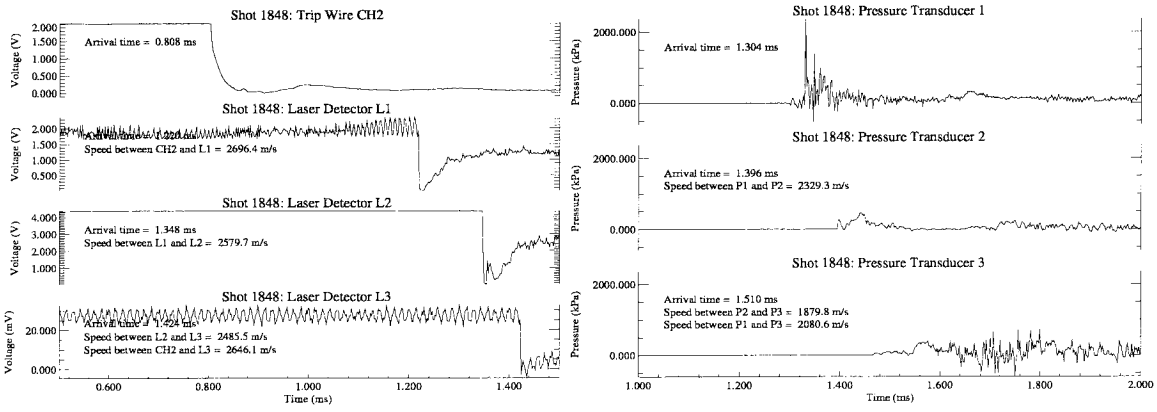

(a) Break wire and photodiode traces (b) Pressure transducer traces

Figure B.8. Shadowgraph and raw timing data (from T5 DAS) for shot 1848.

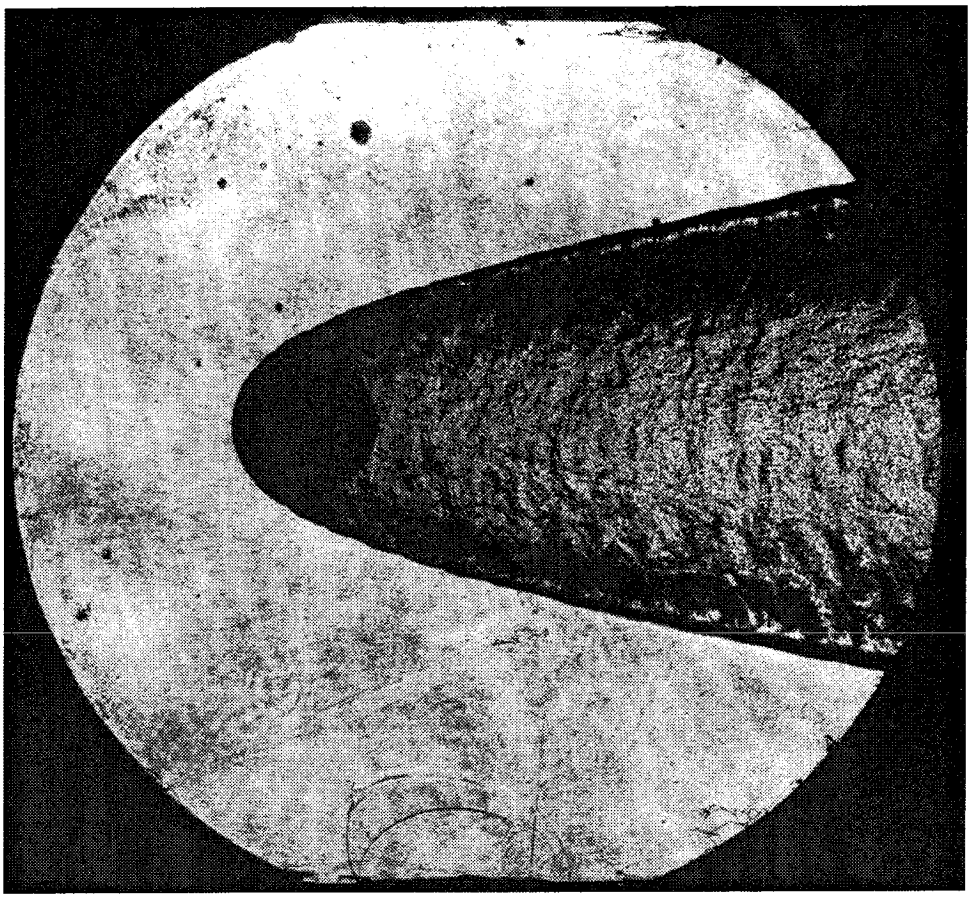

Shot 1849

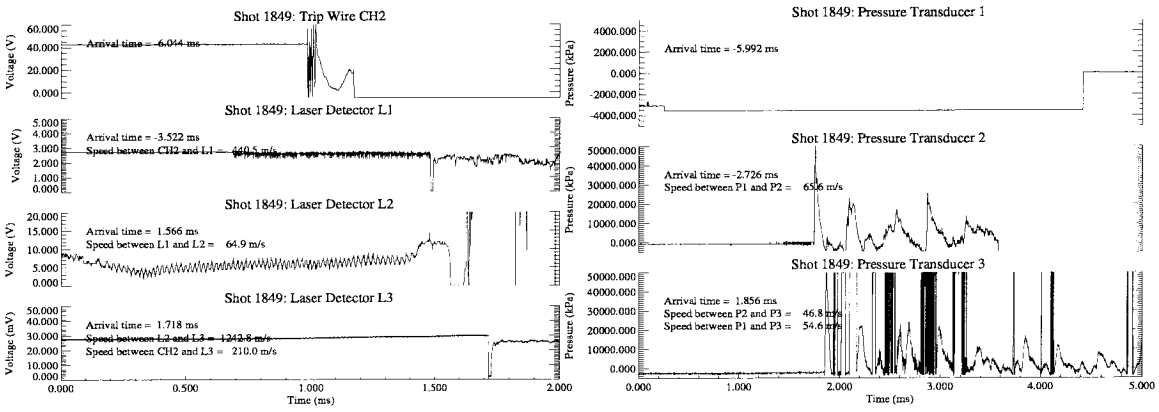

(a) Break wire and photodiode traces (b) Pressure transducer traces

Figure B.9. Shadowgraph and raw timing data (from T5 DAS) for shot 1849.

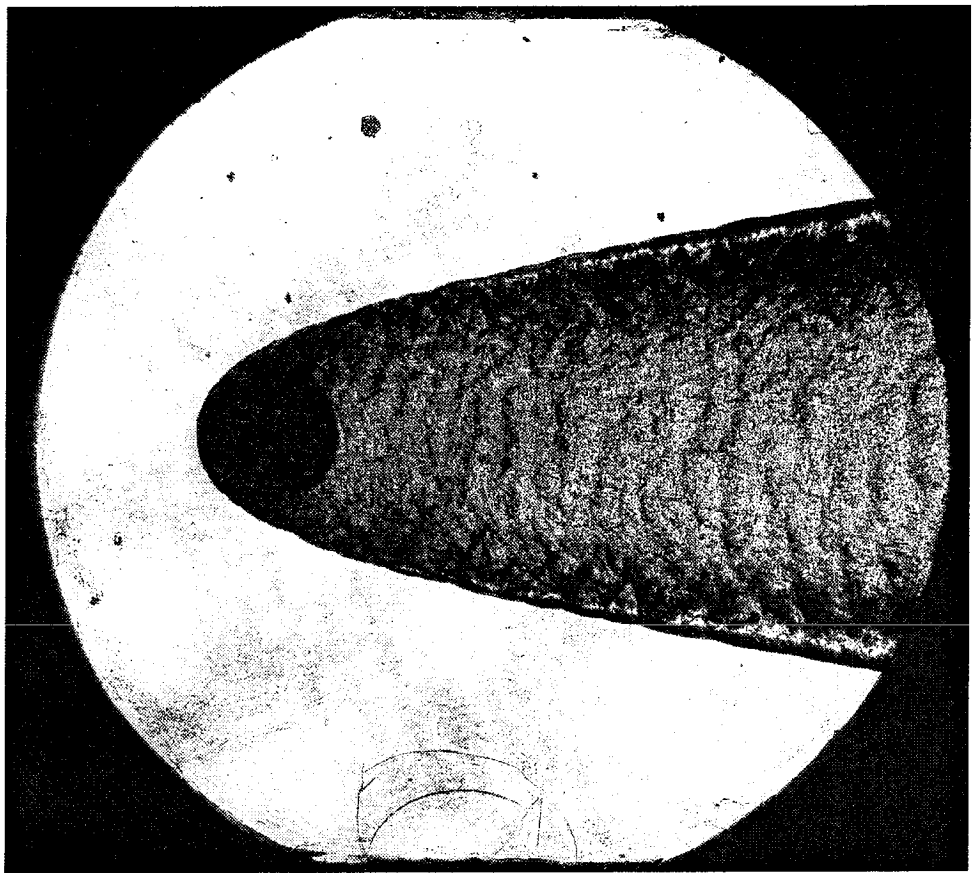

Shot 1850

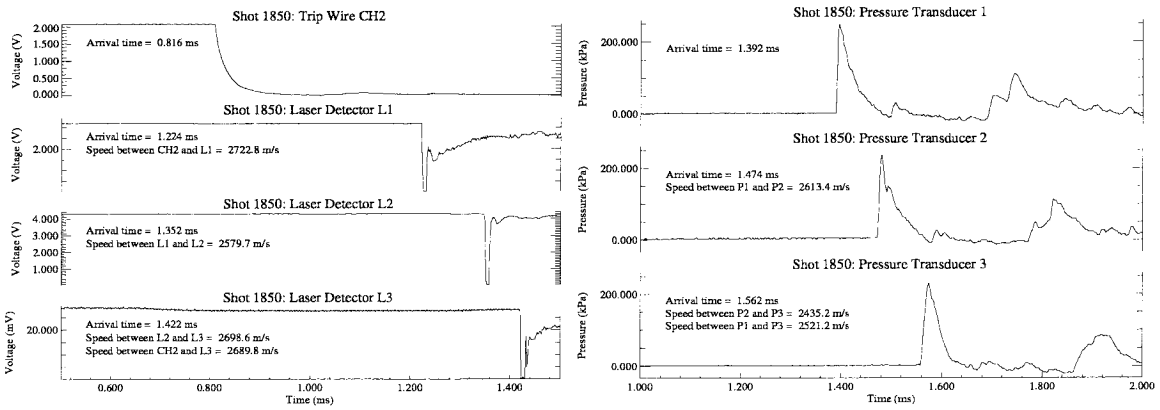

(a) Break wire and photodiode traces (b) Pressure transducer traces

Figure B.10. Shadowgraph and raw timing data (from T5 DAS) for shot 1850.

(No shadowgraph available for shot 1851)

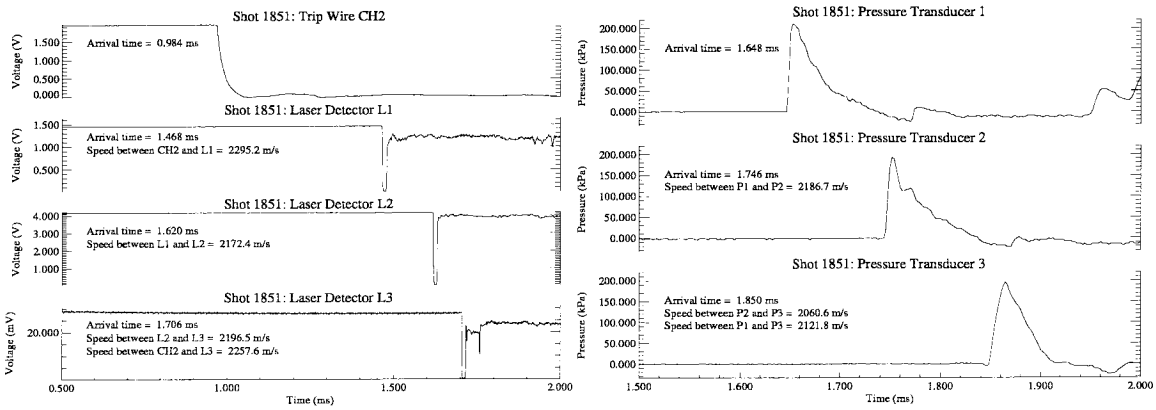

(a) Break wire and photodiode traces (b) Pressure transducer traces

Figure B.11. Shadowgraph and raw timing data (from T5 DAS) for shot 1851.

(No shadowgraph available for shot 1852)

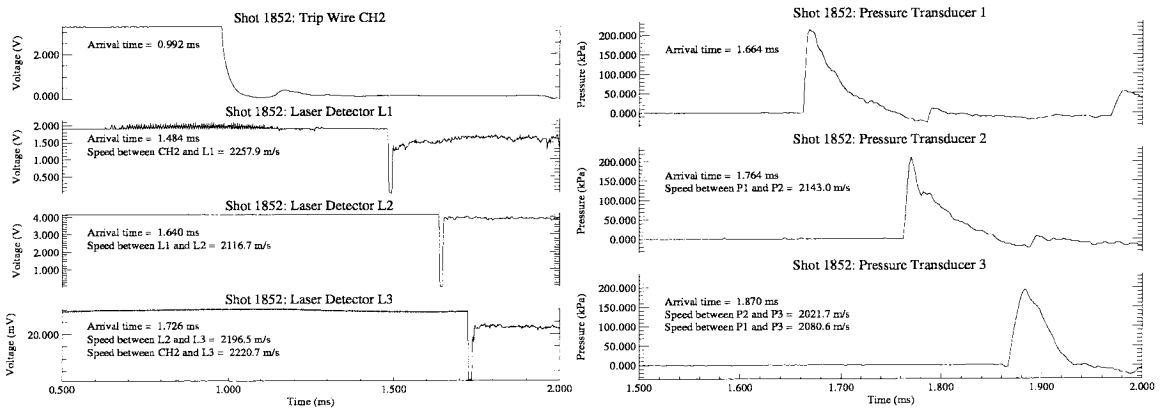

(a) Break wire and photodiode traces

(b) Pressure transducer traces

Figure B.12. Shadowgraph and raw timing data (from T5 DAS) for shot 1852.

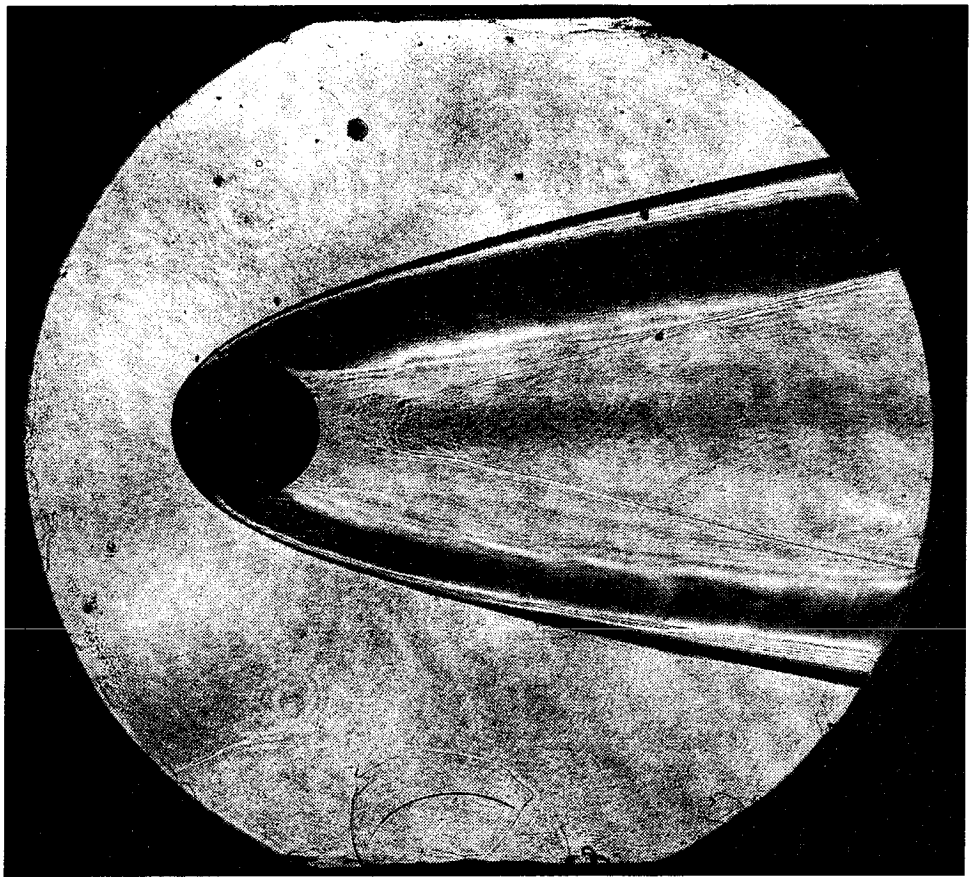

Shot 1853

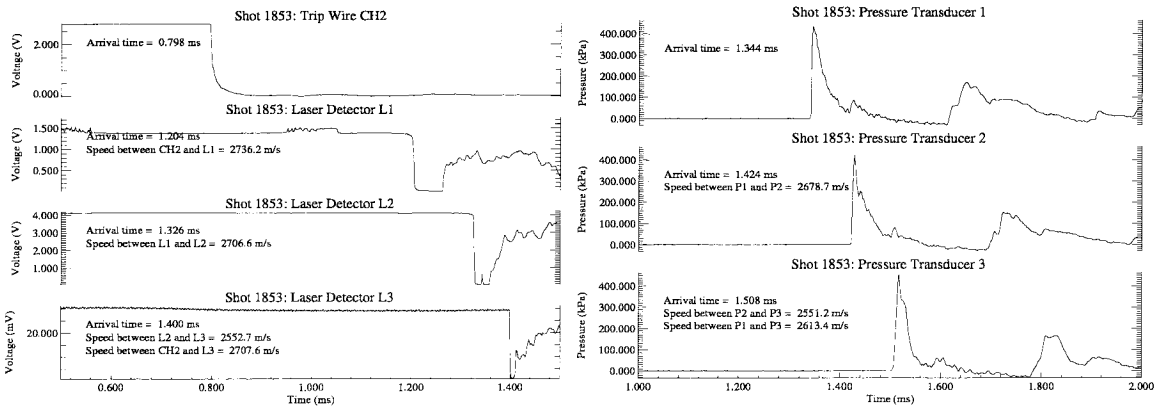

(a) Break wire and photodiode traces (b) Pressure transducer traces

Figure B.13. Shadowgraph and raw timing data (from T5 DAS) for shot 1853.

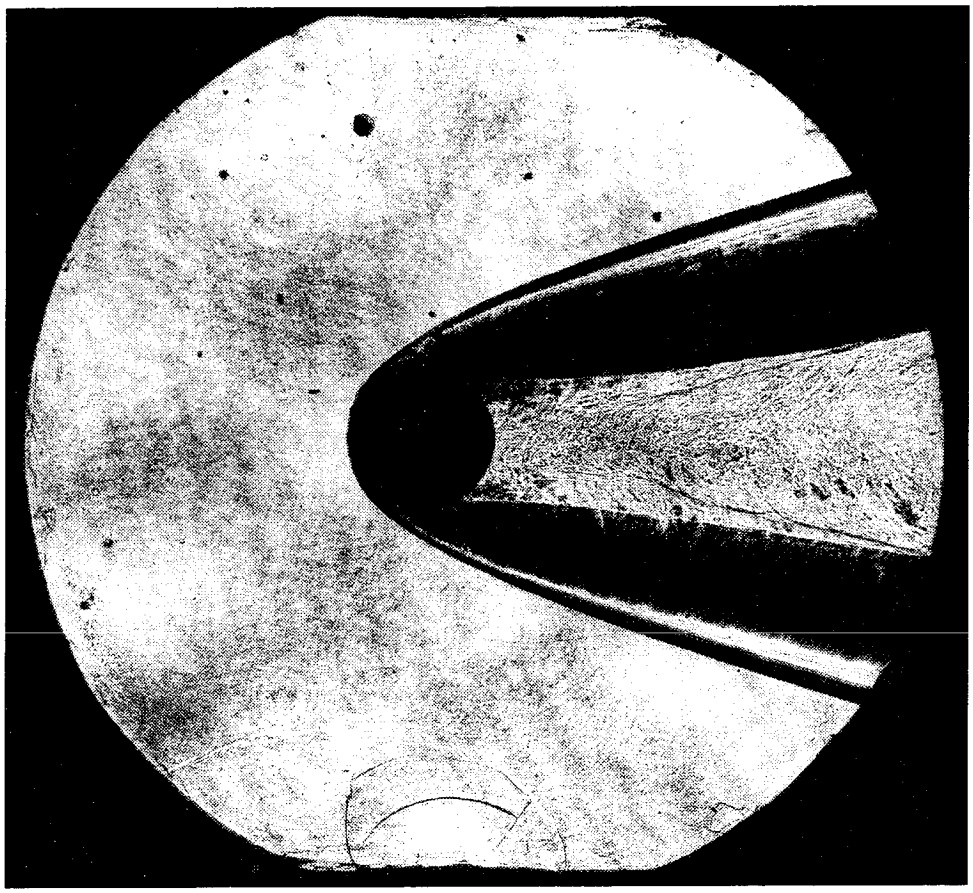

Shot 1854

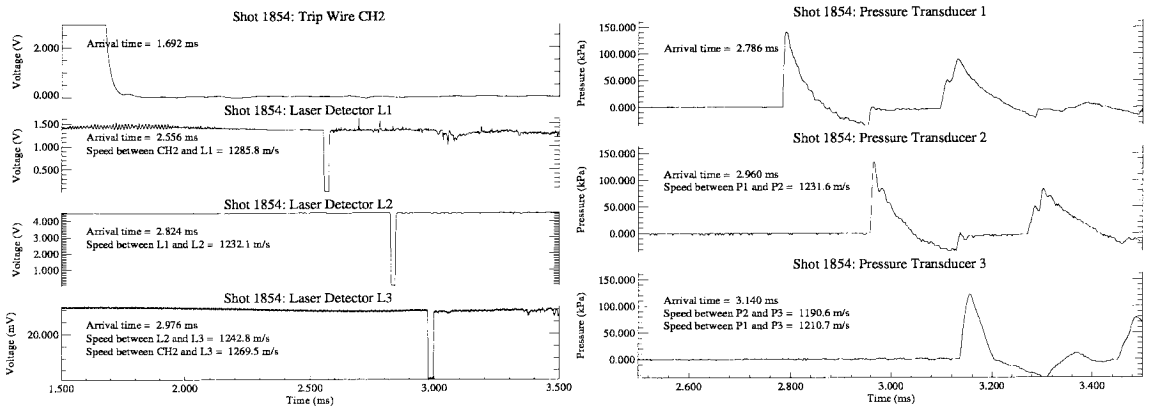

(a) Break wire and photodiode traces (b) Pressure transducer traces

Figure B.14. Shadowgraph and raw timing data (from T5 DAS) for shot 1854.

Appendix C Effect of the vorticity thickness on the wavelength

This appendix presents some additional results concerning the effect of vorticity thickness and free stream disturbances on the instability of the shear layer. These results complement those presented in Chapter 5.

C.1 Description and methodology

The three density ratios presented here are approximately 8.4, 10.5 and 14.9, respectively (maximum values across the normal part of the shock). As seen in Chapter 5, the vorticity thickness at a density ratio of 8.4 is about twice as large as it is at a density ratio of 16.8, and thus permits the qualitative correlation between that parameter and the wavelength of the structures seen in the shear layer.

Each numerical experiment presented here compares a case with no free stream disturbance with several other cases where a disturbance of wavelength 0.73%, 100%, 200%, 300% and 400% times the nose radius has been added to the free stream. Two amplitude levels are used in each test case: 2% and 4%, meaning that the disturbance adds a velocity component perpendicular to the free stream that has a maximum of 2% and 4%, respectively, of the undisturbed free stream speed.

C.2 Results

The results show qualitatively that the preferred wavelength of the disturbances is affected by the vorticity thickness. The higher the density ratio, the thinner the vorticity thickness and the shorter the preferred wavelength of the disturbances observed appears to be. The amplitude of the disturbances, in the range presented here, only

appears to affect the clarity with which the preferred wavelength may be detected in the pseudo-schlieren images. The disturbances are sufficient to cause a detectable instability in the shear layer at both of these amplitude levels, although at a density ratio of 8.4, the effect of the 2% disturbance is noticeable small, compared to the other conditions.

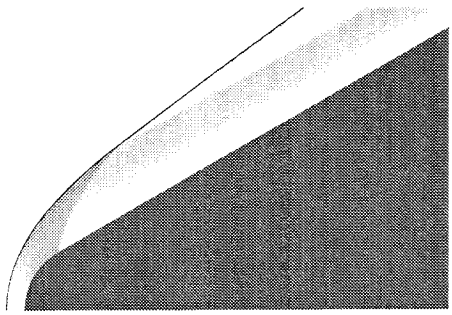

before disturbance

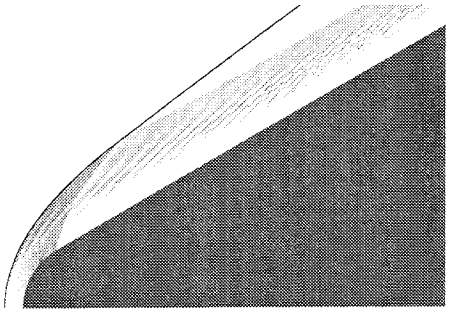

$\lambda/R = 0.733$

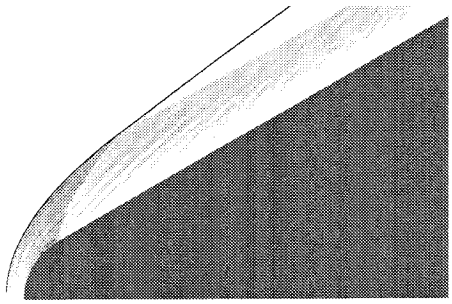

$\lambda/R = 1$

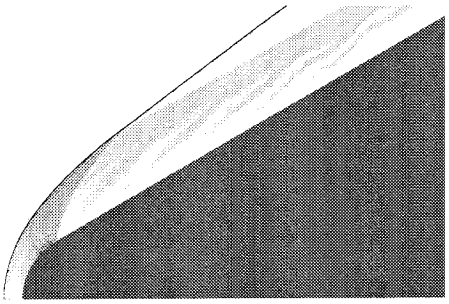

$\lambda/R = 2$

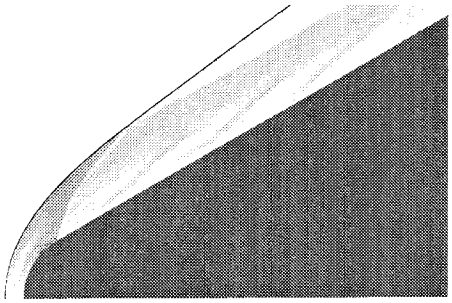

$\lambda/R = 3$

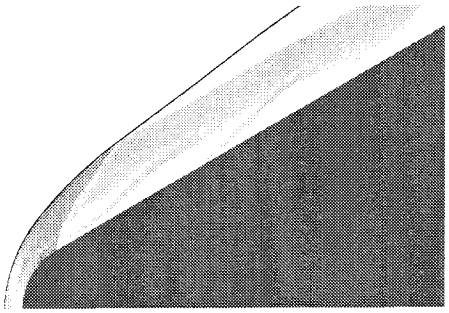

$\lambda/R = 4$

Effect of the vorticity thickness and of the amplitude and wavelength of external disturbances, on the structures developing in the shear layer produced by the shock over a hemicylindrically blunted wedge. The vorticity thickness for this condition is computed in Chapter 5.

$$M_\infty = 5.7,\ \theta = 30.0^\circ,\ \gamma = 1.20,\ \ \rho_2/\rho_1 \approx 8.4$$

amplitude of free stream disturbances: 2.00%

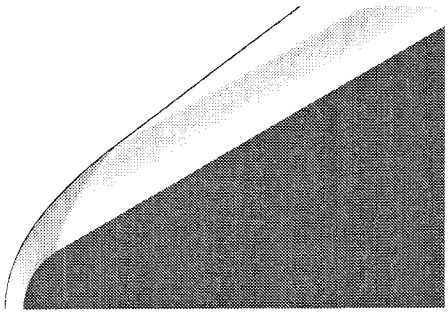

before disturbance

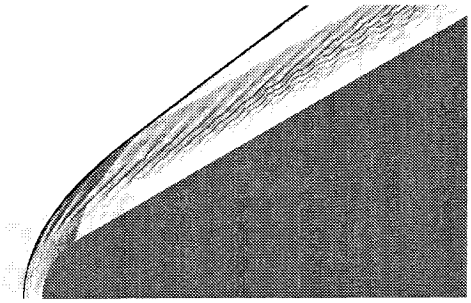

$\lambda/R = 0.733$

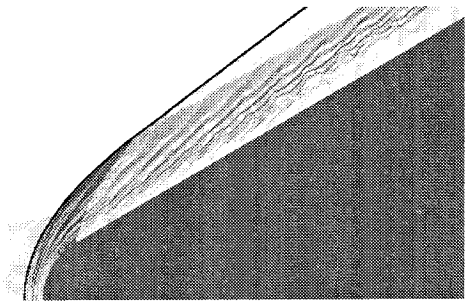

$\lambda/R = 1$

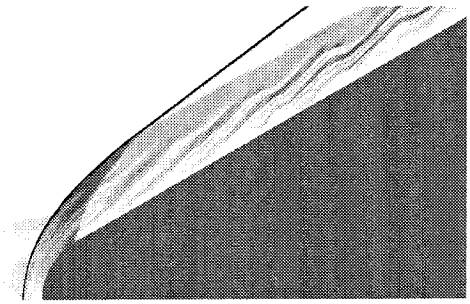

$\lambda/R = 2$

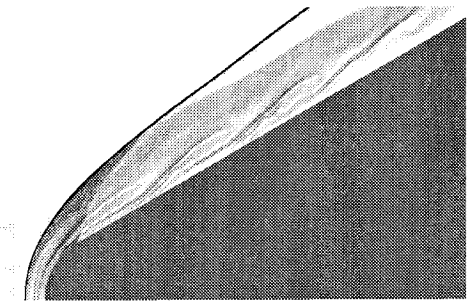

$\lambda/R = 3$

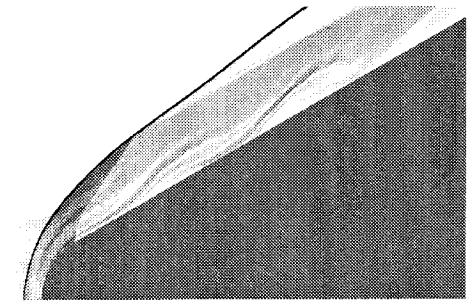

$\lambda/R = 4$

Effect of the vorticity thickness and of the amplitude and wavelength of external disturbances, on the structures developing in the shear layer produced by the shock over a hemicylindrically blunted wedge. The vorticity thickness for this condition is computed in Chapter 5.

$$M_\infty = 5.7,\ \theta = 30.0^\circ,\ \gamma = 1.20,\ \ \rho_2/\rho_1 \approx 8.4$$

amplitude of free stream disturbances: 4.00%

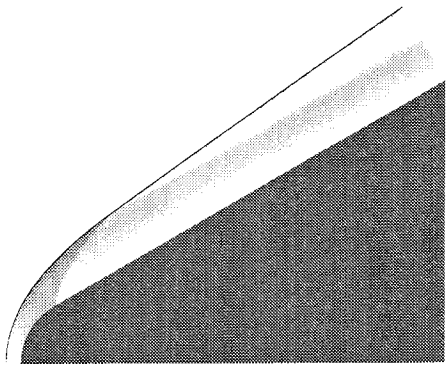

before disturbance

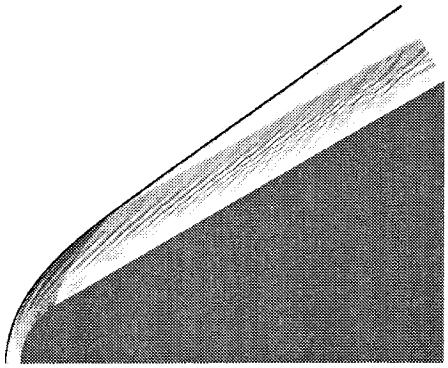

$\lambda/R = 0.733$

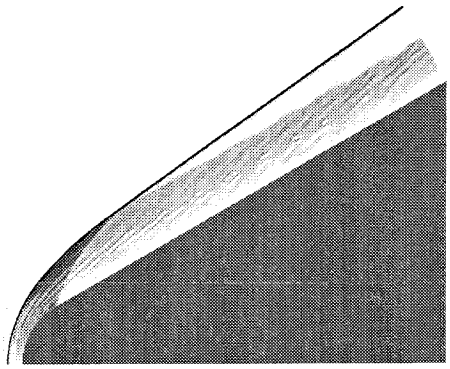

$\lambda/R = 1$

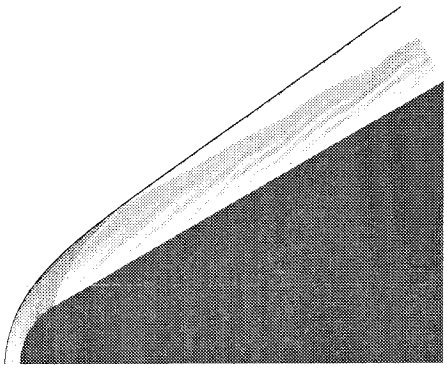

$\lambda/R = 2$

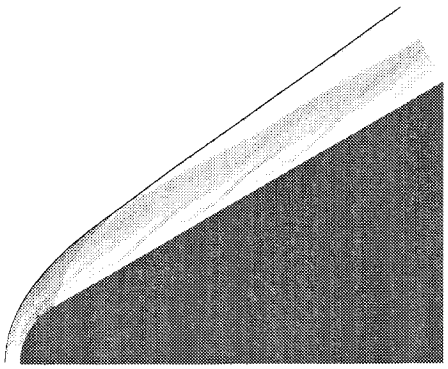

$\lambda/R = 3$

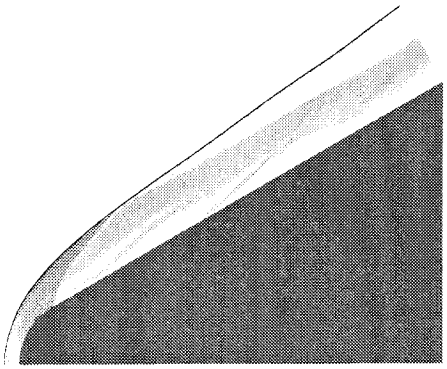

$\lambda/R = 4$

Effect of the vorticity thickness and of the amplitude and wavelength of external disturbances, on the structures developing in the shear layer produced by the shock over a hemicylindrically blunted wedge. The vorticity thickness for this condition is computed in Chapter 5.

$M_\infty = 6.0$, $\theta = 30.0°$, $\gamma = 1.15$, $\rho_2/\rho_1 \approx 10.5$

amplitude of free stream disturbances: 2.00%

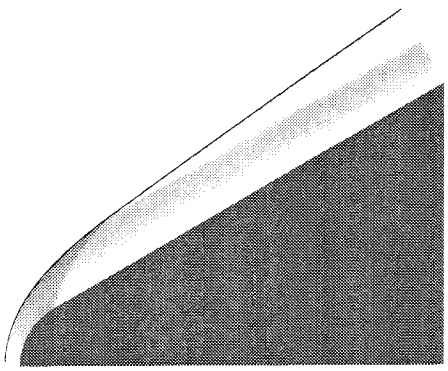

before disturbance

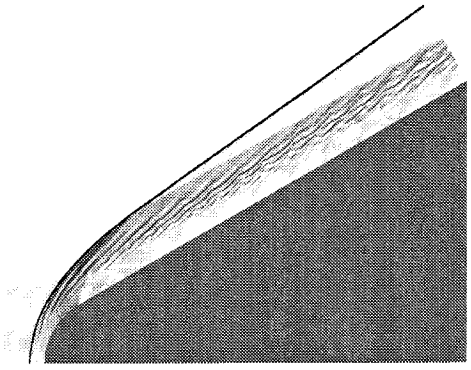

$\lambda/R = 0.733$

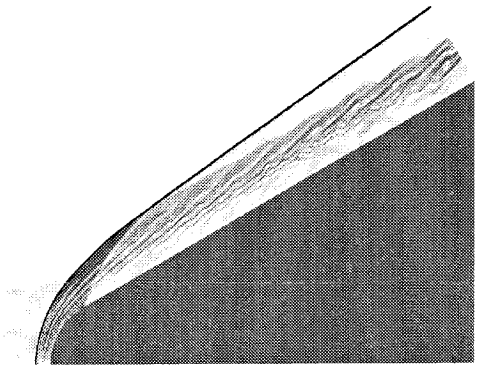

$\lambda/R = 1$

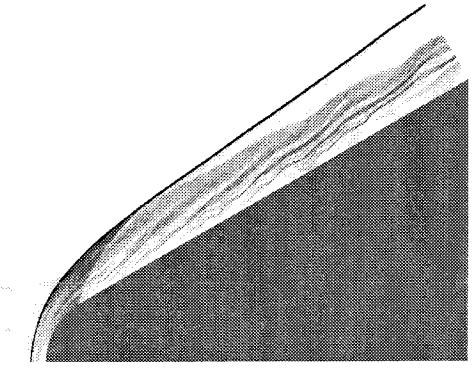

$\lambda/R = 2$

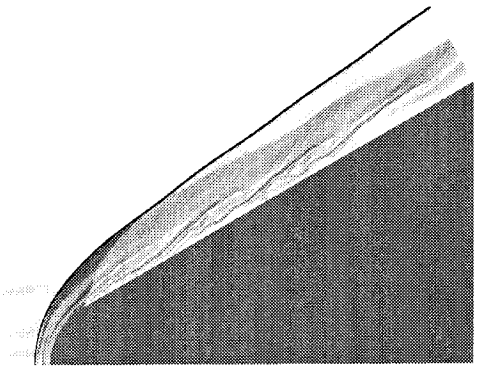

$\lambda/R = 3$

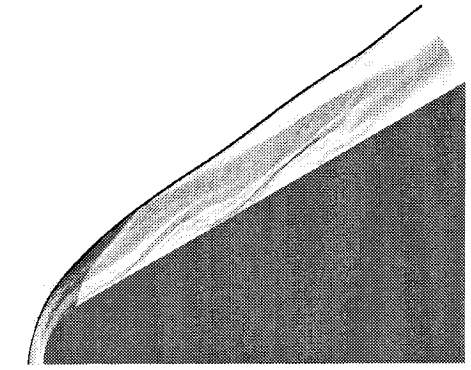

$\lambda/R = 4$

Effect of the vorticity thickness and of the amplitude and wavelength of external disturbances, on the structures developing in the shear layer produced by the shock over a hemicylindrically blunted wedge. The vorticity thickness for this condition is computed in Chapter 5.

$M_\infty = 6.0$, $\theta = 30.0°$, $\gamma = 1.15$, $\rho_2/\rho_1 \approx 10.5$

amplitude of free stream disturbances: 4.00%

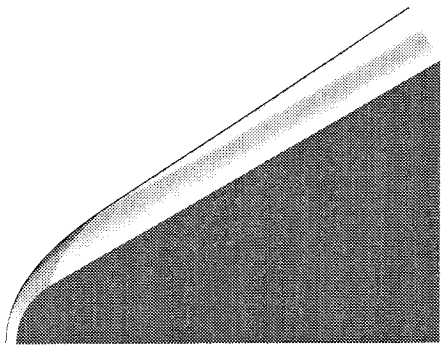

before disturbance

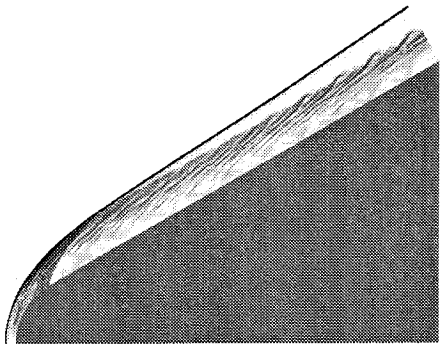

$\lambda/R = 0.733$

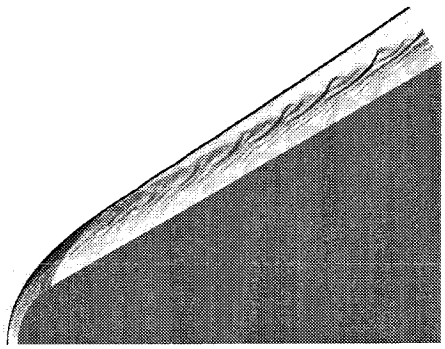

$\lambda/R = 1$

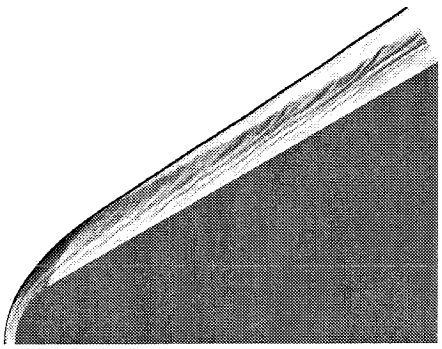

$\lambda/R = 2$

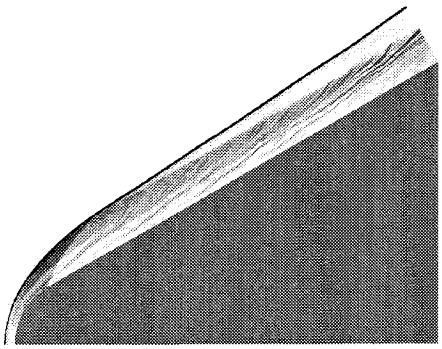

$\lambda/R = 3$

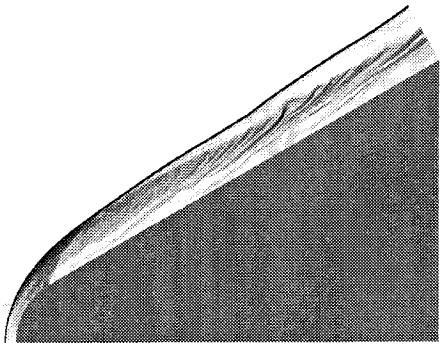

$\lambda/R = 4$

Effect of the vorticity thickness and of the amplitude and wavelength of external disturbances, on the structures developing in the shear layer produced by the shock over a hemicylindrically blunted wedge. The vorticity thickness for this condition is computed in Chapter 5.

$M_\infty = 7.0$, $\theta = 30.0°$, $\gamma = 1.10$, $\rho_2/\rho_1 \approx 14.9$

amplitude of free stream disturbances: 2.00%

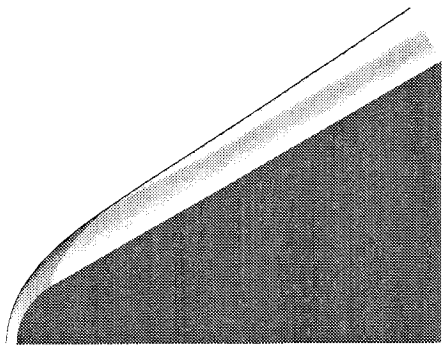

before disturbance

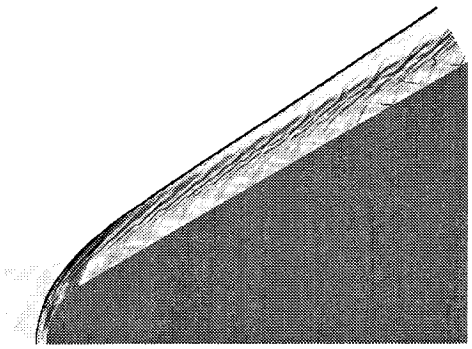

$\lambda/R = 0.733$

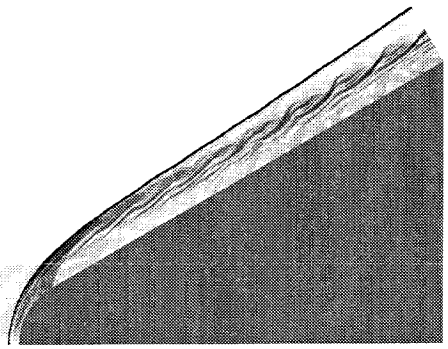

$\lambda/R = 1$

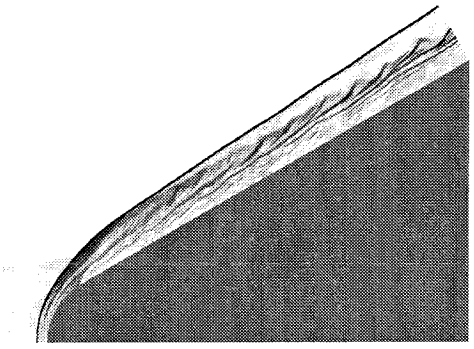

$\lambda/R = 2$

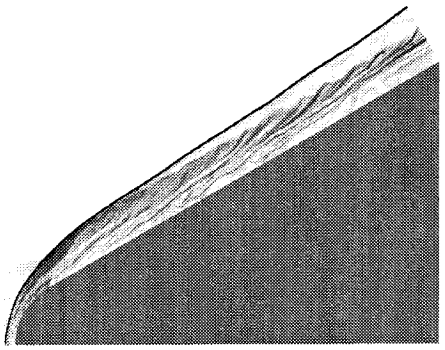

$\lambda/R = 3$

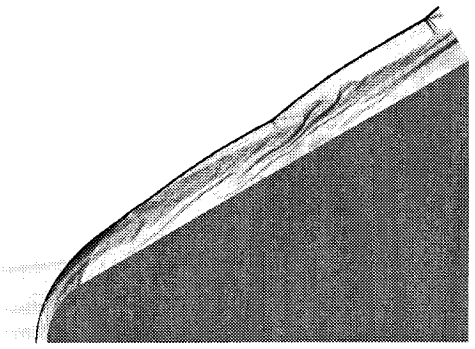

$\lambda/R = 4$

Effect of the vorticity thickness and of the amplitude and wavelength of external disturbances, on the structures developing in the shear layer produced by the shock over a hemicylindrically blunted wedge. The vorticity thickness for this condition is computed in Chapter 5.

$M_\infty = 7.0$, $\theta = 30.0°$, $\gamma = 1.10$, $\rho_2/\rho_1 \approx 14.9$

amplitude of free stream disturbances: 4.00%

Appendix D Caustic effects associated with the T5 optics system

The shadowgraphs of the Light Gas Gun experiment shown in Chapter 5 featured two symmetric dark bands on each side of the projectile path in the shock layer. This is particularly evident in shots at low density ratios where the undisturbed shear layer is relatively homogeneous (see for example Figure D.1, which is repeated from Chapter 5 for convenience) but the same phenomenon is also present even in the turbulent shear layer of the shots at high density ratios. Caustic effects associated with changes in density across the shock layer, along with the geometry of the optics system, were found to be responsible for these features of the flow.

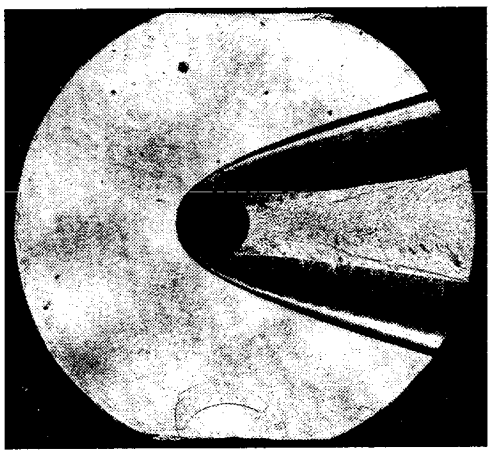

Figure D.1. Shot 1854.

The distance traveled by the light after passing through the test section in the Light Gas Gun experiments, is significantly increased compared to the standard configuration of T5 (see Figure 3.8). This means that the maximum angle through which light may be refracted is necessarily smaller than when T5 is used in the standard configuration. The problem is illustrated in Figure D.2 and explained here.

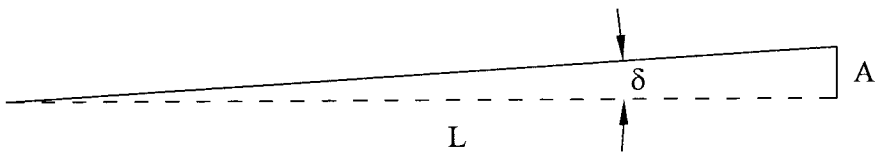

Figure D.2. Maximum deflection of ray passing through a region of high refractivity in the test section. L is the distance from the test section to the aperture; A is the distance between the undeflected light and the edge of the aperture. L is of the order of meters; A is of the order of milimeters.

Consider a light beam traveling through the undisturbed test gas prior to a shot and penetrating the camera aperture a distance A from its edge. Now, assume that the light beam traverses a region of varying refractivity (*e.g.*, in the shock layer of the projectile), so that the beam is defelcted by an angle δ. Thus, δ is fixed by the test gas and the condition. For a given camera aperture, A is also fixed, so that there

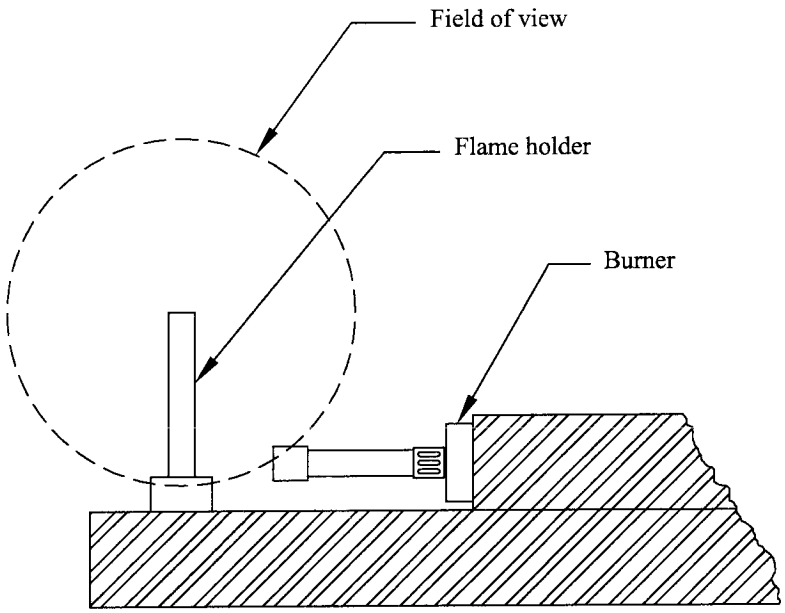

Figure D.3. Setup to verify caustic effects of T5 optical system.

exists a length L beyond which $L \tan\delta > A$. Any light refracted from a distance greater than L will therefore not reach the photographic plate, and will be blocked by the aperture. The setup in the Light Gas Gun experiment is such that the L value is too large to capture a significant part of the light which passes through the shock layer, for the refractivity of the flow and the camera aperture setting used in the experiment. The problem is compounded by astigmatism associated with the folded 'Z' pattern of the optical system used, and by a combined automatic shutter/variable aperture unit which is difficult to position exactly at the focal point of the camera lens.

A control experiment, performed to illustrate this effect, was conducted using the T5 optics system. The parameters of importance are the dimensions L and A of the optics system and the light diffraction angle δ associated with features ofthe flow.

To simulate the effect of varying refractivity in the flow, a propane flame (from a burner) was projected onto a verical post. The turbulence and large density gradients of the gases around this post were imaged using the same shadowgraph system used in the experiments. The setup is illustrated in Figure D.3.

The remaining two parameters, the length of the optical arm L and the aperture diameter A can be varied to observe their relative effect on the shadowgraphs. In particular, the shutter/aperture unit used in the experiments has a continuous adjustment (unlike discrete f-stop settings typically used on most commercial camera system), so that a large range of aperture settings is possible. The effect of these changes in aperture settings is illustrated in Figures D.4 (a) and (b).

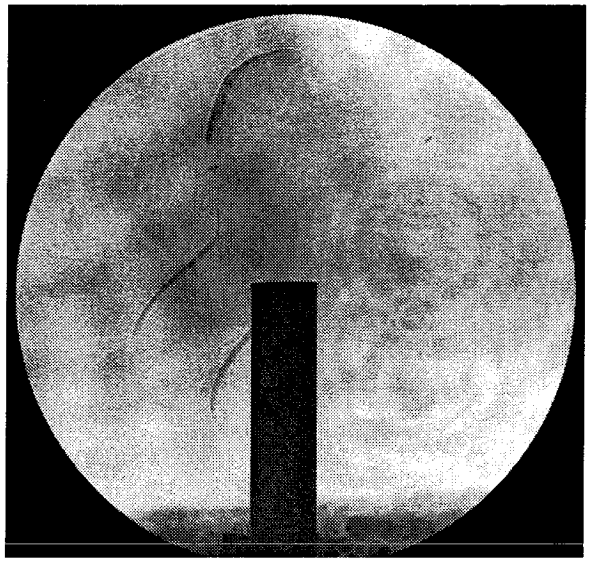

(a)

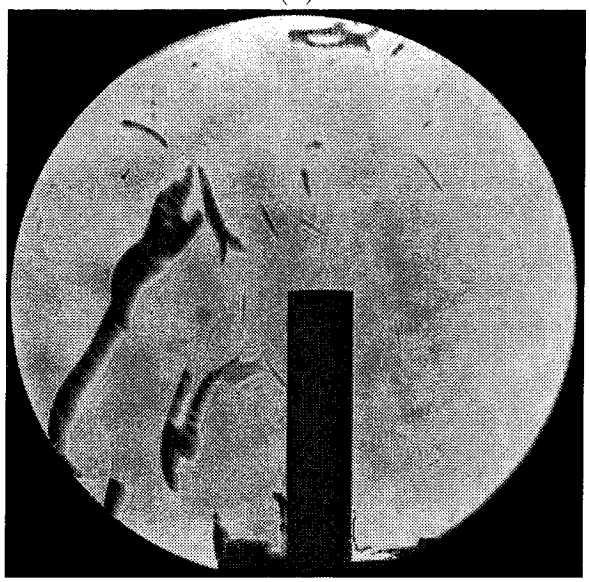

(b)

Figure D.4. Effect of the optical setup on shadowgraphs: varying the aperture. (a) wide aperture (b) narrow aperture.